Five-Dimensional Hadamard-Transform Fluorescence Imaging

By

Oren G. Katz

B.Sc. Chemistry, Queen's University 2020

A thesis submitted in partial fulfillment of the requirements for the degree of

MASTER OF SCIENCE

in the Department of Chemistry

University of Victoria

Five-Dimensional Hadamard-Transform Fluorescence Imaging

By

Oren G. Katz

B.Sc. Chemistry, Queen's University 2020

Supervisory Committee

Dr. Hans-Peter Loock, Supervisor
Department of Chemistry

Dr. Reuven Gordon, Member
Department of Electrical and Computer Engineering

Abstract

A home-built imaging system is designed and characterized which can capture fluorescence over two spectral dimensions (excitation and emission wavelengths) and two spatial dimensions (x and y), at an acquisition rate fast enough to study dynamic chemical systems which change over time (t) and exhibit both complex spectra and spatial inhomogeneity.

Fluorescence excitation-emission matrix (EEM) spectroscopy can identify compounds based on their unique fluorescence fingerprint, but the acquisition rates of conventional techniques are too slow and restrict applications of EEM spectroscopy to static solutions. Furthermore, none of the EEM systems reported to date provides spatial information on how fluorescence EEM signatures may differ in an inhomogeneous sample.

The imaging system described in this thesis uses a fully programmable light source to illuminate a sample with many wavelengths simultaneously, instead of one at a time. Our approach is based on Hadamard-transform (HT) multiplexing and can decrease the acquisition time 500-fold compared to conventional methods. By coupling the programmable light source to an eight-channel snapshot hyperspectral camera, the emission and excitation response can be measured for each of the 256×256 pixels in an image – producing 65,536 EEM spectra in less than 8 seconds. A tensor-rank decomposition method, parallel factor analysis (PARAFAC), is employed to distill the five-dimensional ($x, y, \lambda_{ex}, \lambda_{em}, t$) dataset to the component fluorophores, whose kinetics and chemical transformations can then be studied independently of one another.

The HT-EEM imaging system is demonstrated with two fluorescent dyes (rhodamine B and fluorescein) in a mixture with different solvent phases. The fluorescence EEM of each dye is identified both spatially and spectrally. One hundred 4D images are acquired over 13 minutes while the mixture is heated, to study the thermal quenching effects on Rhodamine B. The applicability of this technology towards high-throughput assays and information-rich fluorescence microscopy is briefly discussed.

Table of Contents

List of Figures

List of Tables

List of Abbreviations

x pixel or spatial dimension	x
y pixel or spatial dimension	y
Excitation wavelength or spectral dimension	λ_{ex}
Emission wavelength or spectral dimension	λ_{em}
Time or temporal dimension	t
Two-Dimensional	2D
Thee-Dimensional	3D
Four-Dimensional	4D
Five-Dimensional	5D
Alternating Least Squares	ALS
Application Programming Interface	API
Charge-Coupled Device	CCD
Capillary Electrophoresis	CE
Confocal Laser Scanning Microscopy	CLSM
Complementary Metal-Oxide Semiconductor	CMOS
Difference Gel Electrophoresis	DiGE
Digital Micromirror Array	DMA
Digital Micromirror Device	DMD
Deoxyribonucleic Acid	DNA
Dissolved Organic Mater	DOM
Excitation Emission Matrix	EEM
Field Of View	FOV

Förster Resonance Energy Transfer	FRET
Full-Width at Half-Maximum	FWHM
Graphical User Interface	GUI
Highest Occupied Molecular Orbital	HOMO
High-Performance Liquid Chromatography	HPLC
Hyperspectral Image or Imaging	HSI
Hadamard-Transform	HT
Integral Field Spectroscopy	IFS
Light Emitting Diode	LED
Laser Induced Fluorescence	LIF
Lowest Occupied Molecular Orbital	LUMO
Microelectromechanical System	MEMS
Magnetic Resonance Imaging	MRI
Multispectral Beam-Splitting	MSBS
Parallel Factor Analysis	PARAFAC
Principal Component Analysis	PCA
Photomultiplier Tube	PMT
Random-Access Memory	RAM
Red Green Blue	RGB
Ribonucleic Acid	RNA
Region Of Interest	ROI
Signal-to-Background Enhancement	SBE
Signal-to-Background Ratio	SBR
Signal-to-Noise Enhancement	SNE
Signal-to-Noise Ratio	SNR

Spectrally Resolving Detector Array	SRDA
Total Internal Reflection Fluorescence Microscopy	TIRFM
Thin Layer Chromatography	TLC
Ultraviolet	UV

Acknowledgements

I would first and foremost like to thank my supervisor Dr. Hans-Peter Loock for his support, insight, and careful guidance throughout my degree. I am grateful for his constant enthusiasm and patience throughout this project, which would not have been possible without him. Thank you also to my committee member Dr. Reuven Gordon for your helpful advice throughout this project.

I would like to acknowledge many of the staff who have been so helpful throughout my time here. Thank you to Nick Braam in the Physics electronics shop, and Mark Evans in the Chemistry electronics shop, for your help and guidance, and for making high-voltage less scary. I'd like to gratefully acknowledge Chris Secord and the machine shop for your help in 3D printing. Thank you also to Erin Hodgson for all your help navigating graduate school, thesis submission timelines, and beyond.

I would like to express my gratitude to the entire Loock Laser Lab, both past and present. Thank you to Adam and Travis for your mentorship in this project, and for never hesitating to accept a video-call and troubleshoot some hardware or code. Emma and Swapnil, I am grateful to have shared this journey of unpacking and starting up the lab here at UVic with the two of you, and couldn't have asked for better company along the way.

I would like to acknowledge my fellow graduate students in the Chemistry Department at UVic, who have made the university such an enjoyable place to go to everyday. A special thank you goes to Hayley, Chris, Kirsten, and Georgia for the coffee breaks, beach days, and games nights. My sincere thanks to my Greater Victoria family Callum, Brian, and Jess, for helping make Victoria a place I could call home.

Finally, I would like to acknowledge my family. To my dad Joel, thank you for always being there, whether it was advice on statistical methods, or your persistent encouragement and belief in me. To my mom Debi, I could not have succeeded without your unwavering love and kindness. Thank you to my brothers Adam and Nathaniel, for putting up with my antics, and being a source of joy and humour in my life.

Chapter 1

Introduction

Fluorescence detection is a powerful technique for identifying and quantifying chemical compounds in variety of environments and applications. Materials that fluoresce are ubiquitous in many fields of science including astronomy, biology, medicine, food science, and environmental studies – as well as in a variety of chemical fields, from fluorescence imaging to separation science.

Fluorescence spectroscopy methods are wide-ranging, and can be resolved in either spectral domain (e.g. laser induced fluorescence studies of molecular excited states), the spatial domain (fluorescence imaging), the temporal domain (fluorescence lifetime measurements), or a combination thereof. Spectral fluorescence methods include techniques in fluorescence spectroscopy where the primary goal is to obtain a fluorescence spectrum of the sample in the excitation, emission, or, in some cases, both dimensions. Spatial fluorescence techniques focus on capturing images of fluorescing materials in the *x*, *y*, and sometimes *z* spatial dimensions. Temporal fluorescence techniques include both, fast fluorescence lifetime measurements in the nanosecond domains, and fluorescence-based kinetic studies (microseconds or longer). Each fluorescence method utilizes these domains to find solutions to applications.

One common spectral fluorescence method includes laser induced fluorescence (LIF), which measures an emission spectrum at a single excitation wavelength using a laser. By limiting the excitation to just a single wavelength, the acquisition of emission spectra can occur fast enough to resolve fluorescence temporally over the course of a capillary electrophoresis (CE) separation, *i.e.* with a time resolution of higher than 1s. Fluorescence detectors using UV excitation are commonly included in commercial capillary electrophoresis systems and have been used extensively for the detection of DNA and protein.[1, 2]

The information content in a fluorescence measurement can be dramatically increased by acquiring emission spectra using many different excitation wavelengths which produces a two-dimensional contour of fluorescence called an excitation emission matrix (EEM). EEM spectroscopy can be highly resolved in both spectral domains and can be used to find the fluorescent fingerprint of molecules in complex mixtures. Its applications span the food industry,[3, 4] environmental monitoring,[5] and monitoring oil lubricant lifespans.[6, 7] Unfortunately, conventional EEM spectrometer designs have low temporal resolution, since typical EEM spectrometers (e.g., Varian Cary Eclipse) scan sequentially through both the emission and excitation, which can take between 20 minutes to an hour to obtain a single, high-resolution EEM spectrum. Newer designs of EEM spectrometers, such as the Horiba Aqualog, replace the emission scanning monochromator with a dispersive charge-coupled device (CCD) detection system, and can reduce acquisition time to a few minutes. Peng et al. also demonstrated a prototype design in which the excitation light source was replaced with a Michelson interferometer to decrease acquisition time using Fourier multiplexing.[8]

Recently, the Loock group has designed and patented an EEM spectrometer with a fully programmable light source that reduces the acquisition time for a single EEM 500-fold compared to conventional designs.[9] The light source takes advantage of the Hadamard-transform-based multiplexing, which uses sequences of excitation spectra, each consisting of a unique combination of wavelength channels.[10] This decrease in acquisition time allows EEM spectroscopy to be resolved in the temporal domain, and has since been applied to study the kinetics of stop-flow reactions,[11] as a detector for HPLC,[12] and is currently being used as an on-line monitor to study the degradation of oil lubricants in as-yet unpublished work from our colleague Travis Ferguson at Queen’s University. However, as of now, EEM spectroscopy is limited to sampling a single point in space and possesses no spatial resolution capabilities.

In the spatial domain, fluorescence spectroscopy has been used to image assays and gel electrophoresis (e.g., Southern,[13] northern blot[14]). DNA or RNA may be tagged or stained with a fluorophore, and the separated gel imaged.[15] The fluorophore’s emission highlights how far the DNA or RNA has traveled, and can be used to infer properties of the sample (molecular weight, charge etc.). In two dimensional difference gel electrophoresis (DiGE), multiple fluorophores may be used at different emission wavelengths,[16] however this technique is limited by the spectral resolution of the imaging spectrometer or camera. As a result, the dyes must have sufficiently different emission peaks to be resolved in the spectral domain. Almost all examples use labelling of target analytes with a fluorescence tag and there exist very few examples of spatially resolved fluorescence spectroscopy, using native fluorescence.

Fluorescence microscopy is perhaps the best-known example of imaging fluorescence. These methods provide high spatial resolution of samples such as tissue and cells tagged with fluorescent dyes in many biological applications. Wide-field fluorescence microscopy typically uses emission and excitation filters to select for a single fluorescent tag at a time and captures two dimensional images in the *x* and *y* dimensions. The spatial resolution of wide-field fluorescence microscopy is ultimately diffraction limited, although recent development in super-resolution imaging[17] and single molecule fluorescence detection[18, 19] have led to breakthroughs in biological imaging. Because the entire image is captured in a single integration time, wide-field microscopy is fast compared to other scanning techniques. Sinclair et al.[20] has developed a hyperspectral wide-field fluorescence microscope which couples a push-broom hyperspectral camera with an excitation laser and an objective. It can capture images with a spectral resolution of 3 nm across 490-900 nm (~136 channels), and a spatial resolution of 30 µm in a 20 mm by 60 mm area. The time to measure the entire hyperspectral image is 5 minutes, due to the limitations of scanning techniques. A popular example of a spatial scanning technique is confocal laser scanning microscopy (CLSM), where excitation and emission light pass through a pinhole to focus on a single spot on the sample. The *x* and *y* dimensions are raster scanned, and because the pinhole aperture focuses the light on a focal point, the depth of the sample can be measured in the *z* dimension as well. Typically, confocal microscopy is performed at a single excitation or emission, however designs with multiple lasers and/or multiple emission detectors are now available commercially (Leica). Because of the slow image acquisition, raster scanning limits this method to non-living static samples.

Total internal reflection fluorescence microscopy (TIRFM) is a method for imaging analytes of interest close to a cell's membrane, where a laser or arc lamp is shone through a glass slide beyond the critical angle, and the evanescent wave excites the fluorophores close to the glass slide. The emission is then captured through an objective lens and detected on a CCD camera. TIRFM has excellent sensitivity and spatial resolution however is typically used with only one or two fluorescent tags. Multispectral imaging is possible, if several excitation filters or several excitation lasers are used instead of just one.[21]

Considering the considerable advantages offered by EEM spectroscopy in identifying and quantifying molecules through their native fluorescence an ideal fluorescence imaging system would allow the recording of a full EEM for each pixel in an image. There are, indeed, several methods which combine EEM spectroscopy and imaging techniques to gain even more information in the spectral and spatial domains, however few achieve this with either good time resolution, or with EEM for each pixel in the image. In the food industry, Rahman et al.[22] evaluated the freshness of frozen shrimp by first sampling a single spatial point on the shrimp sample with a fiber probe coupled to an EEM spectrometer, and then separately imaging the shrimp at a single excitation wavelength and several emission wavelength using a CCD camera and a filter wheel. The dataset consists of a 3D hyperspectral image of x, y, and λ_{em}, and then separately a contour of the excitation and emission at a single x, y point on the shrimp. Abamba et al.[23] used a similar technique to identify adulterated extra-virgin olive oils, where the olive oil EEM spectrum was measured in a cuvette in the EEM spectrometer, and the sample was subsequently imaged with an RGB camera under UV and also visible lighting conditions. In medical applications, Herzka et al.[24] used magnetic resonance imaging (MRI) and EEM spectroscopy to demonstrate how EEM spectra could be used *in vivo* for tissue characterization. They coupled an EEM spectrometer to a bifurcated 7.0 m long fiber probe and used MRI to guide the probe through a plastic "phantom" (a stand-in for human tissue used commonly in medical imaging) and sampled fluorescent dyes within. Here, again, EEM spectroscopy is being used to provide high-resolution spectral information, while a separate imaging technique is required to provide any spatial information.

The goal of this work is to develop a fluorescence imaging system which rapidly captures data in five dimensions: the x and y spatial dimensions, the excitation and emission wavelengths, and time. A system of this kind could characterize complex mixtures of fluorophores which may not be spatially homogeneous. Presently, in imaging, microscopy, and assays, fluorescent analytes are required to be spectrally distinct from one another so that their emission spectra do not overlap. Including the additional excitation dimension allows for separation of these overlapping emission spectra. Imaging can also allow EEM spectroscopy to be applied to high throughput assays. If a series of samples can fit within the field of view of the hyperspectral camera and be illuminated by the light source, the samples can be measured in parallel, since every pixel in the image corresponds to an EEM. Leveraging fast acquisition techniques our group has developed (Hadamard Transform fluorescence EEM spectroscopy) allows for temporal resolution of the spectra, such that kinetics of complex reactions can now be studied in more dimensions than ever before.

1.1 Summary of Contributions

O. Katz designed and built the HT EEM imaging system and wrote the code for the acquisition and imaging processing graphical user interfaces described in Chapter 3. T. Ferguson consulted on the design and assisted in troubleshooting. The original programmable light source was developed by N. Andrews, H-P. Loock, and O. Reich, and filed as a patent in 2017. H-P. Loock conceived the HT EEM imaging system. A provisional patent was filed for the HT imaging system with the United States Patent Office on March 31, 2022. This imaging system was also presented at the 2022 Graduate Student Research Day at UVic.

O. Katz ran the temperature ramp experiments, collected the data, and analyzed the results described in Chapter 4. H-P. Loock conceived the experiment. The work was presented at the Canadian Chemistry Conference and Exhibition in Calgary, Canada on June 15, 2022, and at the Optical Industrial Optics Topical Meeting in Dublin, Ireland on July 26, 2022.

Chapter 2

Background

2.1 Fluorescence

Fluorescence is the absorption of a photon by a molecule or atom, followed by the emission of a photon at longer wavelength. Fluorescence occurs when an electron in the molecule or atom is excited to a higher molecular or atomic orbital and the corresponding electronically excited state relaxes to the ground state without a change in the spin state of the electron.[25] This process is shown schematically in the Jablonski diagram in Figure 2-1.

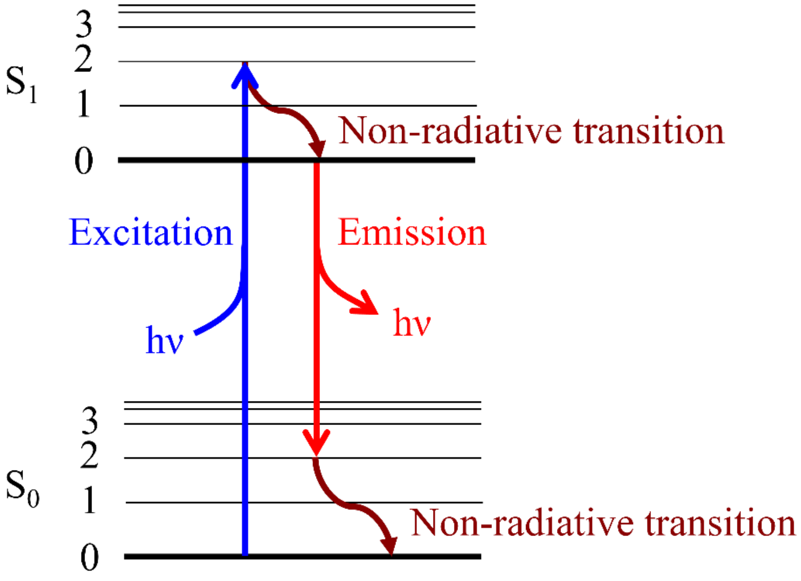

Figure 2-1 Jablonski Diagram of Fluorescence.

S_0 is denoted in the Jablonski diagram for the singlet ground state of a molecule. Upon excitation by a photon with energy $h\nu$, an electron is promoted to form an excited state of that energy. In the diagram it is shown by S_1 for the first singlet excited state, however formation of higher electronic excited states is also possible. Through non-radiative processes, the molecule can relax to the ground vibrational level of the excited state. Then, upon relaxation to the ground electronic state, a photon is emitted with the equivalent energy of the transition. The difference in the excitation energy and emission energy is known as the Stokes shift, and in general, the shift to longer emission wavelengths than excitation. Aside from the electronic structure of the sample molecule, the exact fluorescence emission energies are also determined by the Franck-Condon factors of the respective transitions (depending on the potential energy surfaces of both states involved) and the electronic environment, e.g., due to solvents or electric fields.

Several processes compete with the relaxation from the excited state to the electronic ground state. These include intersystem crossing where instead the electron changes spin states from the singlet state to the triplet state. The resulting emission from the triplet state is called phosphorescence. Another competitive process is internal conversion, where the excited state energy is lost to nonradiative relaxation in the vibrational states of the ground state. Energy transfer to another molecule, can also lead to de-excitation of the molecule and may lead to emission from the second molecule, such in a Förster Resonant Electron transfer (FRET) process or to quenching of fluorescence. Since not all photons which are absorbed necessarily result in an emission, this ratio of photons emitted to photons absorbed is described as the quantum yield,

$$\Phi = \frac{\text{photons emitted}}{\text{photons absorbed}} \tag{1}$$

where a molecule with a 100% quantum yield would emit a lower-energy photon for every photon absorbed.

Fluorescent molecules are also called fluorophores, and many organic fluorophores typically have a high degree of aromaticity in their structure. When the π orbitals of a molecule overlap, this is called conjugation. Conjugation stabilizes the π and π^* orbitals in the molecule and decreases the gap between the highest occupied molecular orbital (HOMO) and the lowest unoccupied molecular orbital (LUMO). The HOMO-LUMO gap dictates the minimum energy required to excite an electron from the ground state to the excited state. Many molecules with long π-conjugated systems are fluorophores with high quantum yield,[26] such as rhodamine dyes and fluorescein.

2.2 Fluorescence Spectroscopy

Spectroscopy is the study of electromagnetic radiation, and its absorption and emission in materials. Depending on the material properties of interest, one selects the corresponding wavelength range in the electromagnetic spectrum; for example, to identify functional groups in organic molecules, infrared absorbance spectroscopy is used to excite the corresponding molecular vibrations. To study fluorophores and their electronic excitation/relaxation energies, spectroscopists use fluorescence spectroscopy in the ultraviolet and visible range of the spectrum.

Instruments that measure a spectrum are called spectrometers and a diagram of a typical fluorescence emission spectrometer can be found in Figure 2-2. The instrument consists of a light source, a dispersive element to separate the emission into its component wavelengths, and a detector to measure the emission wavelengths. The single excitation wavelength is supplied usually by lasers which inherently have narrow linewidths. Alternatively, a broadband source coupled with either a filter or a monochromator can provide a sufficiently narrow excitation wavelength range. To disperse the emission light, a monochromator is used, such as the Czerny-Turner monochromator[27] shown in the example below. Light emitted from the sample passes through the entrance slit, is collimated, and then is dispersed off a diffraction grating. The dispersed light is then refocused, and a single wavelength passes through the narrow exit slit to the detector. The detector can be a single point broadband detector, such as photomultiplier tube (PMT), or a avalanche photodiode. To scan across the spectrum, the grating is moved, changing which wavelength of light passes through the slit to the detector.

Alternatively, a linear array photo detector, such as a CCD, can be placed in the plane of the exit slit, and the entire spectrum can be recorded at once across the pixels of the CCD.

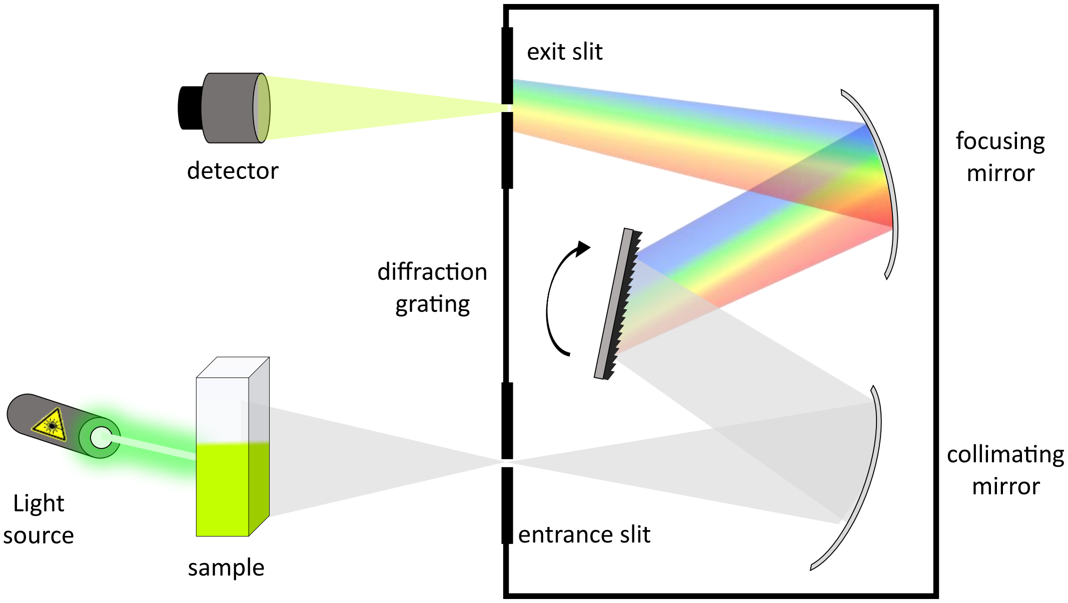

Figure 2-2 Diagram of a Typical Fluorescence Emission Spectrometer.

The spectrometer described above is one out of many possible designs, and there are countless variations by altering the detector, emission monochromator/geometry, and excitation light source. For example, time resolved fluorescence spectroscopy can measure the fluorescence decay, using a pulsed laser as the excitation light source and a variety of detection techniques (Time Correlated Single Photon Counting,[28] intensified CCD cameras,[29] etc.). Fluorescence excitation spectroscopy can also be performed, where instead the excitation wavelength is scanned using a monochromator and emission is only collected at a single wavelength, producing a line-scan of the excitation spectrum.[30]

The applications of fluorescence spectroscopy are far ranging. It is used in biology and medicine to tag relevant biomolecules,[31] perform single molecule detection,[32] and characterize dissolved organic matter (DOM) in the environment.[33, 34] Fluorescence excitation spectroscopy has applications in studying However, fluorescence is a phenomenon that is defined by two dimensions: excitation and emission. A technique where both dimensions are characterized can provide additional information that a 1-dimensional technique cannot.

2.3 Fluorescence Excitation Emission Matrix Spectroscopy

Fluorescence Excitation Emission Matrix (EEM) spectroscopy is a technique where a sample is excited across a range of wavelengths, and its emission is measured across a range of wavelengths. The series of spectra form a matrix, referred to as an EEM, and are plotted usually as a two-dimensional (2D) contour map or colour map. The height of the contour corresponds to the intensity at a given excitation and emission wavelength.

EEM spectroscopy is advantageous compared to one-dimensional (1D) spectroscopy such as either emission spectroscopy or excitation spectroscopy. In solutions with multiple fluorophores, their emission spectra can overlap, and peaks can be difficult to resolve. An example of this is shown in Figure 2-3, where on the left the emission spectrum of fluorescein and rhodamine B are overlapped such that only a single peak is visible. In EEM however, the spectra can be resolved such that two clear peaks are visible (shown in the right in Figure 2-3).

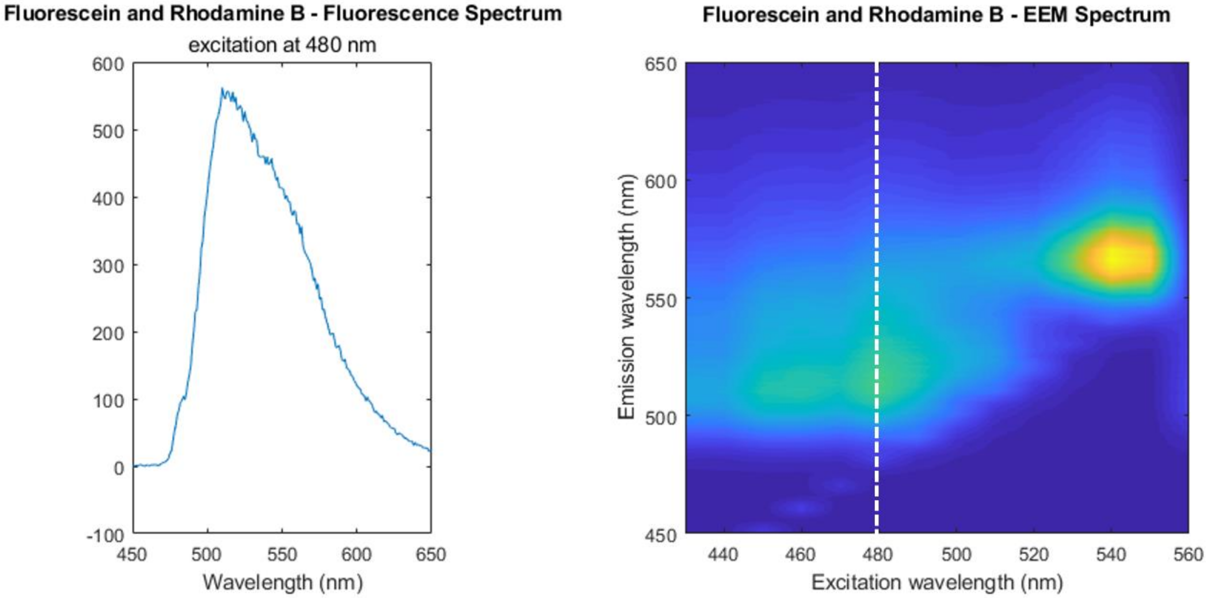

Figure 2-3 One-Dimensional Emission Spectrum vs. EEM of two fluorescent dyes.(Left) an emission spectrum where fluorescein and Rhodamine B are indistinguishable when excited at 480 nm. (Right) the corresponding EEM where fluorescein and rhodamine B have two distinctly separate peaks (a dotted line indicates the excitation wavelength of the emission spectrum).

One common design of an EEM spectrometer is shown in Figure 2-4. It consists of two monochromators, one for excitation and one for emission. The excitation monochromator selects for a single narrow excitation wavelength by dispersing light from a white light-source and passing only a narrow portion through the exit slit. This excitation light is used to excite the fluorescent sample, and the emission is then collected at 90°. The emission light is subsequently passed through the entrance slit of the second monochromator, which selects for a single narrow wavelength, dispersing the emission light and passing only a narrow portion through the exit slit towards a broadband detector such as a PMT.

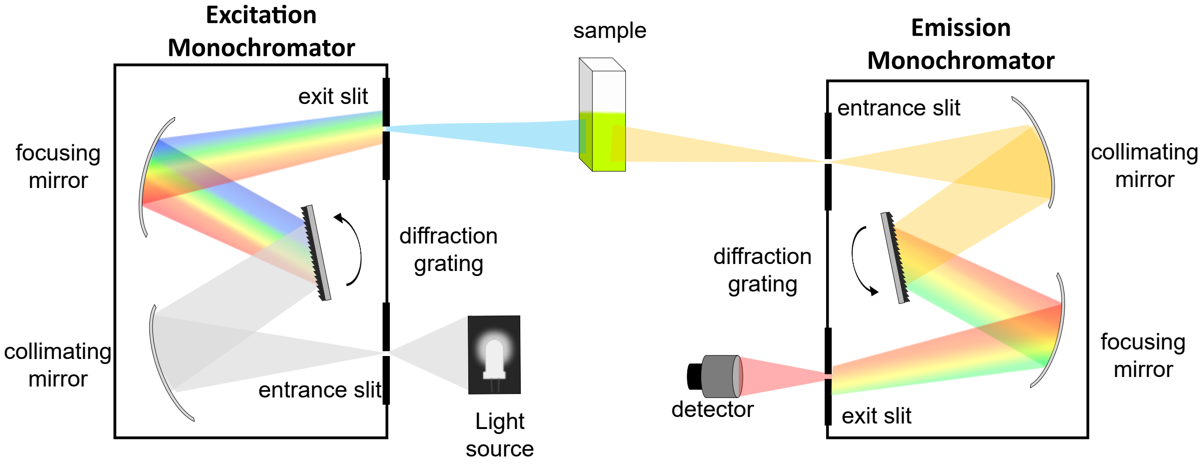

Figure 2-4 Schematic for a two-monochromator EEM spectrometer. By moving the grating, the excitation and emission wavelengths can be selected.

EEM spectroscopy provides high-resolution spectral information, at the expense of acquisition time. To collect a single EEM spectrum, the spectrometer must scan through each excitation and emission wavelength sequentially, such that a single high resolution spectrum can take 30 minutes to over an hour to acquire a single spectrum.[35] As a result, EEM spectroscopy is either limited to static, unchanging systems, or offline reaction analysis where aliquots must be sampled and the reaction quenched to monitor kinetics - a time-consuming, and error-prone process. Other EEM techniques replace the emission monochromator with a CCD spectrometer so that each emission wavelength can be measured simultaneously. Even so, these systems are still wasteful in light throughput since each acquisition only utilizes a fraction of the excitation light per integration time.

To address the low data acquisition rate the Loock group increased the “photon-efficiency” of the excitation light source using a multiplexing technique called Hadamard-transform, and thereby decreased the acquisition time of EEM spectroscopy. To understand this new spectroscopic method, Hadamard multiplexing is explained in the following section.

2.4 Hadamard Multiplexing

Multiplexing is the process of combining several signals to be measured at once by a system. The advantage of multiplexing is most apparent in the improved signal-to-noise ratio (SNR), called Fellgett’s advantage[36] or the multiplex advantage. One such multiplexing technique is based on the Hadamard Transform (HT) and is used in image processing,[37] quantum computations,[38] and importantly, spectroscopy.[10, 11, 39] To help explain the Hadamard Transform, authors Graff[40] and also Marshall[41] have used a thought experiment where *n* rocks are to be weighed *j* times on a one-pan scale to determine their mass. This can best be described with linear algebra, as follows,

$$\mathbf{H} \times \mathbf{r} = \mathbf{m} \pm \mathbf{e} \tag{2}$$

Where **H** is a conversion matrix, dictating on the j^{th} measurement which of the *n* rocks is weighed. **r** is a vector for the calculated weight of the n^{th} rock, and **m** is a vector containing of the j^{th} measurements. **e** is the error associated with each measurement, which is to be minimized. Assuming the scale has a constant intrinsic error of ±0.1 g, then four rocks can be weighed, one at a time, and the four measurements can be read from the scale. The true masses of rocks are 9, 6, 3, and 4 grams.

$$\begin{bmatrix} 1 & 0 & 0 & 0 \\ 0 & 1 & 0 & 0 \\ 0 & 0 & 1 & 0 \\ 0 & 0 & 0 & 1 \end{bmatrix} \begin{bmatrix} r_1 \\ r_2 \\ r_3 \\ r_4 \end{bmatrix} = \begin{bmatrix} 9 \\ 6 \\ 3 \\ 4 \end{bmatrix} \pm \begin{bmatrix} 0.1 \\ 0.1 \\ 0.1 \\ 0.1 \end{bmatrix} \tag{3}$$

Where the conversion matrix describes for which of the four measurements (rows) weigh a given rock (columns). Because a single rock is weighed at a time, this is described by the identity matrix. To determine the mass of each rock r_n, the conversion matrix must be multiplied by the inverse of itself, which is trivial since the inverse of the identity matrix is itself. As a result, each of the four masses measured corresponds to the mass of each rock.

$$\begin{bmatrix} 1 & 0 & 0 & 0 \\ 0 & 1 & 0 & 0 \\ 0 & 0 & 1 & 0 \\ 0 & 0 & 0 & 1 \end{bmatrix} \begin{bmatrix} r_1 \\ r_2 \\ r_3 \\ r_4 \end{bmatrix} = \begin{bmatrix} 1 & 0 & 0 & 0 \\ 0 & 1 & 0 & 0 \\ 0 & 0 & 1 & 0 \\ 0 & 0 & 0 & 1 \end{bmatrix} \begin{bmatrix} 9.0 \pm 0.1 \\ 6.0 \pm 0.1 \\ 3.0 \pm 0.1 \\ 4.0 \pm 0.1 \end{bmatrix} \tag{4}$$

$$\begin{bmatrix} r_1 \\ r_2 \\ r_3 \\ r_4 \end{bmatrix} = \begin{bmatrix} 9.0 \pm 0.1 \\ 6.0 \pm 0.1 \\ 3.0 \pm 0.1 \\ 4.0 \pm 0.1 \end{bmatrix}$$

What if instead of placing only one rock on the scale at a time, multiple rocks are measured at once? Replicates can be obtained by multiplexing the measurements, if we are able to work out what the original masses were for each rock. An example is shown below.

$$\begin{bmatrix} 0 & 1 & 1 & 1 \\ 1 & 1 & 0 & 0 \\ 1 & 0 & 1 & 0 \\ 1 & 0 & 0 & 1 \end{bmatrix} \begin{bmatrix} r_1 \\ r_2 \\ r_3 \\ r_4 \end{bmatrix} = \begin{bmatrix} 13 \\ 15 \\ 12 \\ 13 \end{bmatrix} \pm \begin{bmatrix} 0.1 \\ 0.1 \\ 0.1 \\ 0.1 \end{bmatrix} \tag{5}$$

Here, in the first measurement, all four rocks are placed on the scale, and in the second measurement only the first two rocks are placed on the scale, and so on. Note the intrinsic error remains the same for the four measurements. To solve for the mass of each rock, the measurements must be multiplied by the inverse matrix. Here, it is important to select a matrix that is in fact invertible, such that $\mathbf{HH^{-1}} = \mathrm{I}$. The inverse of the conversion matrix is found to be

$$\mathbf{H}^{-1} = \frac{1}{3}\times\begin{bmatrix} -1 & 1 & 1 & 1 \\ 1 & 2 & -1 & -1 \\ 1 & -1 & 2 & -1 \\ 1 & -1 & -1 & 2 \end{bmatrix} \qquad (6)$$

Applying the conversion matrix to both sides of the equation allows the masses of each rock to be found.

$$\begin{bmatrix} r_1 \\ r_2 \\ r_3 \\ r_4 \end{bmatrix} = \begin{bmatrix} -1 & 1 & 1 & 1 \\ 1 & 2 & -1 & -1 \\ 1 & -1 & 2 & -1 \\ 1 & -1 & -1 & 2 \end{bmatrix}\begin{bmatrix} 13.0\pm0.1 \\ 15.0\pm0.1 \\ 12.0\pm0.1 \\ 13.0\pm0.1 \end{bmatrix} = \begin{bmatrix} 9.0\pm0.067 \\ 6.0\pm0.088 \\ 3.0\pm0.088 \\ 4.0\pm0.088 \end{bmatrix} \qquad (7)$$

The mass of the rocks has been found, but the mean squared error of all four measurements has decreased to 0.007 from 0.01. This best illustrates the multiplex advantage: because each rock is weighed multiple times, the uncertainty in the measurement is reduced and a more accurate value can be achieved.

This analogy can be applied to spectroscopy, where a typical sequentially scanning detector measures light intensity only one wavelength at a time (akin to the first example with the rocks). By instead measuring a signal arising from several wavelengths of light at once and then decoding the signal, one can get an increase in the signal-to-noise ratio (where the noise is the associated error in a spectrometer). To encode and decode a signal using the HT, the signal is multiplied by a Hadamard Matrix, $\mathbf{H}_m^*$, of size $m \times m$. In this work and previous works by the Loock Group,[10-12, 42] the Hadamard matrices are of the Paley type I construction,[43] where $\mathbf{H}_4^*$, can be defined as:

$$\mathbf{H}_4^* = \begin{pmatrix} 1 & 1 & 1 & 1 \\ 1 & -1 & 1 & -1 \\ 1 & -1 & -1 & 1 \\ 1 & 1 & -1 & -1 \end{pmatrix} \qquad (8)$$

In a two-detector spectroscopic setup, one detector measures the “1” signal, and the second detector measures the “–1” signal simultaneously. In the application of HT to fluorescence EEM spectroscopy, a two detector is problematic, since the sample can either be excited (1) or not excited (0)[*]. Instead, the S-matrix $\mathbf{H}_n$ can be used, by setting all 1 elements to 0 and all –1 elements to 1. The matrix is also truncated by removing the first row and column, such that a $m\times m$ size Hadamard matrix becomes a $n\times n$ matrix, where $n = m - 1$.

$$\mathbf{H}_4^* = \begin{pmatrix} 1 & 1 & 1 & 1 \\ 1 & -1 & 1 & -1 \\ 1 & -1 & -1 & 1 \\ 1 & 1 & -1 & -1 \end{pmatrix} \xrightarrow{1\to 0,-1\to 1} \mathbf{H}_3 = \begin{pmatrix} 1 & 0 & 1 \\ 1 & 1 & 0 \\ 0 & 1 & 1 \end{pmatrix} \tag{9}$$

To encode a light source using the Hadamard transform, the light source spectrum with *i* number of excitation wavelengths is modulated in the time domain, such that each exposure of the light irradiates with a different combination of wavelengths, according to the columns of $\mathbf{H}_n$. **S** is the light source matrix with *n* identical rows, where the columns are the spectrum of a light source with *i* wavelengths channels ($n \equiv i$, however *i* is excitation wavelengths while *n* refers to modulated spectra). The element-wise product with $\mathbf{H}_n$ gives the sequence of modulated spectra

$$\mathbf{H}_n \circ \mathbf{S} = \mathbf{H}_n \begin{bmatrix} S_{11} & S_{12} & \cdots & S_{1i} \\ \vdots & & & \vdots \\ S_{n1} & S_{n2} & \cdots & S_{ni} \end{bmatrix} = \begin{bmatrix} H_{11}S_{11} & H_{12}S_{12} & \cdots & H_{1n}S_{1i} \\ \vdots & & & \vdots \\ H_{n1}S_{n1} & H_{n2}S_{n2} & \cdots & H_{nn}S_{ni} \end{bmatrix} \tag{10}$$

If the integrated intensity of each modulated spectrum is measured, and then multiplied by the inverse Hadamard matrix, the original light source spectrum can be retrieved.

---

[*] It is possible, though, to excite the sample first with wavelengths given by the Hadamard matrix and then next by a pattern that is derived by switching all values for 1 and 0.

$$\begin{bmatrix} S_1 \\ \vdots \\ S_n \end{bmatrix} = \mathbf{H}^{-1} \times \begin{bmatrix} \sum_{k=1}^{n} H_{1k} S_k \\ \vdots \\ \sum_{k=1}^{n} H_{nk} S_k \end{bmatrix} \tag{11}$$

The Hadamard transformed source spectra **H°S** can now be used to excite fluorescence. For each column in the matrix the fluorescence emission spectrum is measured, e.g., using an array detector. The matrix **F** describes *n* measured emission spectra with *j* emission wavelengths, that have been excited with the corresponding *n*th modulated excitation spectrum. If **F** is the measured encoded matrix, then,

$$\begin{bmatrix} f_{11} & f_{12} & \cdots & f_{1j} \\ \vdots & & & \vdots \\ f_{n1} & f_{n2} & \cdots & f_{nj} \end{bmatrix} = \begin{bmatrix} H_{11}S_{11} & H_{12}S_{12} & \cdots & H_{1n}S_{1i} \\ \vdots & & & \vdots \\ H_{n1}S_{n1} & H_{n2}S_{n2} & \cdots & H_{nn}S_{ni} \end{bmatrix} \times \mathbf{M}_{i,j} \tag{12}$$
$$\mathbf{F} = \mathbf{HS} \times \mathbf{M}$$

Equation (12) illustrates that the fluorescence spectra in **F** collected by sequential excitation with “barcodes” corresponding to the columns in the **HS** matrix are governed by the EEM spectrum **M**, where *j* is the emission wavelengths and *i* is the excitation wavelengths. To find the **M** from the experimentally determined **F**, the measured spectra are multiplied by the inverse of the Hadamard matrix

$$\mathbf{M} = \left[\mathbf{HS}\right]^{-1} \times \mathbf{F} \tag{13}$$

As mentioned earlier, acquiring spectra in this manner increases SNR though a much greater photon throughput. This advantage is especially relevant to fluorescence EEM spectroscopy where spectra take a long time to acquire. Of course, increased SNR at the same data acquisition time can be traded off with a shorter acquisition time at the same SNR.

2.5 Hadamard Transform Excitation Emission Matrix Spectroscopy

The manner in which a light source is practically encoded using the Hadamard Transform is the subject of ongoing research in our group. We developed two complementary methods to generate multi wavelength light with fully programmable light sources. One method (developed second) is simply based on a battery of narrow bandwidth light sources such as (UV-)LEDs or lasers that are controlled by corresponding drivers. The other method (developed first) instead uses a broadband lights source, here an LED, that is disbursed on a MEMS device, which allows for a selection of wavelengths. Devices based on other spatial light modulators, or Fourier-transform optics are conceivable.

Our group also demonstrated that, using Hadamard Transform Excitation Emission Matrix (HT-EEM) spectroscopy, acquisition times are drastically reduced up to 500-fold from conventional sequential scanning methods.[10] We next describe a previously developed HT-EEM spectrometer.

White light from a light emitting diode (LED) is dispersed spatially across a digital micromirror device (DMD, sometimes called a digital micromirror array or DMA). The array consists of microscopic mirrors which can be flipped into an “on” or “off” state, in such a way that wavelengths of the spatially dispersed light can be turned on or off to irradiate the sample. Emission is then recorded using a CCD spectrometer. A schematic of the HT-EEM spectrometer can be seen in Figure 2-5.

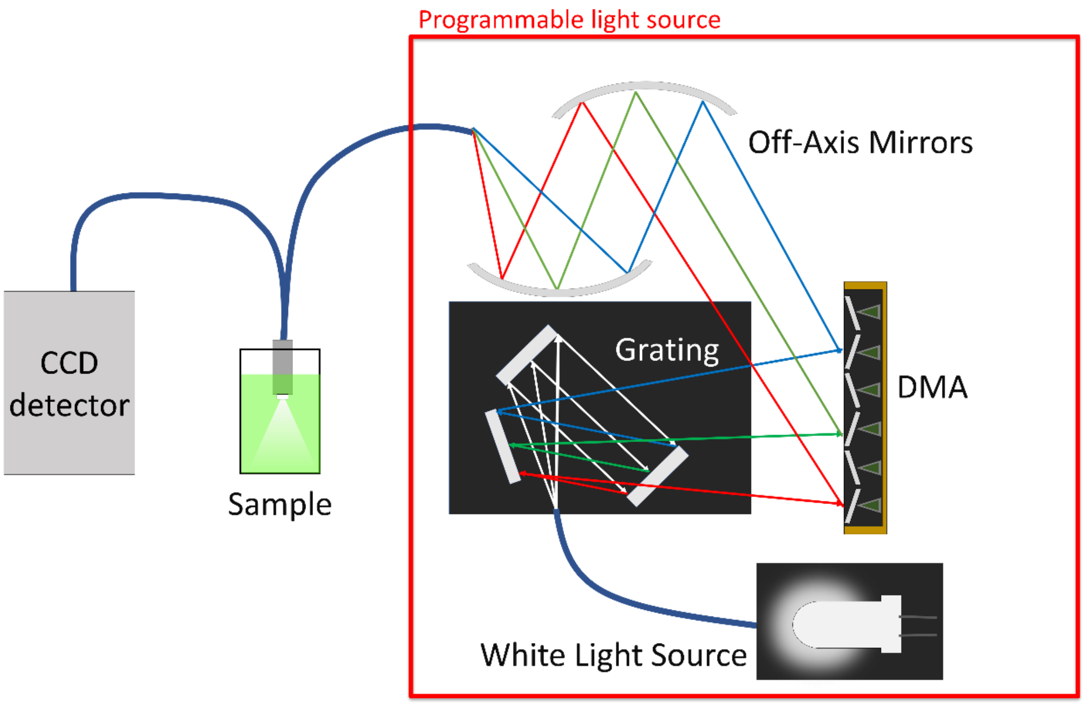

Figure 2-5 Schematic of a Hadamard transform EEM spectrometer. Light from an LED source is directed to a cannibalized spectrometer where it is dispersed into a rainbow of colours that is projected on a digital micromirror array (DMA).

A column of the **H** matrix is displayed on the DMA, where a 1 is a mirror column in the “on” state and a 0 is the “off” state. The columns are displayed sequentially through time and an emission spectrum is recorded at each illumination, thus measuring the columns of the **F** matrix. An illustration of the masks displayed on the DMD can be seen in Figure 2-6.

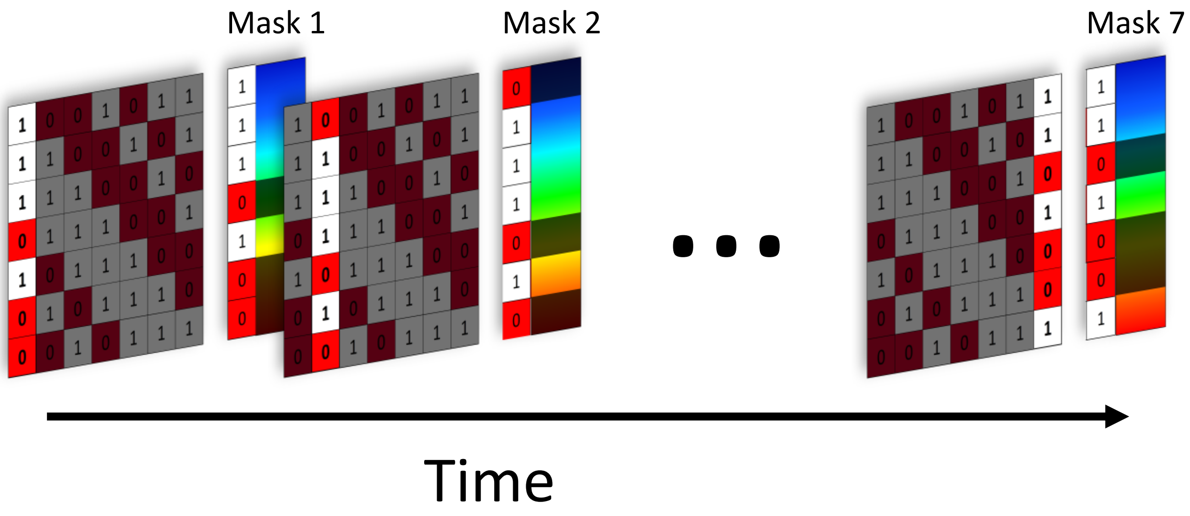

Figure 2-6 7×7 Hadamard Mask sequence. One column of the Hadamard S-matrix is displayed at each integration, and the corresponding DMD mirror columns are flipped either on (1) or off (0).

With this the HT-EEM spectrometer, we have been able to record EEMs with 127 excitation wavelengths in as little as 1.6 seconds.[11] The device has been applied to study several systems where fluorescence is changing dynamically and would change too fast to acquire using conventional sequential scanning techniques. For example, the demetallation of chlorophyll-a into pheophytin-a has been studied in the past, however to monitor the kinetics, aliquots had to be quenched and then measured offline, limiting the time resolution achievable(16 samples in 9.5 hours).[44] Using HT-EEM spectroscopy, our group acquires EEM spectra continuously throughout the reaction, yielding a much greater time resolution (600 EEM spectra in 2.5 hours) with none of the work required to quench the reaction.[10]

Another configuration of the HT-EEM spectrometer replaces the DMD light source with a bank of seven programmable ultraviolet (UV) LEDs, allowing with narrow (~15 nm) bandwidths. This configuration can study fluorophores with excitation into the UV region, which was previously inaccessible due to a coating on the DMD mirrors. The spectrometer was used to detect analytes eluting off a high-performance liquid chromatography (HPLC) column, acquiring EEM at a rate of 6 spectra/second.[12] Because of the added dimensionality in EEM as compared to one-dimensional spectroscopic techniques, the spectrometer was able to identify the coelution of two fluorophores which otherwise appeared as a single peak in the absorbance chromatogram.

Hadamard Transform is a powerful tool for studying the kinetics of solutions, however it lacks the ability to resolve spatial details in a sample, such as inhomogeneity or changes in features across space. While it is conceivable that one can raster-scan a large sample using the fiber-probe developed for previous studies, it is much more elegant to combine our programmable light source with a hyperspectral camera.

We next review, briefly, the most common techniques used in hyperspectral imaging.

2.6 Hyperspectral Imaging

Imagers such as CCD camera sensors capture the intensity of light across a 2D array of pixels, building an image with dimensions x and y. Monochrome imagers are sensitive to a broad spectrum of light, and so only provide the value for the integrated intensity across that range. Hyperspectral imaging is a technique which attempts to resolve the spectrum of light at each pixel in the image, yielding a three-dimensional (3D) dataset (also called a data-cube) of dimensions (x, y, λ). Modern commercial colour cameras provide a limited amount of “hyperspectral” or “multispectral” data, as they consist of filter arrays which are sensitive to broad bands in the visible spectrum that approximate the human eye’s sensitivity to red, green, and blue light (RGB). However, there is no strict definition on how many wavelength channels constitute a hyperspectral image vs. a multispectral image. Broadly, hyperspectral imaging techniques can be divided into two categories, scanning techniques and snapshot techniques,[45] and are illustrated in Figure 2-7. A scanning technique builds the data-cube over the course of several integrations, sacrificing temporal resolution for improved spatial or spectral resolution. Spatial scanning methods include point-scanning, where the pinhole aperture raster scans through the x and then the y pixels using two mirror galvanometers, and a spectrum is dispersed and measured on a linear array detector. Point-scanning detectors were often mounted to satellites and satellites for environmental surveys, moving a mirror perpendicular to the direction of flight.[46] They are also employed in cancer research for the imaging of tumours.[47]

With the advent of 2D CCD detectors, came another spatial scanning method called the line-scan, where light from a slit aperture is dispersed by a prism or a grating onto a 2D CCD array, allowing the measurement of both x and λ simultaneously. The camera (or alternatively the imaging stage) is translated in the y direction to capture the entire data-cube. The line-scan method is so aptly nicknamed the "push-broom" method. Push-broom hyperspectral imaging has applications in airborne environmental surveys of deforestation,[48] the fishing industry,[49, 50] and waste management.[51] There even exist schematics for "do-it-yourself" push-broom hyperspectral imagers.[52]

Wavelength scanning techniques involve using the entire 2D detector array to measure the spatial x and y dimensions simultaneously, capturing several integrations over time to build the λ dimension. This is often achieved using filter wheels where each image is captured with a different bandpass filter. These hyperspectral imagers have been used on several rovers for exploration on Mars.[53-55]

Snapshot techniques capture the entire data-cube in a single integration. Snapshot hyperspectral imaging sacrifices spatial and/or spectral resolution in exchange for vastly improved temporal resolution compared to scanning techniques, as only a single integration time is necessary. As will be explained in the following chapters, our ultimate goal is to use a hyperspectral imager to capture the emission in HT-EEM spectroscopy. The overall advantage of HT is the decreased acquisition time, which is what informs the decision in the selection of a hyperspectral imaging technique. Snapshot detection methods are the most favourable in this application because they can best capitalize on the speed advantage offered by HT, albeit at the expense of spectral and/or spatial resolution.

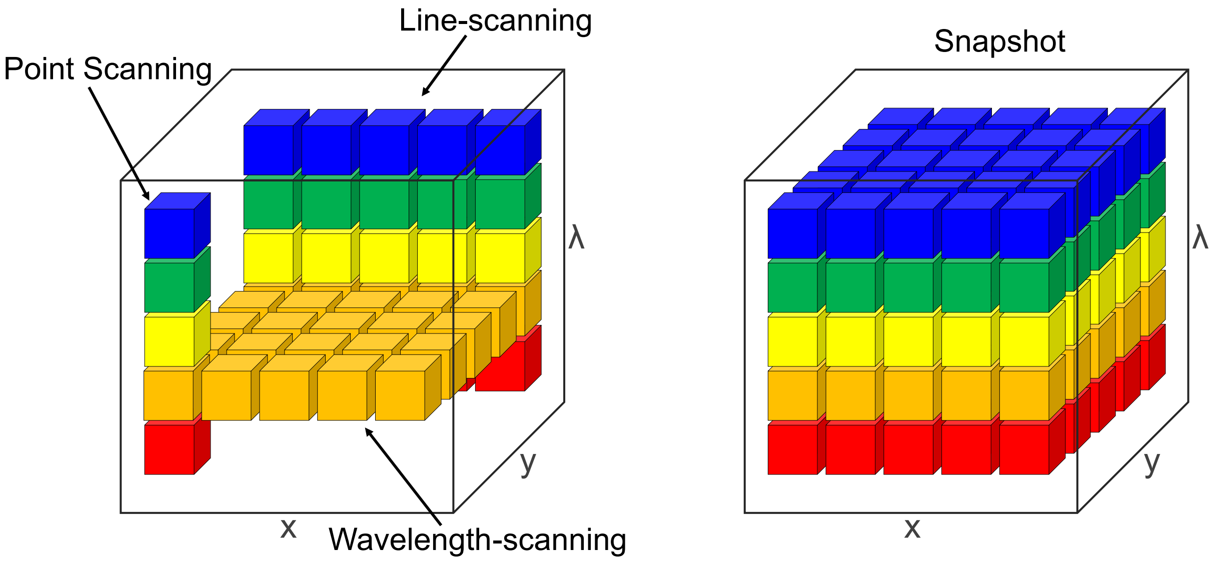

Figure 2-7 Illustration of Scanning vs. Snapshot Devices. The blocks represent cells of the data-cube captured in each integration. Figure adapted from Hagen and Kudenov.[45]

The techniques for snapshot hyperspectral imaging are varied. Integral field spectrometry (IFS), contains an imager that is composed of an array of either mirrors (IFS-M),[56] fibers (IFS-F),[57]or lenses (IFS-L),[58] which are then dispersed over a portion of the imaging sensor. IFS techniques are often used in astronomy and produce "tall" data-cubes with high spectral resolution but comparably poor spatial resolution (fewer pixels). Other snapshot techniques produce "wide" data-cubes, that have good spatial resolution in exchange for few spectral channels. These include multispectral beamsplitting (MSBS),[59] where a series of dichroic beam splitters (long-pass filters with different cut-off wavelengths) sequentially direct images in different spectral bands to separate monochromatic imaging detectors. High spatial resolution is achievable, however light loss from successive passes through the beam splitters limits the technique to typically four channels.[60] One of the most common techniques for compact spectral imagers is the spectrally resolving detector array (SRDA). It consists of a detector with an array of filters individually laid upon each detector pixel, similar to the Bayer filters[61] that are used in typical commercial "colour" cameras - just with more wavelength channels.[62] The relatively low cost and ubiquity of the SRDA detector makes it the preferred method for hyperspectral imaging in this work.

When applied to fluorescence imaging any of these hyperspectral imaging systems produces 3-dimensional (x, y, λ_{em}) data cubes. In combination with the programmable light source (λ_{ex}) we now have access to a 4-dimensional data “cube” that can be acquired at a high rate (t). Using typical numbers for the size of these arrays one can estimate the size of the data cube and therefore the memory and storage requirements. Assuming an image intensity depth of 8-bit (1 byte, 256 intensity gradations), and 256×256 pixels (65,536 pixels = 0.065 megapixel = 0.065 MB at 8-bit) with just 8 colour channels results in a hyperspectral data cube of 0.52 MB that is acquired with each exposure. Considering that between 8 and 128 excitation channels can be used, the size of the 4D data cube increases accordingly to 4 MB to 66MB. In a time series of, say 100 such 4D data cubes we quickly run into data management and processing issues.

Parallel factor (PARAFAC) analysis is then used on the 5D - data cube to help identify the EEM spectra of the different fluorophores and decompose the EEM spectra of the mixtures into a linear combination of the EEM spectra of the chemical constituents (the “components"). The group has previously shown that the linear weighting factors (the “scores”) arising from the PARAFAC analysis can be used to quantify the changing concentration of the respective fluorophores in solution.

2.7 Parallel Factor Analysis (PARAFAC)

Parallel factor analysis (PARAFAC) is a tensor-rank-decomposition method for fitting multi-way datasets. It is a useful tool in analyzing EEM, where a dataset often has three or more dimensions. For example, if a series of samples are analyzed with EEM spectroscopy, then the dataset $\underline{\mathbf{X}}$ would be three dimensional: excitation, emission, and sample number. PARAFAC models $\underline{\mathbf{X}}$ as the sum of the Kronecker product of series of three orthogonal component vectors **a**, **b**, and **c** as follows,

$$\underline{\mathbf{X}} = \sum_{n=1}^{N} \mathbf{a}_n \otimes \mathbf{b}_n \otimes \mathbf{c}_n \qquad (14)$$

Where N is the number of unique components. The model can also be described in terms of the elements of $\underline{\mathbf{X}}$,

$$x_{ijk} = \sum_{n=1}^{N} a_{in} b_{jn} c_{kn} + e_{ijk} \tag{15}$$

Where every element x_{ijk} is equal to the sum and product of a_{in}, b_{jn}, and c_{kn}, and some residual error e_{ijk} which is to be minimized using an alternating least squares (ALS) method.[63] The PARAFAC model is described graphically in Figure 2-8, where $\underline{\mathbf{X}}$ is some three dimensional dataset (shown as a cube), the component vectors are spatially orthogonal lines, and the unexplained error is a cube which is to be minimized.

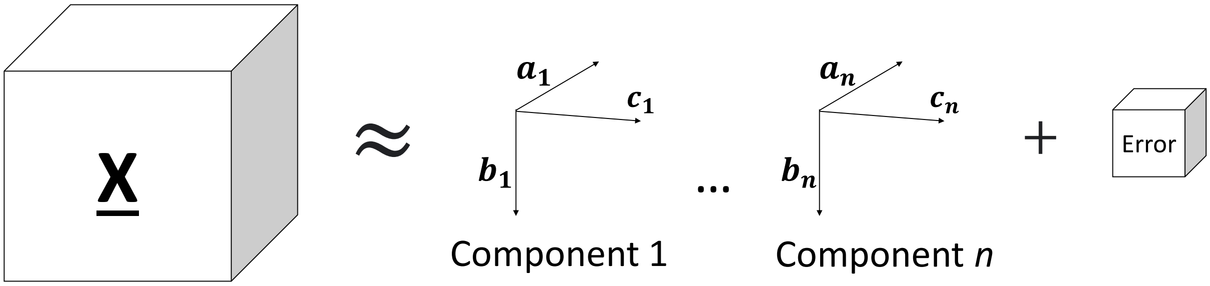

Figure 2-8 Graphical Representation of PARAFAC.

A PARAFAC model of an EEM dataset would result in component vectors which explain the excitation, emission, and “concentration” or signal intensity for each of the constituents or components. The number of components is estimated by the user, and a good fit is characterized by the assignment of a unique fluorophore to one of the components.

In HT-EEM spectroscopy, the third dimension is treated as time, such as in a chromatogram or a kinetic experiment. PARAFAC is a generalization of principal component analysis (PCA) for higher order arrays. Thus, it can be used not just for three-way arrays as shown here but four-way and five-way arrays (and beyond). This is relevant to our goals of imaging EEM spatially, because PARAFAC can explain the spatial dimension as another vector.

Chapter 3

Five Dimensional Hadamard-Transform Fluorescence Imaging

The methods developed by the Loock Lab as described in Chapter 2 have introduced the possibility of Hadamard Transform Excitation-Emission Matrix (HT-EEM) fluorescence spectroscopy in its demonstration to online monitoring and kinetics. However, current methods only provide single point detection; they do not supply any spatial information. In this chapter, I will introduce an instrument I have built that combines the previous HT-EEM method using a custom built programmable light source with a hyperspectral camera, to obtain spatial data as well as EEM spectral data.

The instrument consists of two parts: a programmable excitation light source, and a hyperspectral camera. Broadly, the programmable light source is responsible for modulating excitation light and delivering it to the sample, while the hyperspectral camera captures the corresponding emission light, and resolving it across two spatial dimensions *x* and y, while also providing a low-resolution spectrum for each pixel. A diagram of the imaging system can be seen in Figure 3-1, and each part will then be discussed in detail.

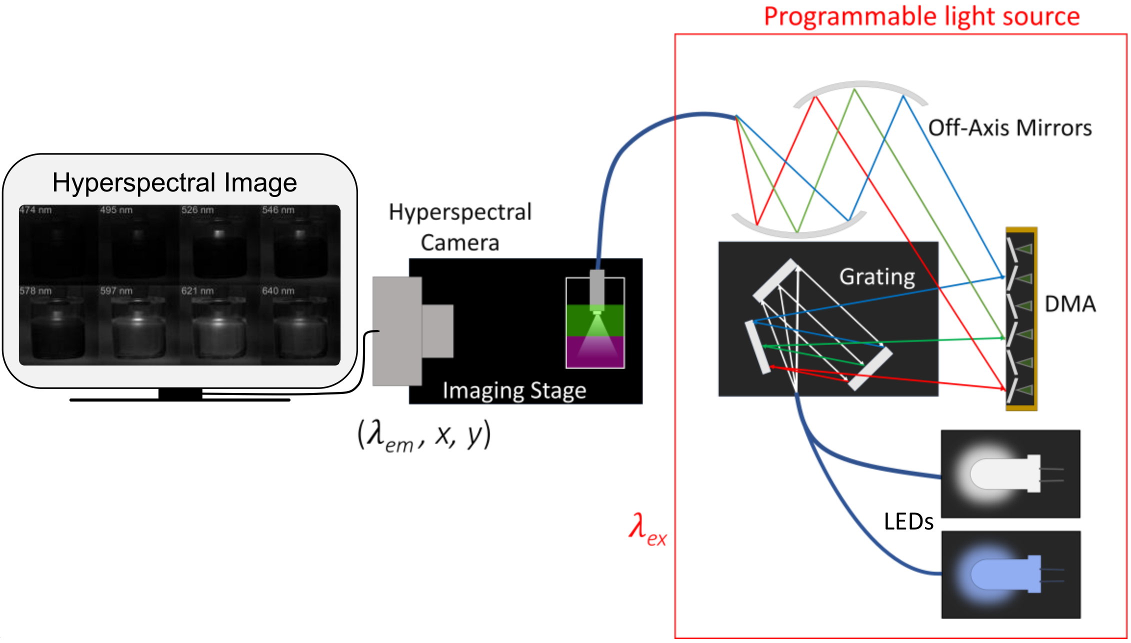

Figure 3-1 Diagram of the 5D HT Imaging System. The programmable light source modulates the excitation light, while the hyperspectral camera captures the emission and *x* and and *y* spatial information.

3.1 Programmable Light Source

The programmable light source supplies the Hadamard encoded excitation light to the sample and consists of an LED light source and entrance slit, a spectrograph for dispersing the light, a digital micromirror device (DMD), focusing optics, and a bifurcated fibre probe to deliver the light to the sample. Each of these components will be discussed in detail.

3.1.1 Combination Blue-White LED and Entrance Slit

In previous iterations of this programmable light source a white light source is coupled to a fiber bundle. The fibers in this bundle were arranged into a vertical stack on the other end of the bundle.[10, 11] By grouping the fibers in this manner, they form a slit with a narrow width equal to the fiber core diameter. A narrow entrance slit translates to better spectral resolution. Broadband LEDs such as the Thorlabs fiber-coupled “warm” white LED pictured in Figure 3-2 have been used previously as the white light source.

While the appearance of the light colour temperature is a warm white the spectrum is not uniformly flat. The light source actually consists of a 450 nm LED which optically stimulates emission of a phosphor. The resulting spectrum shows a comparably sharp peak at 450 nm and a broad emission from 500 nm to around 700 nm.

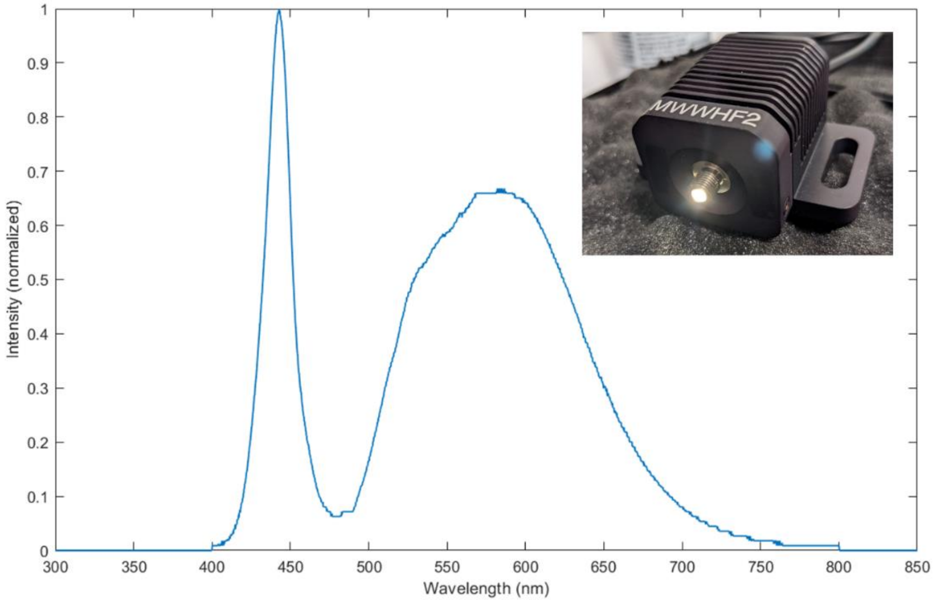

Figure 3-2 Normalized spectrum of warm white broadband LED.(Inset) fiber coupled LED, mounted in a heatsink. Spectrum obtained from manufacturer specifications (Thorlabs).

Most commercial LEDs have a gap at around 470 nm in their spectrum between the maximum wavelength of the blue LED and the phosphor emission. Eliminating this gap would allow for more uniform light intensity across the spectrum and is the motivation behind a new combination blue-white LED light source described below.

The concept behind the combination blue-white LED light source is to bifurcate the entrance slit fibers into two bundles: one that is coupled to a broadband white LED (MCWHF2, Thorlabs), and a second that is coupled to a blue LED (M470F3, Thorlabs) whose emission corresponds to the 470 nm gap in the broadband LED. An illustration of the design can be found in Figure 3-3.

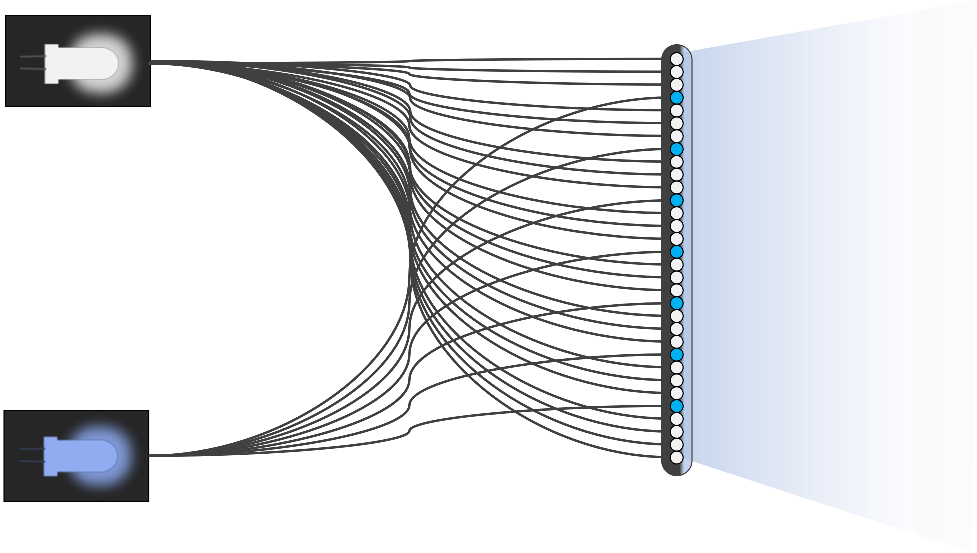

Figure 3-3 Diagram of the combination blue-white LED entrance slit. the white and blue LEDs are coupled to bundles of 25 and 7 fibers, respectively.

A multimode optical fiber (numerical aperture 0.22, High -OH, part number FVP100110125, Polymicro Technologies) was chosen as the fiber to make the entrance slit. This fiber was specifically chosen for its core, cladding, and coating diameters. The cladding and polyimide coating diameters (110 μm and 124 μm respectively) were relatively thin in comparison to the core diameter of the fiber (100 μm). A thinner coating and cladding means more fibers can be stacked into the length of the entrance slit, and so a greater light throughput can be achieved. One can also think about the cross-sectional area of each fiber: only the core will emit light, and so any cladding or coating is essentially dead area to be minimized. The polyimide coating also contributed to the fiber's flexibility.

To hold the fibers in a vertical arrangement, a custom fiber mount was designed in Fusion 360 and printed with a 3D printer. The mount was designed to clamp the fibers flat in a 6 mm × 3.35 mm × 25 mm trough with a separate 3D printed filler piece. A space in the mount was left for a setscrew to hold the mount onto the spectrograph body and align it with the rest of the optics. The fiber mount rendering is shown in Figure 3-4 (A) and the 3D printed mount in Figure 3-4 (B).

The fiber was cut into 32 strands approximately 50 cm in length, and then epoxied into the fiber mount. The ends were cleaved and polished, and then the fibers were then carefully separated into the bundles for the white and blue LEDs, consisting of 25 and 7 fibers, respectively. The rationale for the size of these bundles is as follows:

1. Since the total slit length cannot exceed 4 mm (the diameter of the entrance aperture of the spectrograph), the outer diameter of the fibers (124 µm) dictates that total number of fibers is 32. (124 µm × 32 = 3.968 mm)
2. The ratio of the two bundles decides how white or blue the final light is. Since we want the light source to be mostly broadband light, the white LED must have the lion’s share the fibers.
3. Fibers stack readily into a hexagonal grid, and certain numbers of fibers stack better than others. 7 fibers pack nicely, and so the blue LED will have 7 fibers. The white LED has the rest. (32 – 7 = 25).

The 7 blue LED fibers were spread throughout the length of the slit. Although not entirely necessary, this was done so that the spectrum would remain homogenous along the length of the slit.

Each bundle was then epoxied into a connector and cleaved to an appropriate length. The ends were cleaved and polished. The fiber ends were inspected visually using a microscope as shown in Figure 3-4 (E) and (F). Upon inspection, a single broken fiber was observed in the white LED connector. the fracture likely occurred during the cleaving process. When the connector is coupled to the LED, however, none of the fibers are perceptibly darker upon visual inspection (of course, there is no convenient way of knowing the actual losses caused by the fractured fiber).

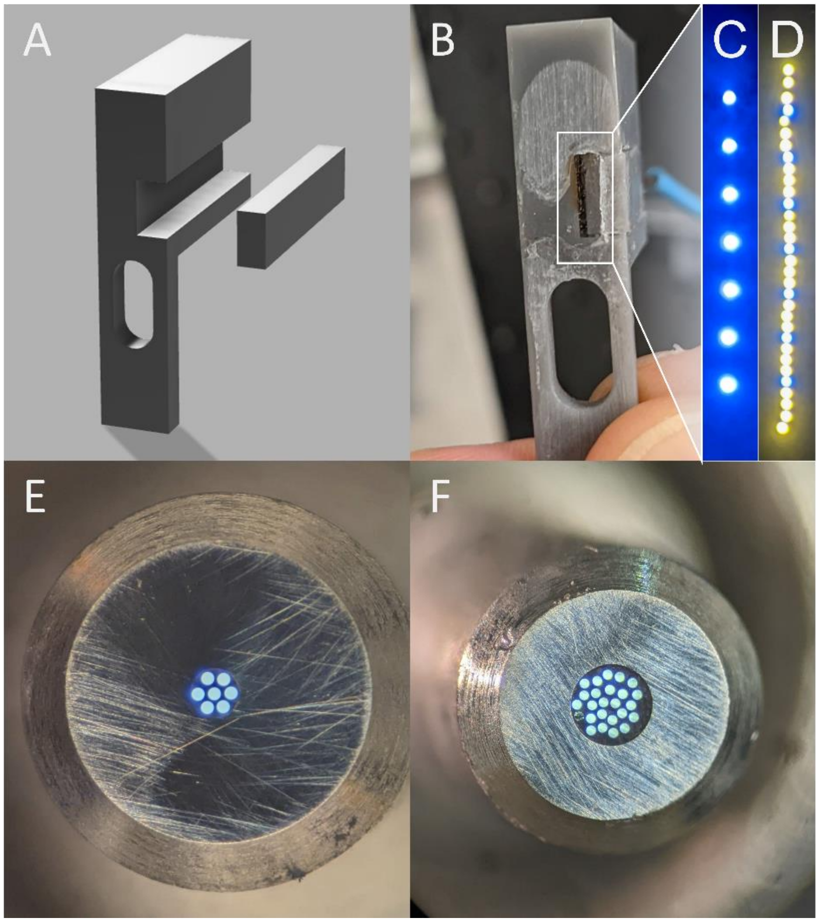

Figure 3-4 Combination Blue-White LED and Slit (A) 3D rendering of the slit mount and filler. (B) 3D printed mount with epoxied fiber slit. (C) Slit with only the blue LED on. (D) both white and blue LEDs on. (E) Polished fiber ends for the blue LED connector. (F) polished fiber ends for the white LED connector. A single fractured fiber is visible on the left of the bundle.

To prevent any damage to the LEDs, power from the standard power supplies is passed through fast-blowing fuses before reaching the LEDs. The blue and white LEDs were installed on the breadboard and connected to the slit, which was subsequently attached to the spectrograph via the set-screw. The entire LED and slit set-up can be seen in Figure 3-5.

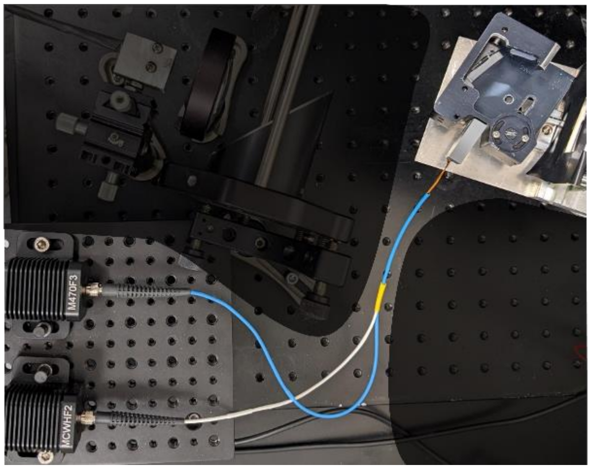

Figure 3-5 Image of the combination blue-white LED entrance slit setup. The fiber coupled LED units are seen in the bottom left, which connect to the 3D printed entrance slit and DMD spectrograph unit on the top right.

A comparison of the spectra with and without the blue LED are shown in Figure 3-6, and illustrate how the blue LED effectively fills the gap in the white LED’s spectrum. With the addition of the blue LED, the spectrum of the programmable light source is significantly more even across wavelengths. Since the LEDs are controlled by independent power supplies, the impact of the blue LED can be measured by turning the blue LED power supply off and recording the excitation spectrum. The light was recorded on an Avantes CCD spectrometer, by reflecting the excitation fibers from a white piece of paper and back into the emission fibers of the bifurcated probe (for more details on light source calibration, see Section 3.1.5).

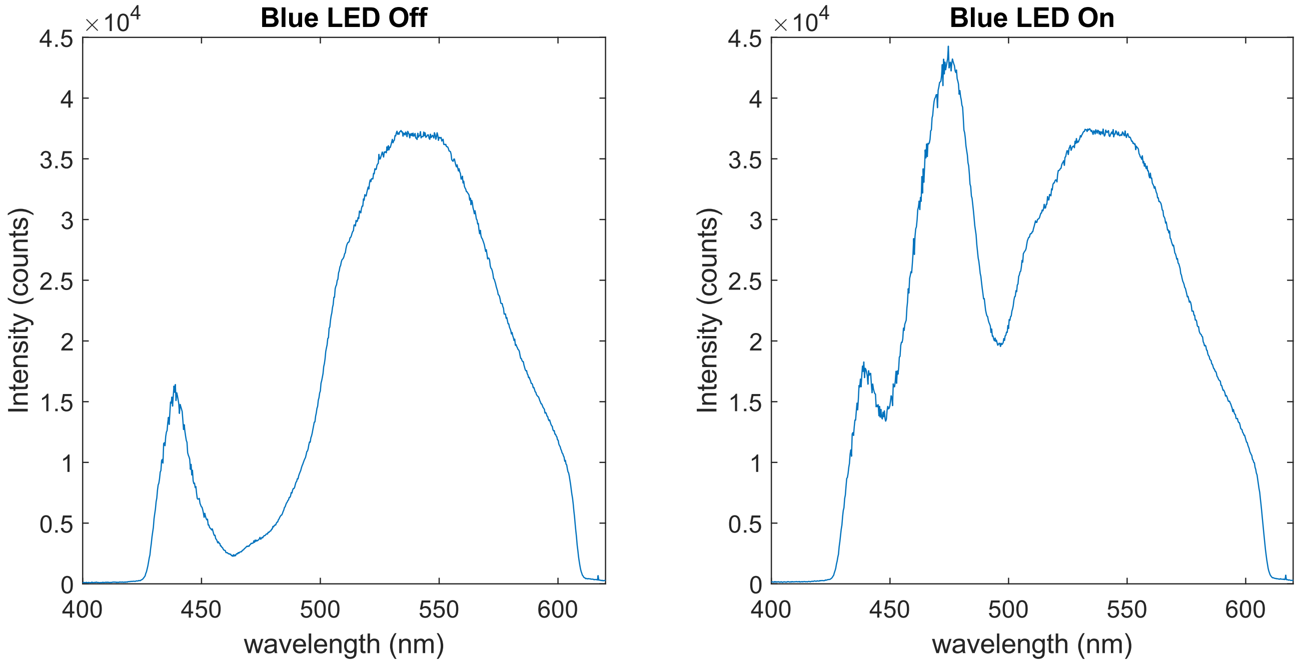

Figure 3-6 Spectrum excitation light source when the blue LED is off (left) and on (right).

3.1.2 Spectrograph

In order to project a spectrum of light onto the DMD, the white light must be diffracted into its component wavelengths. To do so, we have cannibalized the spectrograph from a spectrometer (Ocean Optics USB2000) and mounted it to a translation stage in front of the DMD. The spectrograph consists of a metal housing and a collimating mirror, a diffraction grating (600 lines/mm), and focusing mirror (focal length = 10 cm). the unit housing the linear diode array was removed so that fiber split could be attached. The dispersed light is projected onto the DMD, a diagram of which can be seen in Figure 3-7.

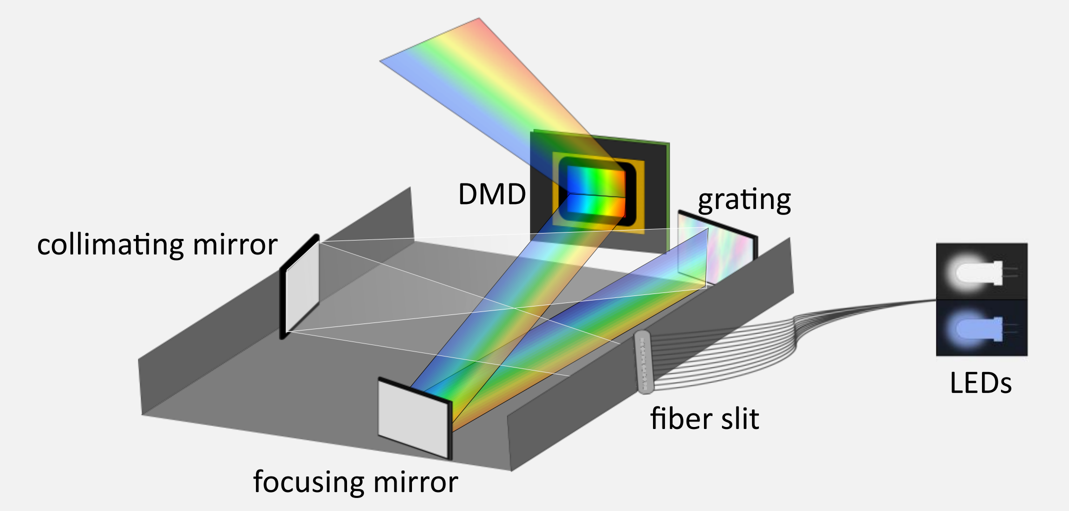

Figure 3-7 Diagram of Spectrograph.

By using a commercial spectrograph, much of the optical alignment has already been taken care of. That said, there have been some modifications to the spectrograph design. The stock focusing mirror (focal length = 4.5 cm) had been replaced with the longer focal length mirror (focal length = 10 cm) by past graduate student Adam Bernicky. The motivation for this modification was that the focal plane of the previous mirror was too short; the DMD could not reach the focal plane of the mirror the spectrograph housing was in the way. This resulted in unfocused light on the DMD. Since spectral resolution depends on how finely the light can be dispersed on the mirror, the unfocused light had caused the resolution to suffer. Using the longer focal length mirror, the DMD can be further away from the spectrograph while still remaining at the mirror's focal plane. The result is a greater spectral resolution[64] than with just the stock mirror.

3.1.3 Digital Micromirror Device

The digital micromirror device (DMD) is a microelectromechanical system developed by Texas Instruments.[65] It consists of an array of 768×1024 microscopic aluminum mirrors (10 μm x 10 μm) that each sit upon a hinge. By applying an electrostatic charge beneath a mirror, it is tilted either +12° or -12°, reflecting the light in either direction.[66] Since each mirror can be independently actuated, the array can be used to display an image, where every mirror on the array corresponds to a pixel in the image either “on” (+12°) or “off” (-12°). The “on” light can then be collected while the “off” light is discarded, shown in Figure 3-8.

Dispersed light is projected from the spectrograph onto the mirrors of the DMD, such that each column of mirrors corresponds to a different wavelength of light in the spectrum. Turning on a single column of mirror thus selects for a “single” wavelength of light. Multiple wavelengths can be turned on at a time to display a mask in the Hadamard Transform and multiplex the light.

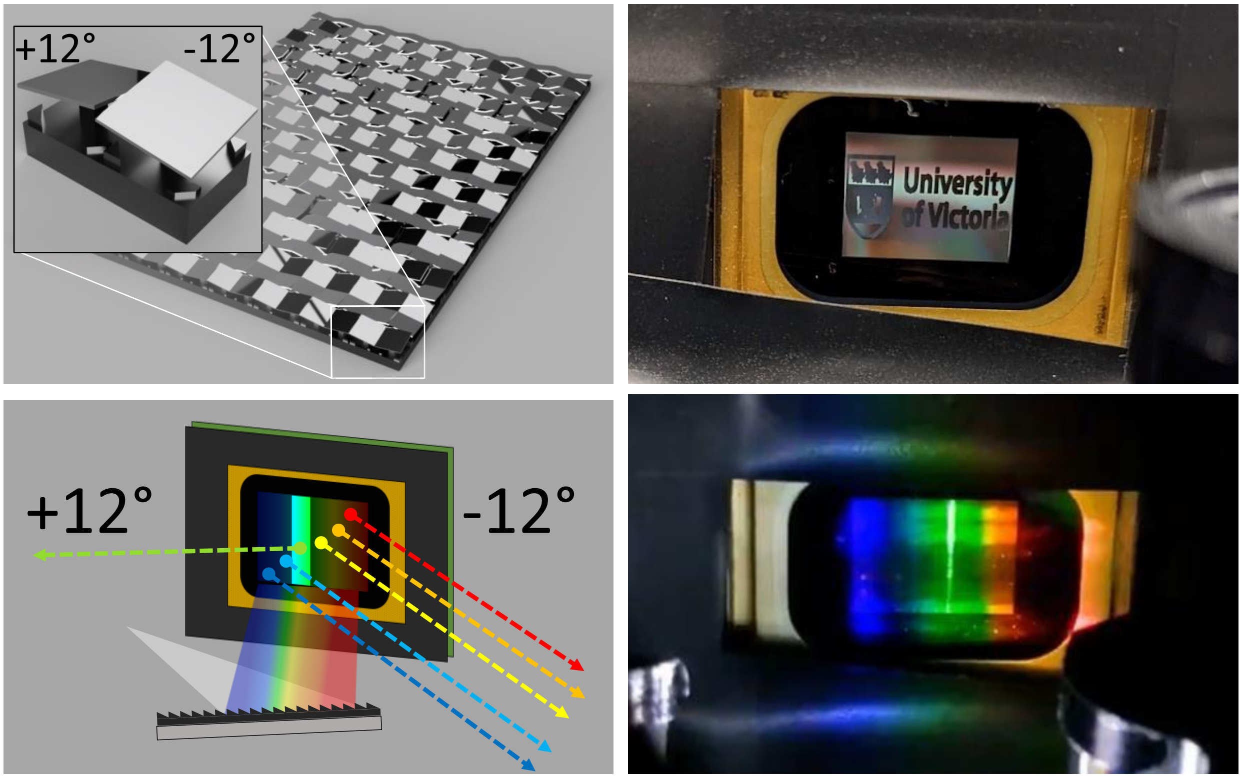

Figure 3-8 Digital Micromirror Device. (Top left) individual mirrors on the array tilting ±12° in an “on” or “off” position. (Top right) Image displayed on the DMD by turning some pixels on/off. (Bottom left) A schematic to illustrate how turning on/off mirror columns will select for unique wavelengths. (Bottom right) Image of a single column of mirrors selecting light on the DMD.

In practice, the spectral resolution of the programmable light-source depends, first, on the spectral resolution afforded by the dispersion element and the collimating optics, as well as how many mirror columns are grouped to constitute a spectral band (or “wavelength channel”). The 1024 columns of mirrors can be divided into *n* groups of columns, where *n* corresponds to the rows and columns in an $n \times n$ Hadamard S-matrix (e.g., 7, 31, 127 etc.). In the case where 1024 mirrors do not divide evenly into *n*, the remainder is left as unflipped mirrors in the blue region of the DMD array.

3.1.4 Collection Optics and Fiber Probe

The light reflected off the DMD at +12° was collected using a pair of off-axis parabolic mirrors. The first mirror collimates the diverging light, while the second mirror refocuses the collimated light. The light is then focused through a plano-convex cylindrical lens and into one of the arms of a custom-built bifurcated fiber probe, that carries the light to the sample. The fiber probe is the same as has been used in past iterations of this programmable light source.[64] It consists of 22 fibers that carry the excitation light from the DMD to the sample, and another 15 fibers that then carry the emitted light to a CCD spectrometer. While the HT Imaging system no longer uses the CCD spectrometer for detecting emission, the CCD spectrometer is still useful for calibration of the light source, and so the bifurcated probe is still coupled to the spectrometer.

3.1.5 Calibration of Light source

Once optical alignment has been completed, the light source needs to be calibrated. This consists of turning on a mirror column at a time, and measuring the spectrum on the CCD spectrometer, to inform what mirror column correspond to what wavelength of light. Single column measurements were taken for Hadamard S-matrices of size 7, 11, 19, 23, 31, 43, 59, 67, 71, 83, and 127 (541 images in total). Examples of these calibration spectra are shown in Figure 3-9 for size 7, 31, and 127 Hadamard S-matrices.

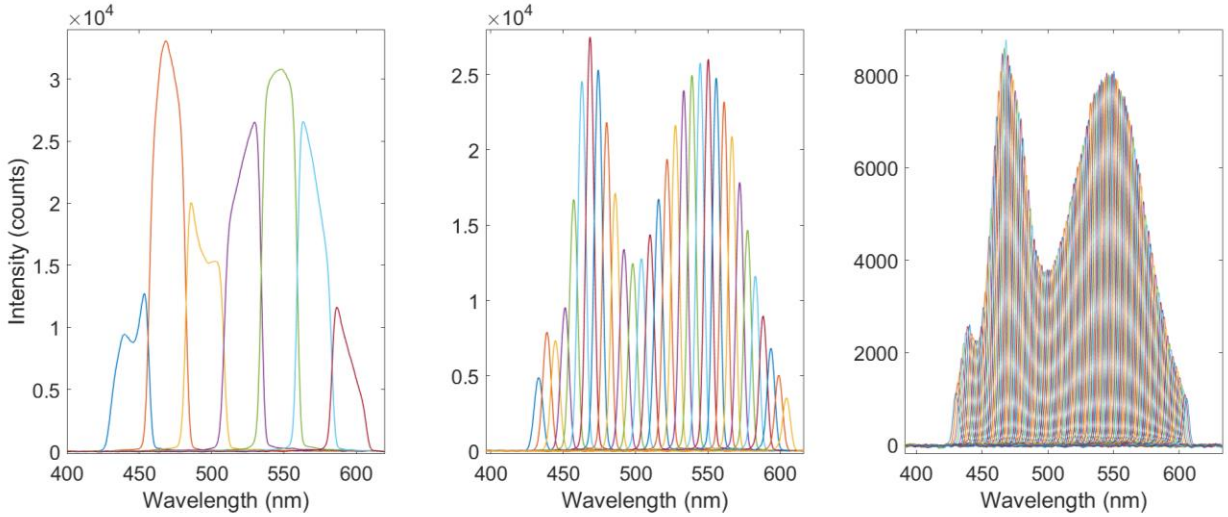

Figure 3-9 Calibration Spectra for size 7, 31, and 127 S-Matrices.

Each spectrum contains a single peak that corresponds to the wavelength reflected off that mirror column when it is flipped on. These peaks can be fitted to a Gaussian function using a MATLAB code written by Adam Bernicky, that can be found in Appendix A.i. The code fits each peak to a function

$$f(x) = a\,exp\left(-\frac{(x-b)^2}{2c^2}\right) \tag{16}$$

where *a* is the peak amplitude, *b* is the centroid and *c* is the peak width for each mirror column. These coefficients are useful for three main reasons. First the centroid informs which mirror corresponds to which wavelength, allowing us to assign wavelength information to the excitation axis of an EEM (e.g., not just “mirror column 1’, but rather 445 nm). Second, the amplitude allows a corrector to be applied, to scale the excitation spectrum appropriately for the intensity of the light source. If the corrector is applied, it boosts wavelengths where there may be a lower intensity vs. wavelengths with greater intensity. Third, the fit informs how finely the spectrograph light is dispersed across the DMD. The full-width at half-maximum (FWHM) of each peak can be determined from the formula,

$$FWHM = 2\sqrt{2\,ln(2)}\;c \tag{17}$$

where *c* is the peak width of the fitted Gaussian function as above. The spacing of each mirror column can be determined from the formula,

$$\Delta b = b_{i+1} - b_i \tag{18}$$

by computing the difference between neighbouring centroids, b_i and b_{i+1}. The average FWHM and mirror spacing can be found in Table 1.

Table 1 Average FWHM and mirror spacing for *n* mirror columns.

Number of masks	Average Full-Width-Half-Maximum (nm)	Standard deviation (nm)	Average mirror spacing (nm)	Standard deviation (nm)
7	20.89	1.98	24.22	2.62
11	13.53	0.74	15.86	1.74
19	8.57	0.38	9.14	0.62
23	7.50	0.33	7.59	0.42
31	6.34	0.29	5.70	0.28
43	5.51	0.27	4.00	0.23
59	5.15	0.27	2.95	0.83
67	5.06	0.27	2.60	0.17
71	5.00	0.26	2.44	0.17
83	4.94	0.26	2.09	0.16
127	4.80	0.26	1.39	0.15

By plotting the average FWHM as a function of the matrix size as shown in Figure 3-10, one can see how increasing the number mask increases spectral resolution, to a point. Eventually the resolution is limited to how finely the spectrum is dispersed across the mirrors, and any further increase in column numbers does not provide an increase in spectral resolution, and only increases the time required for a single EEM to be acquired. For the purposes of the experiments in this work, the matrix size of 31 was chosen, in order to balance speed of acquisition with spectral resolution.

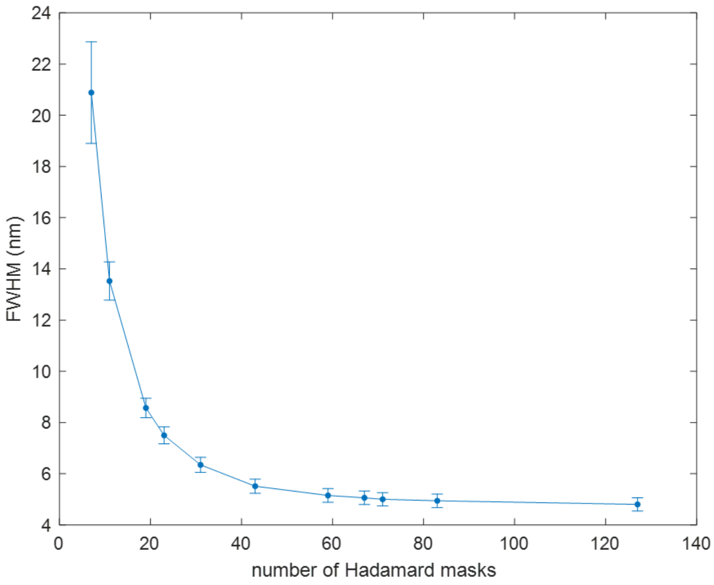

Figure 3-10 FWHM as a function of matrix size. Increasing the number of columns has diminishing returns on spectral resolution.

The Gaussian coefficients are saved on the computer as calibration files that can be accessed by the acquisition and image processing software, described further in Sections 3.3.1 and 3.3.2.

3.2 Hyperspectral Camera

The camera is an 8-channel visible wavelength hyperspectral camera (MSC-VIS8-1-A) supplied by Spectral Devices Inc. in London, Ontario. It consists of a standard complementary metal-oxide semiconductor (CMOS) sensor (CMV4000, Austria Mikro Systeme) with a 4 MP resolution (2048×2048 pixels). Each pixel is 5.5×5.5 μm in size. The camera can be seen in Figure 3-11.

Figure 3-11 Photo of 8-channel visible hyperspectral camera (msCam VIS8, Spectral Devices Inc).

3.2.1 Spectrally Resolving Detector Array

Spectral Devices Inc. builds a hyperspectral camera from a commercially available CMOS sensor and a proprietary filter array which is attached to the monochrome sensor. The filter array consists of 8 different filters that block all wavelengths except for respective narrow spectral bands that are transmitted by the filters to irradiate the underlying light-sensitive CMOS photodetector pixel. The filter array is applied in a mosaic, such that a tile is repeated every 8 pixels along the 2048×2048 array, giving a 256×256 array of filtered pixels.

The eight filters in each tile are arranged in four rows by two columns. A single filter spans the height of one pixel (5.5μm) and the width of three pixels (16.5 μm), with a single border pixel in between neighbouring filters. These bordering pixels are used to prevent crosstalk between neighbouring pixels and are ultimately discarded when the image is demosaiced. Figure 3-12 illustrates the filter array and the arrangement of the individual filters on the detector.

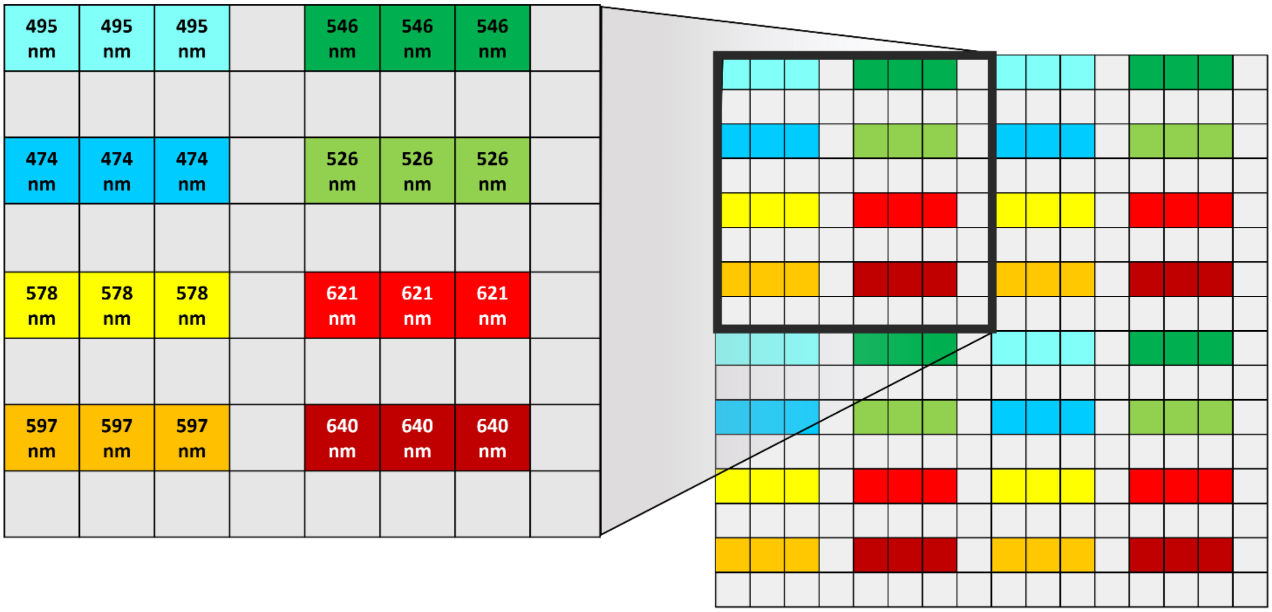

Figure 3-12 Spectrally resolving detector array. The camera consists of a 2048 x 2048 CMOS sensor overlaid with an 8 channel filter array (474-640 nm). Bordering pixels prevent crosstalk from neighbouring filtered pixels. Each pixel (inset left) consists of an array of 8 x 8 subpixels, Only 24 of the 64 subpixels are collecting light that forms an image in 8 different pass bands.

Henceforth, each tile (which consists of one set of the eight filters) may be referred to as a pixel, such that one hyperspectral image consists of 256×256×8 values, whereas the physical pixels on the monochrome CMOS sensor may be referred to as a subpixel, one pixel consists of an 8×8 grid of subpixels.

3.2.2 Camera Lens and Attachments

The camera can attach to a lens via a C-mount, which allows for a degree of flexibility in the selection of appropriate optics for the given application. In this body of work, all images and data collected were captured with a 50 mm fixed focal length lens (V5024-MPZ, Computar) with a close-up +2 diopter lens (Heliopan) on the front threading of the main lens.

3.2.3 Hyperspectral Image Processing

There are two treatments applied to the raw images before they can be used as a hyperspectral image. The first step is averaging the three subpixels that make up a single filtered pixel. The second important step is called Bayer-demosaicing or just demosaicing. The term refers to the mosaic of filter arrays found on colour cameras – in commercial RGB cameras, they are referred to as Bayer filters after the inventor Bryce Bayer.[61] In the case of hyperspectral imaging, it refers to the algorithm that selects for the subpixels in the raw image that correspond to each pixel in each wavelength channel. After demosaicing, the image can be arranged as a three-dimensional data cube with dimensions 256×256×8. To better aide the visualization of the hyperspectral image, it is convenient to rearrange the 8 channels in a single image that is 512 pixels tall and 1024 pixels wide. This is done using a MATLAB function I wrote called demosaicv6, and can be found in Appendix A.ii.

To demonstrate the ability of the filtered array to discern different wavelengths of light, an assortment of different coloured materials (e.g. a green sign, red box, orange webbing, blue spatula holder) were placed in the frame of the image. A demosaiced hyperspectral image can be seen in Figure 3-13.

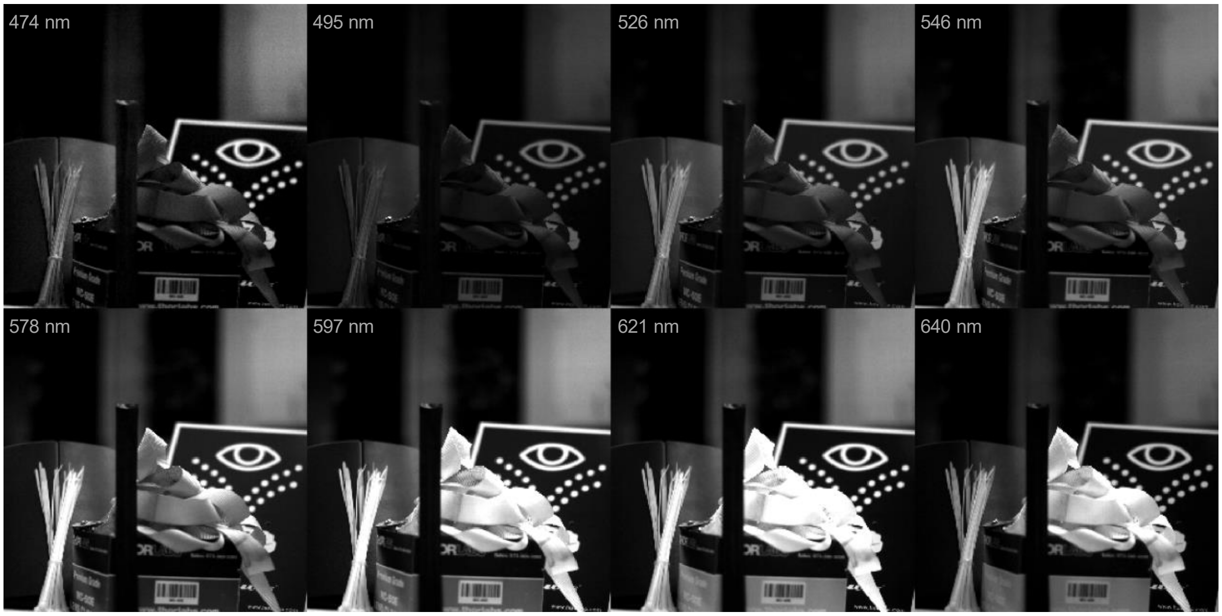

Figure 3-13 Demosaiced Hyperspectral Image of assorted materials in the lab. each tile shows all the pixels for the filter channel indicated.

Since a typical RGB camera only uses three channels, RGB images can be approximated or “false-coloured” from the 8-channel hyperspectral image, by selecting three channels to represent red, green, and blue. For example, if 640 nm, 526 nm, and 474 nm channels are chosen for RGB respectively, then the hyperspectral image in Figure 3-13 can be viewed as a false coloured RGB image in Figure 3-14, compared to a RGB image from a conventional cell phone (Google Pixel).

Figure 3-14 False-coloured RGB Image vs Cell Phone Image. RGB image (left) generated from the hyperspectral image in Figure 3-13. The red, green, and blue values are assigned from the intensities of the 640 nm, 526 nm, and 474 nm hyperspectral channels, respectively. Cell phone image of the same assorted materials (right).

These false colour images are not used for any data analysis within this thesis, however they can be useful in a pedagogical application to demonstrate what a hyperspectral image “looks like”.

3.2.4 Characterization of Spatial and Spectral Resolution

The spatial resolution of the hyperspectral camera can be limited by both, optical resolving power which leads to blurring of an image, and by pixelation. We expect that pixelation is a concern since the sensor array has been divided into 8 channels, and the resolution was thereby reduced from a 2048 x 2048 pixels sensor (4 MP) to a 256×256 pixel sensor (0.065 MP). To measure the spatial resolution, the camera was equipped with a 50 mm fixed focal length lens and +2 diopter close-up lens (Section 3.2.2,) and a ruler was placed at the minimum focal distance for the 50 mm lens. The demosaiced hyperspectral image can be seen in Figure 3-15. It is apparent that blurring is not a concern but rather that pixelation limits the spatial resolution. There are 10 pixels between millimeter markings on the ruler, which is visible if one zooms in on the markings as seen in Figure 3-16. We can conclude that with these optics, a maximum resolution of 10 pixels/mm is achievable and that the spatial resolution is about 100 μm.

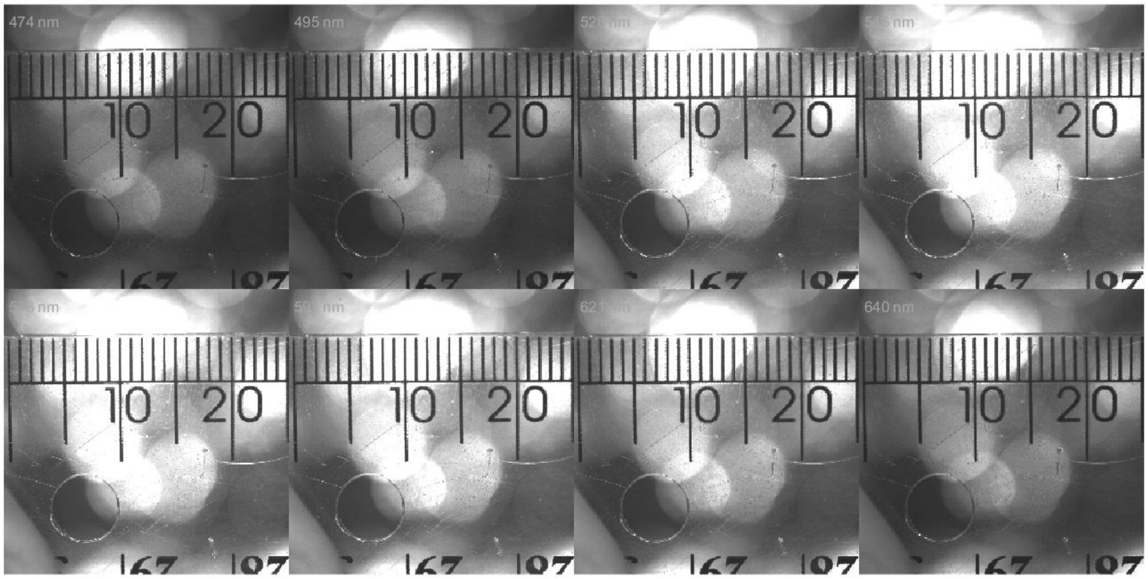

Figure 3-15 Hyperspectral image of a ruler delimited in millimetres.

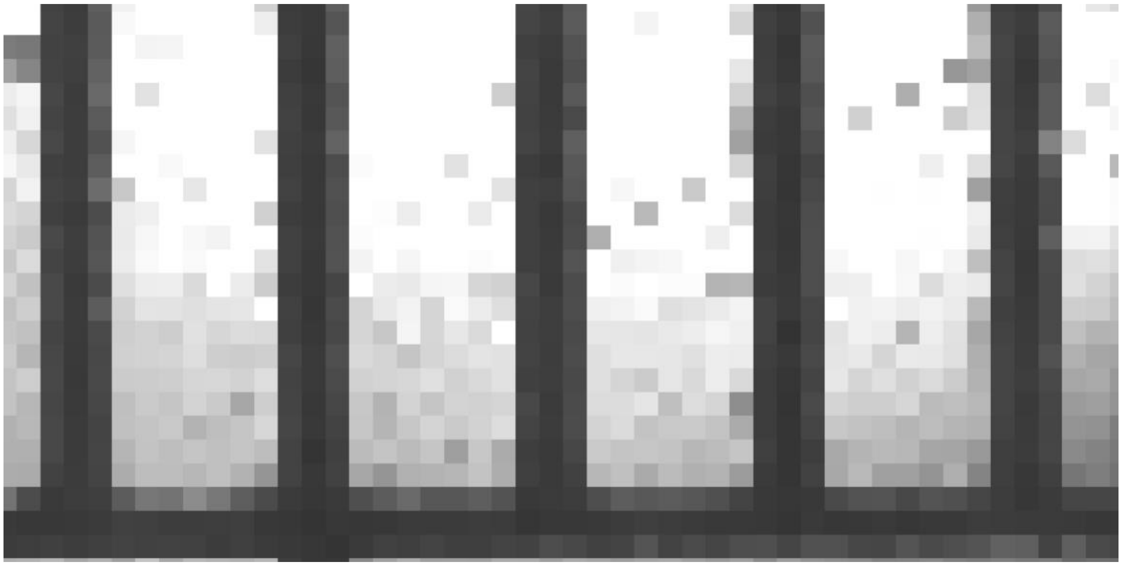

Figure 3-16 Zoom-In of a Hyperspectral Image of a Ruler. There are 10 pixels per millimetre.

To characterize the spectral response of each of the 8 filters, the camera was placed inside a conventional excitation emission fluorescence spectrometer (Varian Cary Eclipse) and pointed at the excitation slit. Then, 195 hyperspectral images were captured with excitation light from 460 nm to 650 nm in 1 nm steps, i.e. the commercial spectrometer was used as a tunable light source. The wavelength range was chosen because the camera's filters range from 474 nm to 640 nm. Each image was then demosaiced into eight channels, and all the pixels across a single channel were averaged to a single value, i.e. any and all spatial information was discarded and the camera was treated as a simple eight channel spectrometer. The spectral response of these eight channels was graphed as a function of the excitation wavelength, seen in Figure 3-17.

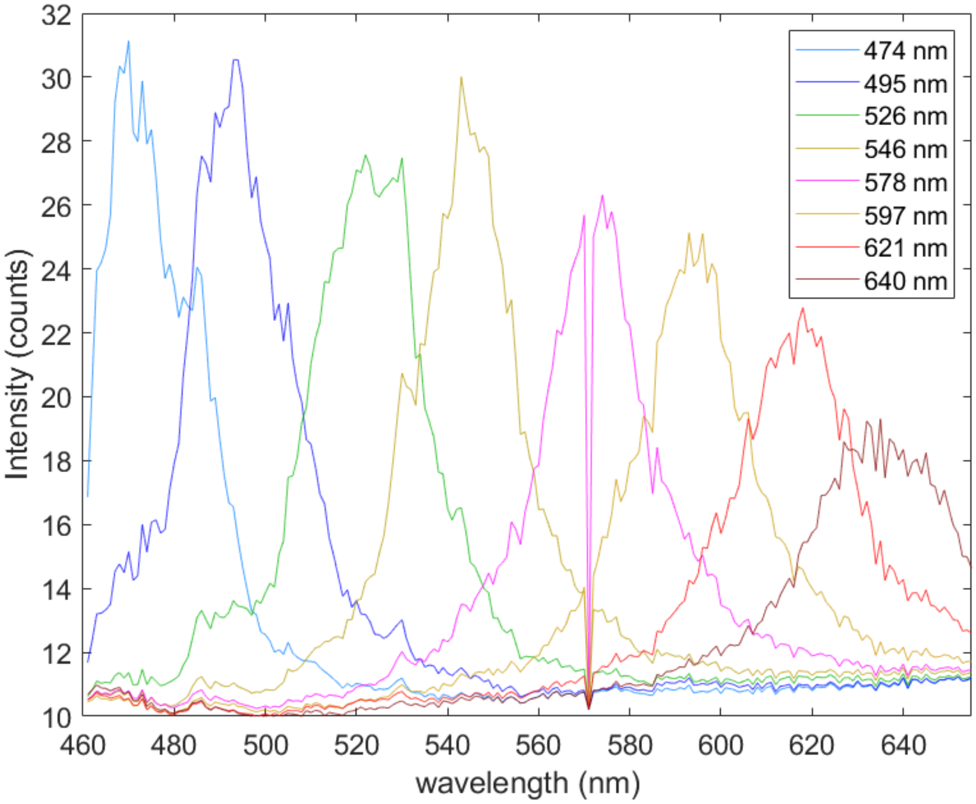

Figure 3-17 Spectral response of the camera filters. A change in spectrometer filters is observed at 570 nm.

While the design of the filters is proprietary to the manufacturer, we expect Lorentzian line shapes for filters based on dichroic stacks. Each curve was fitted to a Lorentzian function using the least squares method, packaged in a MATLAB function by Jered Wells[67] called lorentzfit. The Lorentzian function can be described by the formula

$$L(x) = \frac{P_1}{(x-P_2)^2+P_3}+C \tag{19}$$

Where P_1, P_2, P_3, and C are parameters fitted to the Lorentzian function $L(x)$, and outputted by the MATLAB code. P_2 is the resonance about the Lorentzian, and so it is the wavelength at the maximum. To find the maximum of the Lorentzian, x is set equal to P_2 to give

$$\begin{gathered} A' = \frac{P_1}{P_3}+C \\ A = \frac{P_1}{P_3} \end{gathered} \tag{20}$$

Where A' is the maximum of the function, and A would be the amplitude from the base of the peak). The FWHM can thus be found by setting the function equal to $A/2$ and solving for x. Note that the constant is not included, so that the maximum is defined from the baseline. P_1/P_3 can then be substituted in for A to give the solution for the x values at the half maximum.

$$\begin{gathered} \frac{A}{2} = \frac{P_1}{(x-P_2)^2+P_3} \\ x = \pm\sqrt{2\frac{P_1}{A}-P_3}+P_2 \\ x = \pm\sqrt{P_3}+P_2 \end{gathered} \tag{21}$$

The FWHM is thus equal to the difference in the + and – terms.

$$\begin{gathered} \text{FWHM} = \left(\sqrt{P_3}+P_2\right)-\left(P_2-\sqrt{P_3}\right) \\ \text{FWHM} = 2\sqrt{P_3} \end{gathered} \tag{22}$$

The fitted functions for the filter responses can be seen in Figure 3-18. The wavelengths at resonance and the calculated FWHM can be found in Table 2. The reported wavelength channels are in good agreement with the measured spectral response, with a mean discrepancy of just 3.02 nm, and a maximum discrepancy of 4.94 nm in the 578 nm channel.

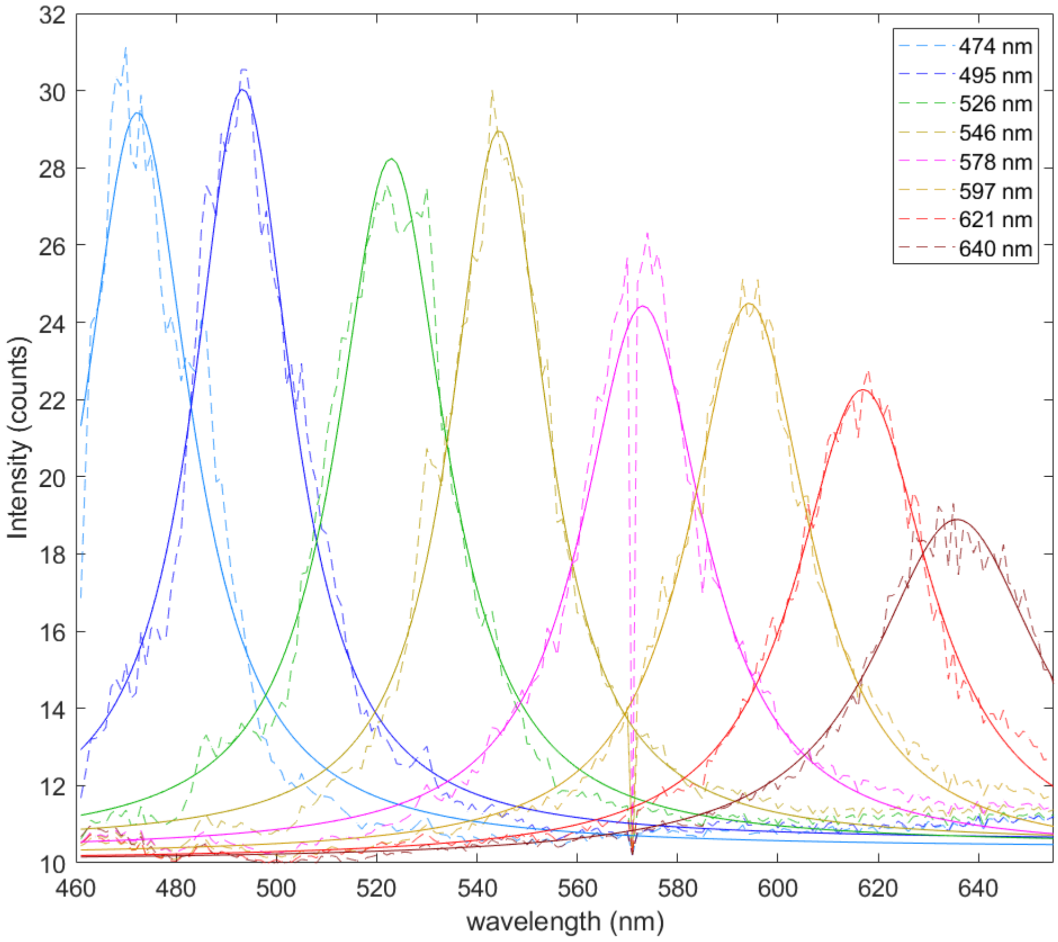

Figure 3-18 Spectral response of the camera filters fitted to Lorentzian functions. The Lorentzian curves (solid lines) are overlaid on the original filter response curves (dotted lines).

Table 2 Calculated resonant wavelength and FWHM from Fitted Lorentzian Functions. The mean discrepancy is just 3.02 nm, with a maximum of 4.94 nm in the 578 nm channel.

Reported wavelength (nm)	Wavelength at Resonance (nm)	Discrepancy (nm)	Full-Width at Half-Maximum (nm)
474	472.29	1.71	26.19
495	493.27	1.73	24.02
526	522.88	3.12	26.44
546	544.41	1.59	23.47
578	573.05	4.94	29.83
597	594.27	2.73	29.20
621	616.96	4.04	32.85
640	635.74	4.26	40.91

3.3 Software

As mentioned previously, the spectrometer is made by combining two major components: the programmable light source, and the hyperspectral camera. A major focus of this work was on controlling these two technologies and combining them into a single system. Each device came with its own application programming interface (API) which could then be controlled using MATLAB. I wrote two main MATLAB programs: the first program to control the settings of the devices and operate the camera and light source in concert for the acquisition of spectra, and a second program to demosaic each hyperspectral image and then demodulate each Hadamard encoded spectrum into an EEM. For ease of use, I packaged these two programs into two graphical user interfaces (GUI). The programs and GUIs will be discussed below.

3.3.1 5D Image Acquisition Software

The acquisition software consists of two workflows: the first workflow takes place before the acquisition to allow the user to make changes to the camera settings and physical scene; the second workflow operates the DMD and acquires the hyperspectral images simultaneously. These workflows can be seen in Figure 3-19 and will be described in detail below.

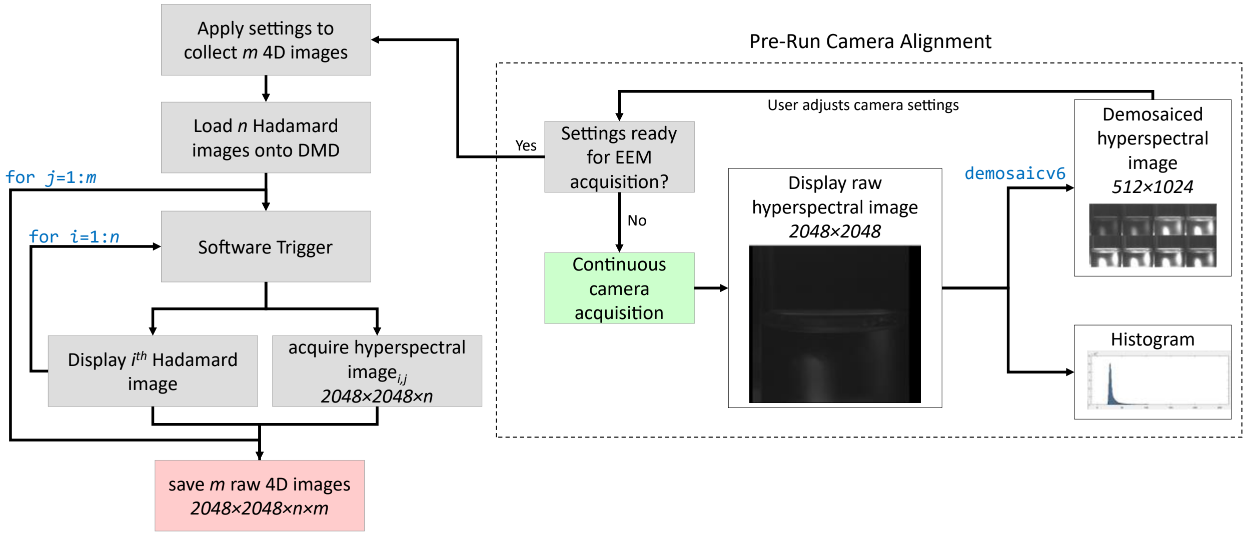

Figure 3-19 Flowchart for 5D Image Acquisition Software. The workflow in the dotted box occurs live before a run, to allow the user to control camera settings. Blue text indicates MATLAB for-loops, or functions found in the appendix. Here, j is a given frame of video in time, *m* is the number of total frames, *i* is a given mask in the Hadamard sequence, and *n* is the size of the Hadamard S-matrix used (and thus number of total excitation wavelengths).

Upon opening the GUI, the camera is automatically connected and continuously acquires raw images that are displayed in the GUI. These raw images are then passed to two functions and displayed on the GUI:

1. demosaicv6, which as described in Section 3.2.3 displays a tiled hyperspectral image of all eight camera channels.
2. A histogram plotting function, which shows the number of pixels as a function of their 8-bit intensity (0 to 255).

In this pre-run alignment phase, the user has a chance to change the integration time, black level, and gain to obtain an optimal image. The demosaiced image and histogram help the user find ideal settings that maximize dynamic range and thereby produce the images with the largest intensity resolution. Each time the black level, gain, or integration time is changed, the demosaiced image and histogram are refreshed. The user can also use a “Grab HSI" button that conveniently plots the demosaiced image in another figure, complete with labels for each wavelength channel. This feature was used to generate many of the tiled demosaiced images found in this thesis.

To simulate the lighting conditions during the experiment, the user has the option to turn “on” all the DMD mirrors such that the sample object is irradiated by all wavelengths transmitted through the fiber probe. This is achieved by loading a single mask onto the DMD memory, which contains a 768×1024 array of 1s. The image is held on the DMD mirror array until the user turns it “off”.

There is also an option to have the demosaiced image and histogram “live” update. To do so, a listener is created, which listens for the camera’s FrameAcquired event. Upon a frame acquisition, the listener then runs the histogram and demosaicv6 functions to update the plots. This can be useful especially when the user is adjusting the physical scene settings to ensure any subjects are in focus and within the field of view of the camera. There is a noticeable lag in the feed when the live update is engaged because MATLAB is by nature single-threaded. Prior to any EEM acquisition the live update was therefore automatically disengaged.

Once the integration time, black level, and gain has been set, the user is ready to acquire a 4D image or 5D image sequence. First, the DMD is connected to the program and the user specifies the file location to save the 4D/5D image, as well as the location of any calibration files that have been acquired prior to this. For an in-depth explanation on the calibration process, see Section 3.1.5. To see how the calibration files are used in the processing of the 4D/5D images, see Section 3.3.2.

The user also specifies the file location for the chosen image sequence (e.g. Hadamard S-matrix, Sequential scan sequence, etc.). The image sequence is loaded onto the DMD’s memory, along with one additional image that constitutes a background measurement with all mirrors flipped to “off” (e.g. for a 31-sized S-matrix, 32 images are loaded on the DMD).

The illumination time is then set for the DMD. The illumination is determined from the integration time set for the hyperspectral camera and refers to the amount of time the DMD mirrors will remain flipped on or off in their flipped state for a given image before they switch to the next image. First the time required to flip the mirrors (44 µs) must be taken into account. To ensure the scene is properly illuminated for duration of the camera’s exposure, the DMD illumination time is set for an additional 100 μs. Thus, the illumination time is set to be 0.144 ms longer than the integration time. In practice, the data acquisition rate is limited by the much larger integration time (500 ms or longer) and – for the brightest images - by the image transfer time from the camera to the computer’s memory (20 ms).

The user can choose to either capture a single 4D image or specify a number of scans to capture a 5D image. Once either case is initiated by the user, the program applies a few last-minute settings to prepare the camera for a speedy acquisition and decrease any lag due to other MATLAB functions running in the background. The GUI feed display is turned off, the camera acquisition mode is set from “continuous” to “single frame”, and the camera trigger mode set to “active”. This instructs the camera to wait for a trigger signal from the software, and upon receipt acquire a single frame. Once these final settings are applied, the software triggers the DMD to flip its mirrors to the first image, and then the camera is triggered to acquire a frame. Once the frame has been received by the computer’s memory, the next DMD image in the sequence is acquired, and so on. Once all DMD images have been displayed, the program either repeats the process for the next 5D image, or (in the case of a single 4D image) proceeds to saving the file. Along with the image dataset, the program saves a .mat file which contains all the settings/metadata for the camera and DMD including integration time, black level, gain, timestamps (if 5D), and the location of the blank/calibration file used for this run. This metadata is passed to the image processing software and is integral to the processing workflow. Finally, once all files are saved, the “continuous acquisition” and live update are restored. The GUI can be seen in Figure 3-20.

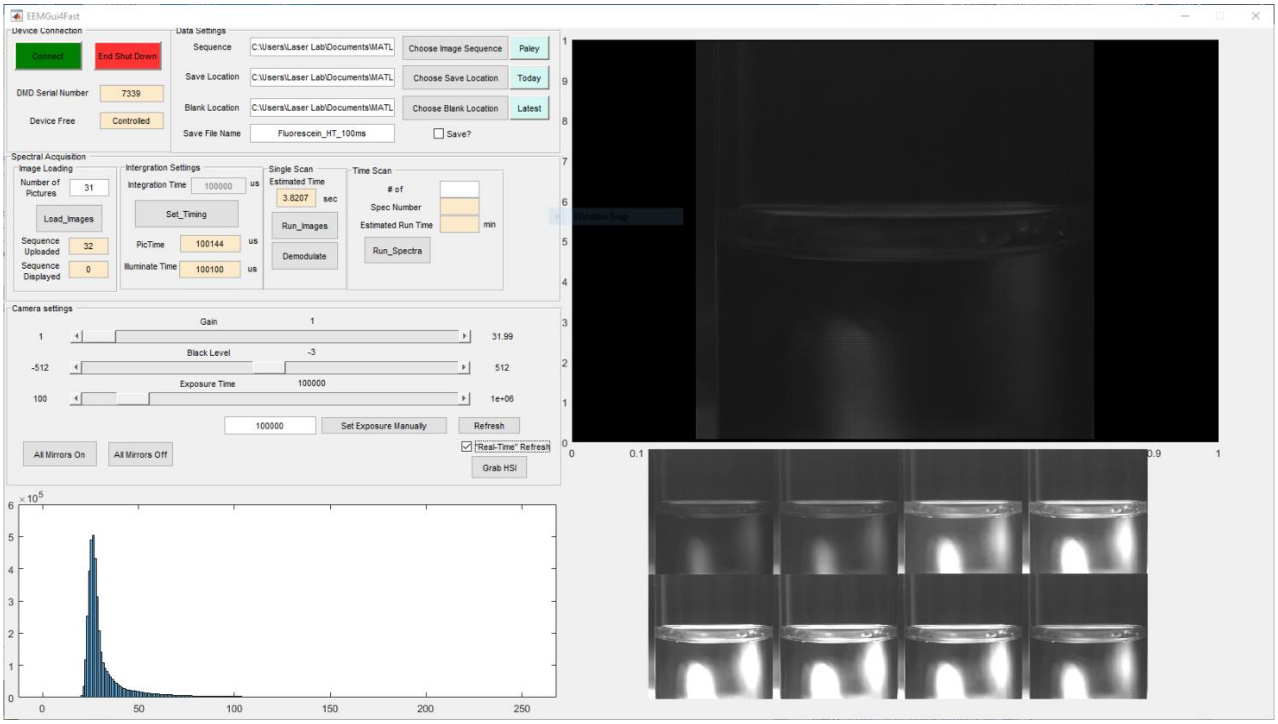

DMD Serial Number: 7339
Device Free: Controlled
Sequence: C:\Users\Laser Lab\Documents\MATL
Save Location: C:\Users\Laser Lab\Documents\MATL
Blank Location: C:\Users\Laser Lab\Documents\MATL
Save File Name: Fluorescein_HT_100ms
☐ Save?
Number of Pictures: 31
Sequence Uploaded: 32
Sequence Displayed: 0
Integration Time: 100000 us
PicTime: 100144 us
Illuminate Time: 100100 us
Estimated Time: 3.8207 sec
# of Spec Number:
Estimated Run Time: min
Gain: 1
Black Level: -3
Exposure Time: 100000
100000
☑ "Real-Time" Refresh

Figure 3-20 GUI for 5D image acquisition software.

3.3.2 Image Processing Software

The image processing software consists of two workflows: the first workflow processes the raw images into a single 5-dimensional dataset, and the second workflow allows the user to interact with the dataset, apply post-processing effects, and inspect different features in the spatial and spectral domains. These workflows can be seen in Figure 3-21.

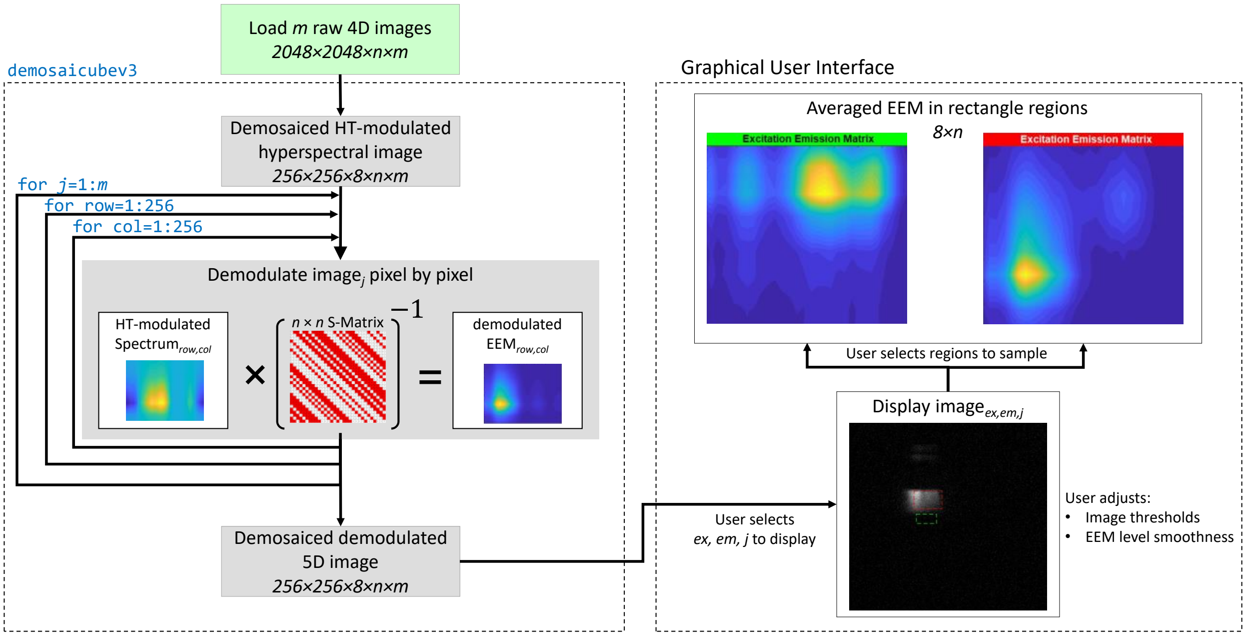

Figure 3-21 Flowchart for Image Processing Software. Blue text indicates MATLAB for-loops, or functions found in the appendix. *j* is a given frame of video in time, *m* is the number of total frames, *row*/*col* are a given row and column in an image, *n* is the size of the Hadamard S-matrix used (and thus number of total excitation wavelengths), and *em*/*ex* are a given emission and excitation wavelength.

The workflow of processing raw images into 5D datasets is operated by passing the raw images into the function demosaicubev3, which can be found in appendix A.iii. The demosaicubev3 function is essentially a hybrid of two operations described so far, demosaicv6 and a Hadamard demodulation. Much like demosaicv6, demosaicubev3 take in a raw hyperspectral image and demosaics the image into the eight wavelength channels. Unlike demosaicv6, which organizes the eight 256×256-images in a 2D tile arrangement of 512×1024, demosaicubev3 organizes the demosaiced hyperspectral images into a 3D data cube of 256×256×8. The dataset is easier to index with the added dimensionality.

The data set now consists of a single 256×256×8×n image, where n is the number of Hadamard encoded images captured. Thus, each pixel of size 8×n can be thought of as an encoded EEM. The demosaicubev3 function then demodulates each pixel in the image by multiplying it by the inverse n×n Hadamard S-matrix, to yield one 8×n EEM per pixel in the image. This process of demosaic-demodulation is repeated *m* times, where *m* is the number of frames captured in time. The output is a demosaiced demodulated 5D image of size $256 \times 256 \times 8 \times n \times m$, and dimensions *x*, *y*, emission, excitation, time.

This dataset is then displayed in the GUI, shown in Figure 3-22 below. Slider bars allow the user to slide through the excitation and emission wavelengths shown in the 256×256-image on screen. A slider bar for the frame dimension is available so that the user can also slide forward or backward through time. The user can click any two points in the image to define a rectangular region and sample the EEM in those defined pixels. This draws a red or green rectangle on the image, and then displays the averaged EEM on the corresponding red or green axes. When the two region's EEM are viewed simultaneously, the contour plot height (or intensity) is by default normalized for each plot independent of one another. By checking the box labeled "compare EEM Heights", the user can scale the contours to the absolute maximum and minimum of the defined two regions.

The GUI offers convenient methods to output the current image and EEMs as a figure, along with options for post-processing effects. There is a slider bar which allows the user to increase or decrease the smoothness of the contour plots. There is also the option to change the image threshold values for the minimum and maximum bright pixel. These are set to 0 and 1 by default, but if the user were to set the maximum to instead 0.6, then all pixels with a value of 0.6 and greater would be set to the maximum brightness. This boosts any darker signals and can be helpful when images have low SNR.

After the user has visually inspected the dataset, the GUI offers options to output the dataset in forms readable by the PARAFAC algorithm. The user can choose to crop out any Rayleigh scattering, which is commonly done to prevent interference with the PARAFAC model.[68] The user can also crop the image spatially by defining some rectangular region of interest. This reduces the size of the dataset and can decrease the time needed to fit the model. The spatial crop also increases the percent of the dataset explained of the model if most of the pixels outside that region are dark.

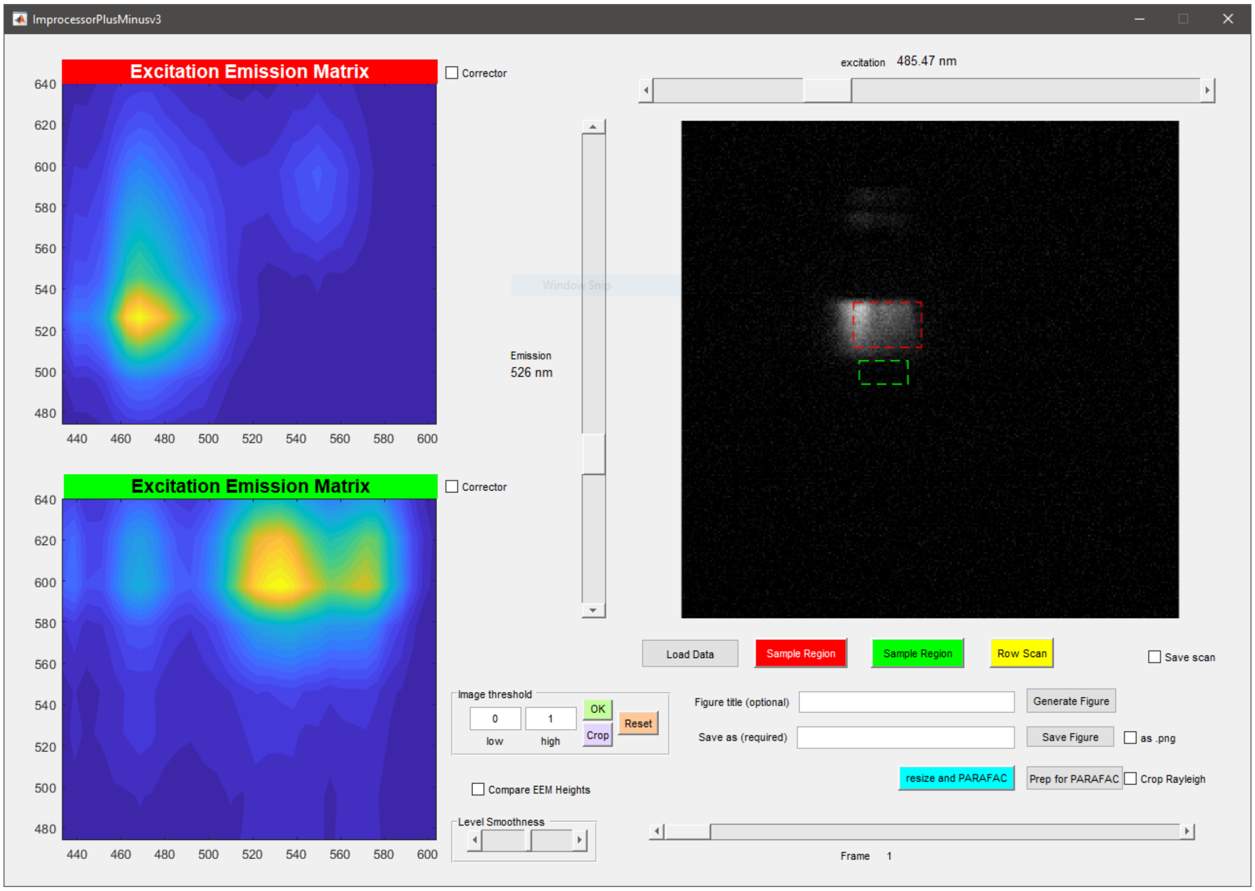

excitation 485.47 nm

Emission 526 nm

Image threshold: low 0, high 1

Frame 1

Figure 3-22 GUI for 4D and 5D image processing.

3.4 Comparison of Sequential Scan vs. Hadamard Transform

As mentioned in Section 2.3, the Hadamard transform is a multiplexing technique, and so it is afforded Fellgett's advantage[36] yielding increased signal when compared to a non-multiplexing sequentially scanned technique. To demonstrate the improvement of HT over a sequential scan, these two methods were used to collect a 4D image of a vial of fluorescein and the level of the fluorescence signal was compared to the noise of the signal. Both the sequential scan and the HT measurements were performed on the imaging system, as opposed to some other device such as the Varian Cary Eclipse, to avoid conflation of the results due to differences in equipment, alignment, or device sensitivity. The scans were performed on the same day with no changes to either the camera's settings, optics and focus, or the subject in the image. The Hadamard transform used a size 31 Hadamard S-matrix, while the sequential scan had the same 31 mirror columns, turned on individually. The experiment was repeated in both methods with integration times of 20, 50 and 100 ms, and results are given in Figure 3-23 below.

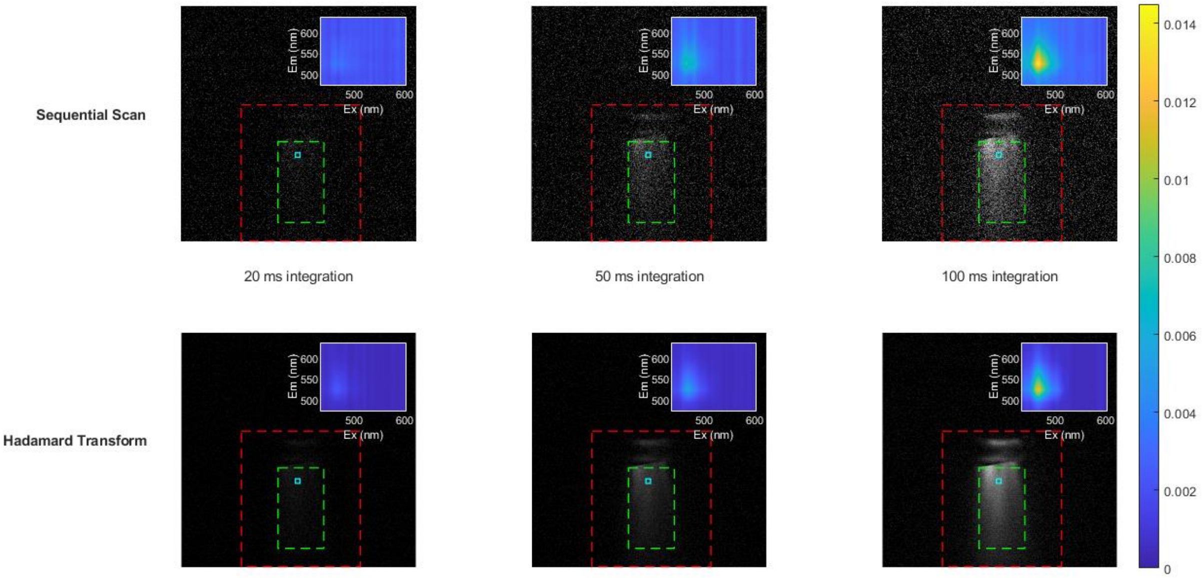

Figure 3-23 Hadamard transform vs. Sequential Scan. Images of a vial of fluorescein at *ex/em* = 468 nm/526 nm and increasing integration times (inset) averaged EEM spectra from the green rectangular region. Pixels outside of the red region are defined as background. Pixels within inner cyan region are sampled for the SNR calculation.

The signal-to-background ratio (SBR) is defined the formula,

$$\mathrm{SBR} = \frac{\bar{S}_{468/526} - \overline{BG}}{\overline{BG}} \tag{23}$$

Where $\overline{S}$ is the signal mean at fluorescein's maximum excitation and emission wavelength (468 nm and 526 nm), and $\overline{BG}$ is the mean of the background at all excitation and emission wavelength. The signal is sampled spatially within the region enclosed by the green rectangle, and the background is sampled outside of the red region. The SBR can then be calculated for both HT and sequential scan methods at each integration time. The signal-to-background enhancement (SBE) can be calculated by dividing the

HT SBR by the sequentially-scanned SBR. The SBR and SBE can be found in Table 3. The Hadamard transform has an average SBE of around 3.5.

Table 3 Signal to Background Enhancement of Hadamard Transform vs. Sequential Scan.

	20 ms	50 ms	100 ms
Hadamard Transform SBR	4.99	9.54	16.60
Sequentially Scanned SBR	1.36	2.85	4.85
Signal to Background Enhancement	3.66	3.34	3.42

The table also shows that, both, signal and background levels increase differently with the integration time. This is evident in an offset of a linear regression of the SBR values against integration time (not shown). If the signal and background measurements had the same dependence on the integration time, the SBR values would have been the same for all three integration times. We can therefore exclude background light intensity as the sole source of the background signal, as it would have increased identically to the fluorescence signal. In our attempt to identify the source of the background we turn to the signal-to-noise ratios.

The signal-to-noise ratio (SNR) of the signal can be determined as it is defined in image processing,[69, 70] otherwise known as the reciprocal coefficient of variation. The formula for SNR is

$$\mathrm{SNR} = \frac{\mu}{\sigma} \tag{24}$$

Where μ is the mean pixel intensity value, and σ is the standard deviation of the pixel intensity in a region of interest (ROI) where the signal is expected to be uniform. Here, the ROI is defined by the small cyan box in Figure 3-23, at the wavelength maximum at 468 nm and 526 nm. SNR is determined for both HT and sequentially scanned images. The signal-to-noise enhancement (SNE) can be found by taking the ratio of HT SNR to sequentially-scanned SNR. The SNR and SNE can be found in Table 4, with an average SNE of 3.37 across the integration times.

Table 4 Signal-to-Noise Enhancement of Hadamard Transform vs. Sequential Scan.

	20 ms	**50 ms**	**100 ms**
Hadamard Transform SNR	3.65	7.08	13.25
Sequentially Scanned SNR	1.13	2.54	3.23
Signal-to-Noise Enhancement	3.23	2.79	4.10

The experimental SNE can be compared to a calculated theoretical SNE, if one assumes all noise is random additive noise from the detector, as described by Nitzsche and Riesenberg.[71] In the case of detector noise, the measured signals m_j for the j^{th} multiplexed measurement are

$$m_j = \sum_i H_{ji} \cdot x_i + e_j \tag{25}$$

Where H is the Hadamard matrix and x_i is the original fluorescence signal for the i^{th} wavelength, and e_j are the random errors for each measurement added after multiplexing. The signal is then demodulated and reconstructed as r_i, which differs from the original signal x_i by an error of ε_i, related to the multiplexing error e_j by

$$\varepsilon_i = (r_i - x_i) = \sum_j H_{ij}^{-1} \cdot e_j \tag{26}$$

Where H^{-1} is the inverse Hadamard matrix. We then assume the errors e_j are random, and so we instead analyze the errors by their mean squares. The same is true for ε_i, where

$$\left\langle \varepsilon_i^2 \right\rangle = \sigma^2 \cdot \sum_j \left(H_{ij}^{-1} \right)^2 \tag{27}$$

In the trivial design of a sequential scan, the conversion matrix used is the identity matrix I, where for each measurement only a single signal is measured. In this case, the multiplexed error ε_i is equal to the random error e_j such that

$$\left\langle \varepsilon_i^2 \right\rangle = \left\langle e_j^2 \right\rangle = \sigma^2 \tag{28}$$

Nitzsche and Reisenberg define the 'gain' or Q factor as the ratio of noise reduction of the Hadamard transform vs the sequential scan by dividing the root mean squares of the errors associated with each method.[71] This is written mathematically as

$$Q_i = \frac{\sqrt{\left\langle \varepsilon_i^2 \right\rangle_{seq}}}{\sqrt{\left\langle \varepsilon_i^2 \right\rangle_{Had}}} \tag{29}$$

Then by inserting equations (27) and (28) into (29) we can describe the gain when the only source of noise is detector noise

$$Q_i = \frac{1}{\sqrt{\sum_j \left(H_{ij}^{-1}\right)^2}} \tag{30}$$

In this case, it is evident that any enhancement in the signal-to-noise ratio is determined by the size and kind of the Hadamard matrix used. In the case of S-matrices, each row is composed of a Walsh function which only differs from its neighbour by a single permutation. As such, a property of these S-matrices is that any element in the inverse matrix has the same absolute value of

$$\left|H_{ij}^{-1}\right| = \frac{2}{N+1} \tag{31}$$

Where *N* is the size of the matrix. Combining equations (30) and (31) determines the Q factor (signal to noise enhancement) in terms of the size of matrix used.

$$SNE = \frac{N+1}{2\sqrt{N}} \tag{32}$$

Here we observe an advantage in signal-to-noise ratio from using the Hadamard transform vs. a sequential method. Again, this is assuming that the source of the noise is noise from the detector (i.e., dark noise). Nitsche and Reisenberg further describe cases where shot noise (such as photon noise) dominates, in which case multiplexing only increases the noise. Based on the empirical SNE (3.37) measured in the experiments above, we can see an overall gain in signal when using the Hadamard Transform. This implies that dark noise is dominating over shot noise. Our system therefore likely operates well above the photon noise regime because our light source is relatively bright, and our acquisition times are long enough that we are not discerning between the arrival of individual photons. The theoretical SNE is 2.87, which is in fair agreement with the observed values. The SNE illustrates how useful a multiplexing technique is when dealing with noisy systems, or when speed is of the essence and integration times are short. Now, the HT imaging system can be applied to time-resolved experiments.

Chapter 4

Applications of the Five Dimensional Hadamard-Transform Fluorescence Imaging System

4.1 Introduction

Conventional EEM spectrometers use scanning monochromators to acquire spectra, which can take between 25 minutes to an hour[10] for a single EEM. Long acquisition times limit the applications of conventional EEM spectrometers to static solutions. Since most spectrometers measure the fluorescence at a single point in space, measurements are further limited to homogenous solutions and spectrometers provide no spatial information on how fluorescence intensities and fluorescence spectra features differ through the sample.

Here we describe a fluorescence imaging system that captures one full EEM for every pixel in an image. By leveraging the speed advantage afforded by the Hadamard-transform programmable light source, these four-dimensional (4D) images can be captured sequentially through time, yielding fluorescence information about heterogenous samples across five dimensions, as seen in Figure 4-1. Here the frame rate corresponds to about 0.1-1.0 fps.

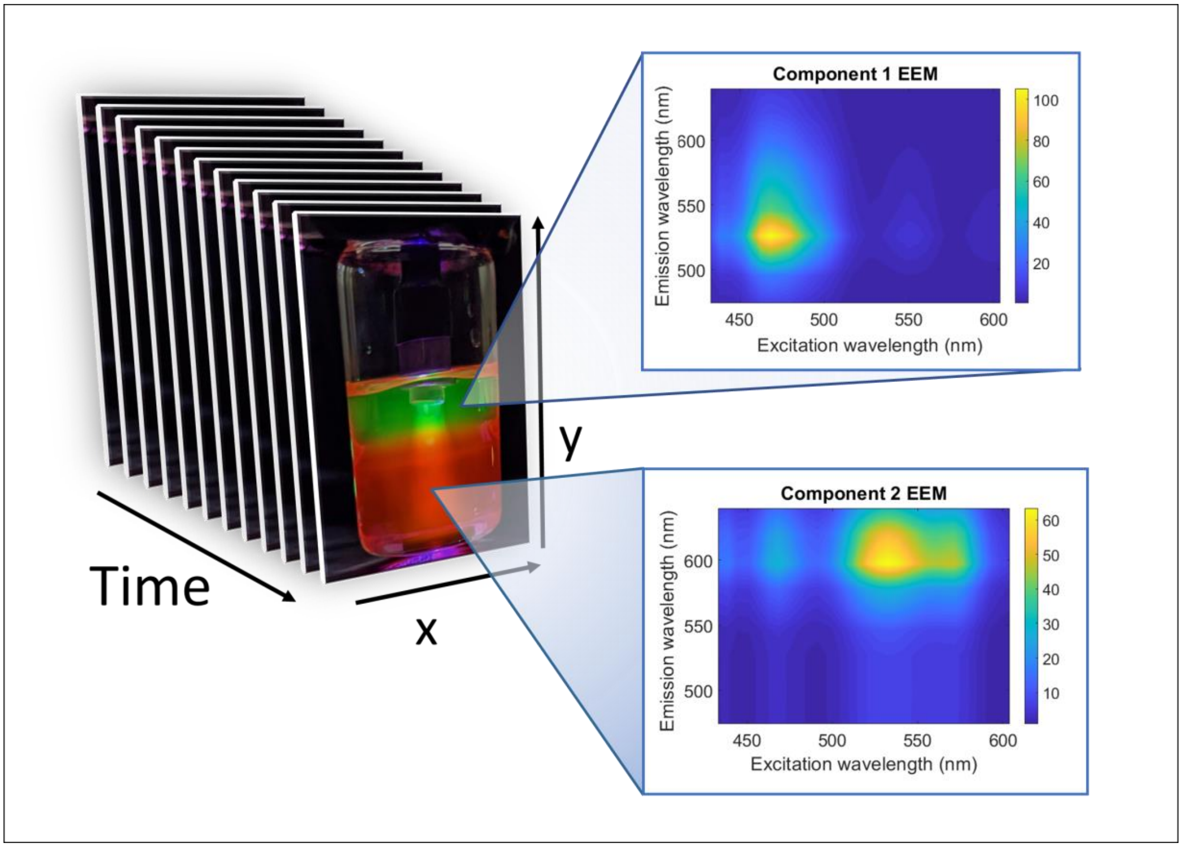

Figure 4-1 Illustration of a five dimensional dataset. Each frame of video has two spatial dimensions (x,y). Each pixel in the image corresponds to a full EEM having λ_{ex} and λ_{em} as two additional dimensions. Time is the fifth dimension in this data cube.

4.2 Preparation of a Two-Solvent Two-Fluorophore Mixture

A 20 µM solution of rhodamine B is prepared in glycerol in a 4-dram vial. A second solution of 20 µM fluorescein in basic (1 g/L KOH) deionized water is pipetted gently on top of the glycerol layer. While the two solvents are miscible, the high viscosity of glycerol prevents mixing if the mixture is undisturbed. The two-fluorophore / two-solvent mixture can be seen in Figure 4-2.

Figure 4-2 Fluorescein dissolved in basic water, layered on top of rhodamine B in glycerol. The stock solutions can be seen in the background of the image.

4.3 Temperature Ramp Experiment

Fluorescein and rhodamine B were chosen for this experiment because these fluorophores respond differently to temperature changes when heated. Rhodamine B undergoes a ring closing reaction to form a spirolactam,[72] seen in Figure 4-3. When the ring closes, π-conjugation is broken, and rhodamine B's fluorescence is diminished. By contrast, fluorescein's emission remains unaffected, when heated.

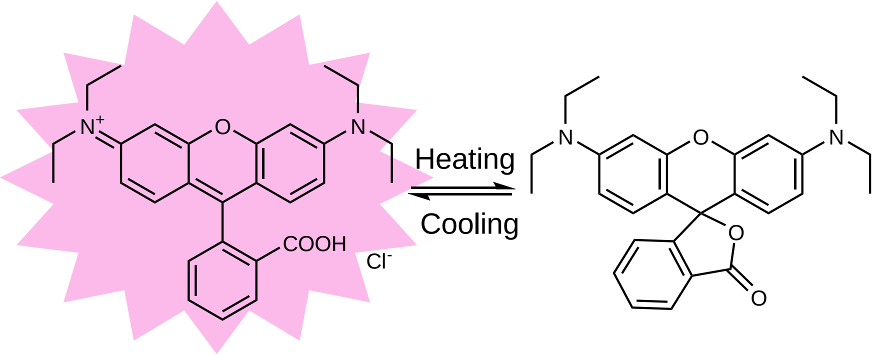

Figure 4-3 Rhodamine B Equilibrium. The dye forms an equilibrium between the fluorescent (ring-open) form and quenched (ring-closed) form.

The two-solvent two-fluorophore mixture is ideal for testing the full capabilities of the instrument. Not only does the fluorescence of the system change throughout the spectral domains of excitation and emission, but also through the spatial domains of *x* and *y* of the image. Lastly, by heating and then cooling the solution over time, we introduce variation in fluorescence in the temporal domain. Visually, the change can be observed in Figure 4-4, where the rhodamine B fluorescence is reduced when it is heated to 55°C.

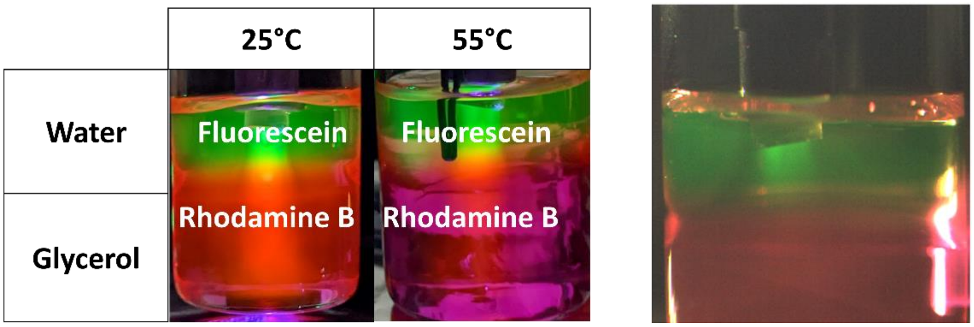

Figure 4-4 Two phase, two fluorophore system of fluorescein and rhodamine B (Left) before and after heating. (Right) false colour image from hyperspectral camera.

4.4 Results and PARAFAC Analysis

Over the course of 800 seconds (approximately 13 minutes), the mixture was heated and subsequently allowed to cool. 100 4D images in total were acquired during the heating and cooling, with the (x, y, λ_{em}, λ_{ex}) dimensions corresponding to 256×256×8×31. The camera gain was set to 1, black level set to 0, and the exposure time was 200 ms. The total acquisition time per spectrum was approximately 7-8 seconds/spectrum, with some variation due to the speed of data-transfer from the camera to the computer. The temperature of the mixture was logged concurrently with a thermocouple, and timestamps were acquired to ensure the temperature data could be aligned in time with the spectra from the imaging system.

Figure 4-5 shows slices of the 4D dataset at specific wavelengths corresponding to the excitation/emission of fluorescein (474.33 nm/546 nm) and rhodamine B (544.64 nm/597 nm). After 400 seconds of heating the mixture, one can see a decrease in intensity in the image slice at 544.64 nm/597 nm, which corresponds to the quenching of rhodamine B. after the solution is allowed to cool for a subsequent 400 seconds the fluorescence at this image slice returns.

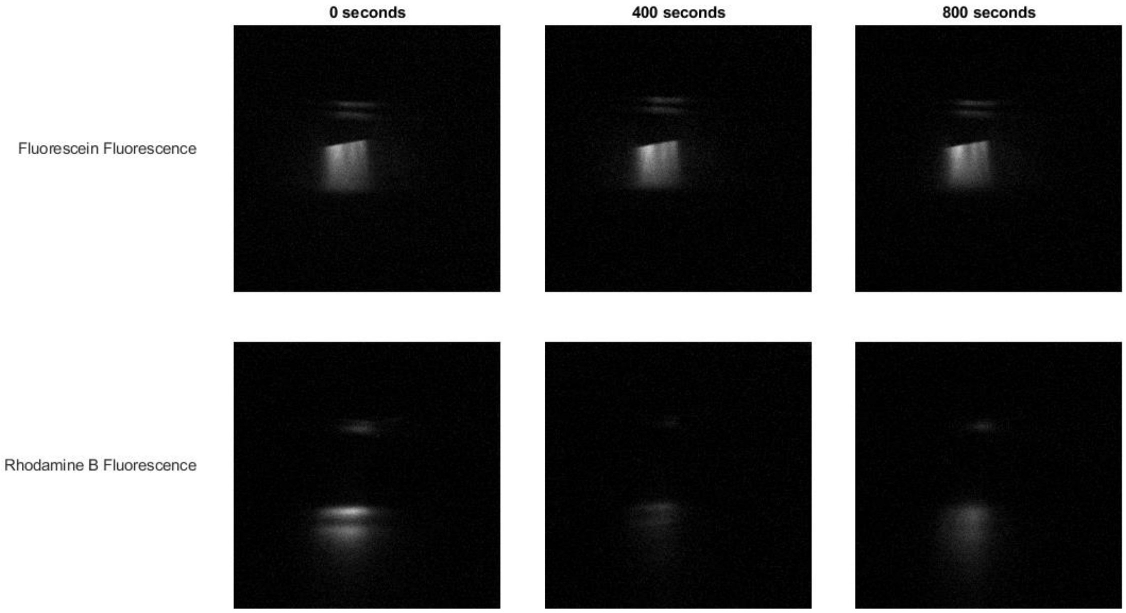

Figure 4-5 full resolution images of the two-component mixture. Images highlight the spectral regions that correspond to the fluorescence of fluorescein (top), and the fluorescence of rhodamine B (bottom), at the beginning of the experiment (left), at the peak of heating (middle), and after the solution is allowed to cool (right).

A significant portion of the images consist of dark pixels where the light source is not illuminating the mixture or is outside the sample vial. The spatial images were cropped from a full resolution of 256×256 to 91×50 so exclude any dark pixels from further data analysis. This has the dual effect of increasing the core consistency by the PARAFAC model from below 50% to 97% and the percent explained from 43% to 88%, as well as decreasing the size of the dataset and thus the time it takes for the algorithm to converge.

To model the 5D dataset with PARAFAC, some treatment is needed first. The dimensions *x* and *y* are not, in fact orthogonal, to one another, and so they must be linearized (or “unfolded”) into a single pixel number dimension. The dimensionality of the dataset is thus reduced to 4D for the purposes of PARAFAC fitting. The four-way array is fitted to a two-component PARAFAC model, with each component described by four vectors. The pixel number vector is then refolded to restore the *x* and *y* dimensions. This data treatment is illustrated in Figure 4-6. The component vectors obtained by PARAFAC analysis can be seen in Figure 4-7.

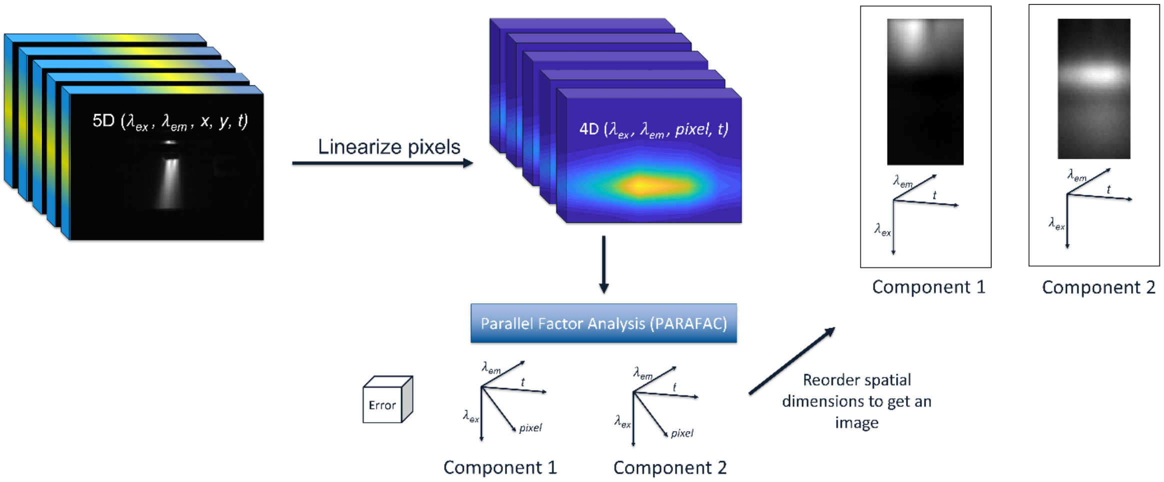

Figure 4-6 PARAFAC Workflow for 5D Datasets.

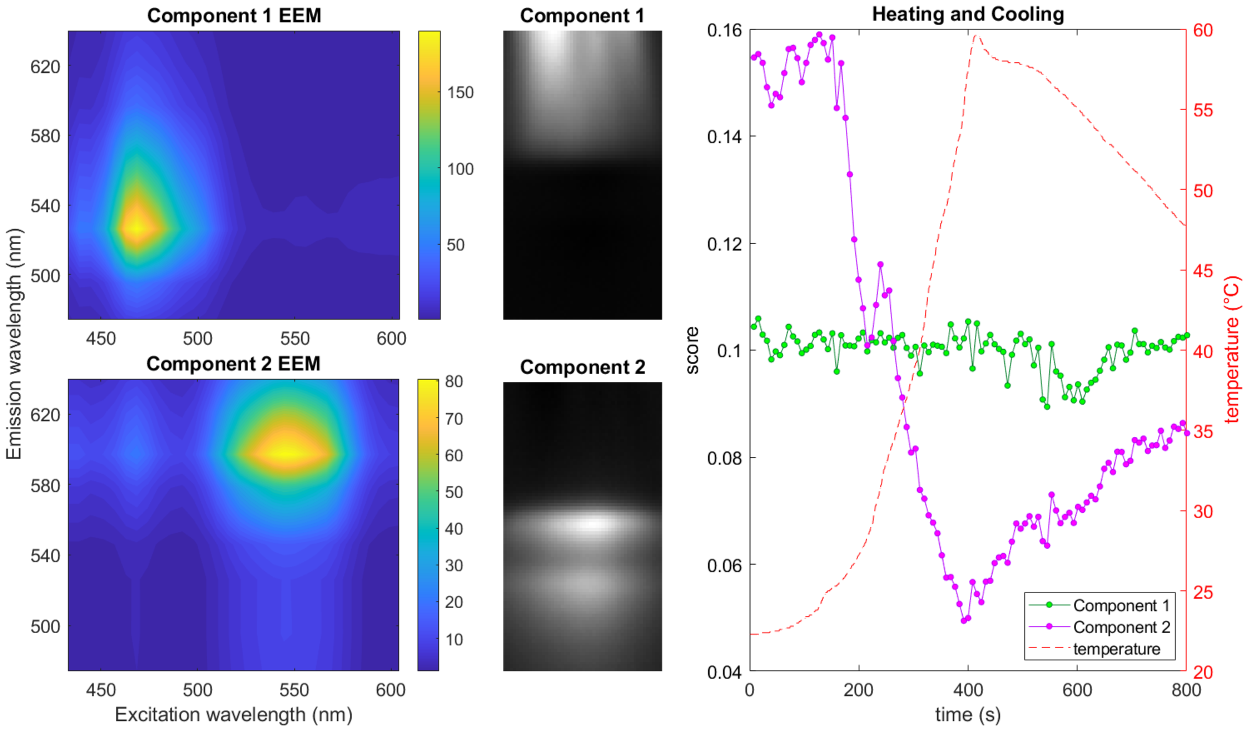

Figure 4-7 Tensor rank decomposition gives the vectors for excitation, emission, pixel value, and time for a two-component fit, with a core consistency of 97%. Fluorescein is component 1, and rhodamine B is component 2.

The PARAFAC model assigned the signal from fluorescein to component 1, and rhodamine B to component 2. This can be inferred from both the signature EEM spectra, and the spatial positions in the image. Fluorescein is found on the top phase of the mixture, while rhodamine B is found in the bottom phase. The rightmost plot in Figure 4-7 shows the loading vectors for component 1 and 2, overlaid with the temperature of the mixture at the corresponding timestamp. These loading vectors correspond to the fluorescence intensity of each of the components (their “score”) at the respective time step. As the temperature increases, the PARAFAC score for component 2 (rhodamine B) decreases, and then increases after the temperature is lowered again. The PARAFAC score for component 1 remains relatively stable and is, therefore, independent of temperature.

To more directly visualize the effect of temperature on the fluorescence intensity, the PARAFAC scores can be plotted against the temperature at that time, as seen in Figure 4-8. Component 2 shows a negative dependence on temperature, where at higher temperatures the score is decreased. Component 2 also shows a distinct hysteresis; at a given temperature, the score is higher if the mixture was being cooled vs. being heated. The hysteresis could be explained by the depth of the temperature probe, where the fluorescence has a chance to respond to a change in temperature before the heat reaches the temperature probe.

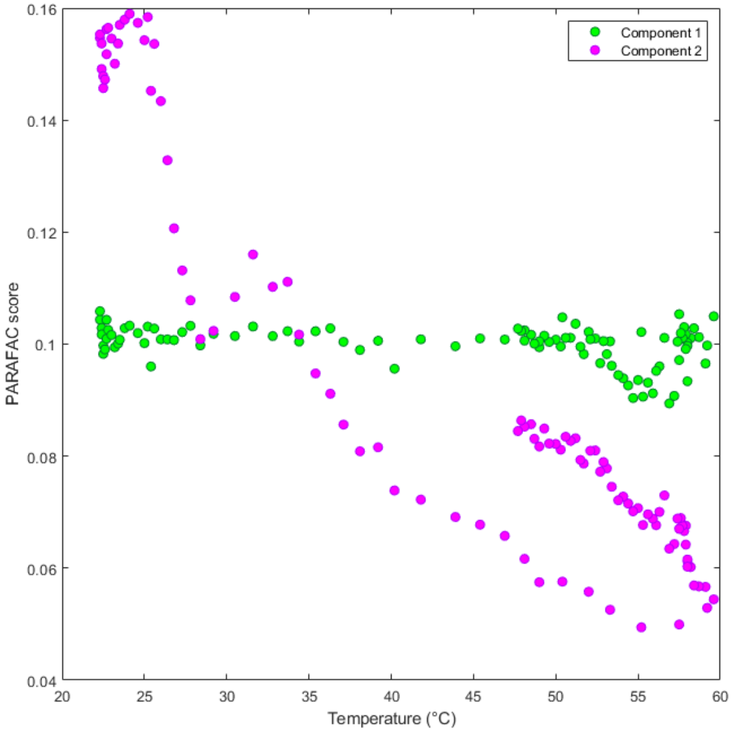

Figure 4-8 Plot of PARAFAC scores as a function of temperature. Component 1 shows an independence of temperature, while component 2 decreases with increased temperature.

4.5 Conclusion

The Hadamard transform imaging system was successful in separating out a multi-fluorophore multi-phase system and identifying not only what fluoresces at a given excitation or emission, but also where the fluorescence occurs spatially in an inhomogeneous mixture. The increased signal to noise ratio afforded by the Hadamard transform means the imaging system can acquire 100 spectra in 800 seconds.

This sample experiment highlights potential applications for the system in future kinetic studies of inhomogeneous mixtures.

Chapter 5

Conclusions and Future Work

5.1 Thesis Summary

As described at the end of Chapter 1, the project goal was to design and build an imaging system which captures an excitation emission matrix for every pixel in an image, and to make this process fast enough to observe and characterize chemical transformations in real time. The HT-EEM imaging system described in this thesis has largely met the stated goal. It captures fluorescence of a dynamic system rapidly in two spatial and two spectral dimensions. By leveraging the multiplex advantage of the Hadamard-transform and the speed of snapshot hyperspectral imaging, a single four-dimensional image could be acquired in less than 8 seconds, where each pixel consisted of an EEM with 8 emission channels and 31 excitation channels. Using a tighter mirror spacing, the spectral resolution of the excitation could be set as low as FWHM = 6.79 nm. The images consist of 256 by 256 pixels with a spatial resolution of 100 µm per pixel, and a higher spatial resolution is easily achievable by replacing the camera optics. Because every pixel corresponds to one EEM, every image yields 65,536 EEMs, a massive increase in the information density as compared to the single-point EEM spectroscopy method used exclusively in the published literature. Using the multivariate analysis method PARAFAC, the large raw dataset can be decomposed into the component fluorophores, and the contribution of each of the components to the overall emission in space (x,y) and time (t) can be identified.

The experimental design in Chapter 4 is may seem simplistic (the same conclusions could have been drawn by simply observing the phases with the naked eye); However, the design was purposely kept straightforward to showcase how impressively information dense even such simple systems are using this newly developed imaging system.

Future applications this imaging system are discussed in section 5.2.5 below and include imaging of cells and tissue using microscopy, the time evolution of fluorescence markers in high throughput assays, and quality control in an industrial food or drug setting such as monitoring batches for impurities in the spectra.

There are several limitations of the system that are to be addressed in the future. The low light throughput of the programmable light source significantly limits speed of acquisition and size of the area that is possible to image. Low excitation light intensity requires larger integration times and/or smaller irradiated volumes. With the current configuration, the largest area that the light source can illuminate is approximately one square centimeter. This area would need to be drastically increased for many of the applications discussed below. Future work to increase light throughput is discussed in section 5.2.3. The size of the datasets and the respective demands on random access memory (RAM), data storage, and data processing capacity are another major limitation of the instrument. Each pixel is stored as an 8-bit unsigned integer, and we require 134 megabytes per raw 4D image (each raw image being 2048×2048 pixels, and 31 excitation images with one blank image). This is the memory and data storage requirement for a single frame in the time series. The memory and storage requirements scale with the acquisition rate and duration of the experiment. We are at risk of becoming a victim of our own innovation - considering that the acquisition time was vastly accelerated by virtue of Hadamard-transform multiplexing. Consider that we require 13.4 gigabytes for a 13-minute-long experiment (such as the one performed in section 4.4) where 100 4D images are acquired. Larger datasets take longer to save, load, and importantly, fit to PARAFAC models. The size of the dataset has an impact during the experiment as well. Since speed is of the essence when studying kinetics, all raw images are temporarily saved to the computer’s random-access memory (RAM) during acquisition. The computer is thus required to have enough RAM to store the entire dataset (it is currently outfitted with 96 gigabytes of RAM). As the kinetics experiments which we study become inevitably longer (over one or several hours), the computer’s RAM will likely become insufficient to store the entire dataset. A new solution, such as saving to the hard drive throughout the experiment, will need to be implemented, at the cost of potential speed.

5.2 Applications and Future Works

5.2.1 Increasing Excitation Range with UV-LED Light Source

In the current iteration of the device, the excitation light range extends between approximately 430 nm to 600 nm, depending on the alignment. Due to a UV filter on the protective window in front of the micromirror array, the DMD is only able to reflect light in the visible region. However, UV wavelengths are the excitation maximum for many common dyes and fluorophores, and the lack of UV excitation light is a limitation of the current device. Travis Ferguson in the Loock group has previously demonstrated HT-EEM spectroscopy using a bank of UV-LEDs, which can be modulated on or off in a Hadamard pattern. Coupling these LEDs to the existing DMD light source would allow for a wider range of wavelengths to be used in the context of imaging, broadening the utility and applications for which the HT-EEM imaging system can be deployed.

5.2.2 Confocal Microscopy with Laser Excitation Light Source

As discussed in Chapter 0, fluorescence imaging is widely applied to study tissue, cells, and other (micro)biological matter, using techniques such as confocal laser scanning microscopy (CLSM). Compared to conventional microscopy, CLSM acquires images with significantly higher spatial resolution, unfortunately at the expense of the extra time required to raster-scan the image plane. The emission is selected either with emission filters or a dispersive element and CCD, while the excitation is usually only a single narrow laser wavelength (some designs may have multiple excitation lasers and a sequential acquisition at each excitation). HT-EEM Imaging can be adapted to CLSM by replacing the DMD excitation light source with a fully programmable bank of laser light sources that is operated similarly to the UV-LED programmable light source developed by Travis Ferguson. This method would decrease the acquisition time required at each point in the spatial raster scan by leveraging the multiplex advantage. Emma Abbey in the Loock group is has been developing a bank of lasers which can be rapidly modulated on or off to perform single-point HT-EEM spectroscopy, and this light source could be adapted in the future to perform CLSM with HT. Some of the high temporal resolution from the current

HT-EEM imaging technique would be sacrificed, in exchange for the high spatial resolution afforded to the confocal method.

5.2.3 Increasing Light Throughput

The programmable light source was initially designed for the purpose of single point spectroscopy and was not purposely built to illuminate a camera's field of view. Currently the light source is simply not bright enough to illuminate an area wider than approximately one square centimeter, and to do so the fiber probe must be submerged in a liquid sample (it is not bright enough to cause a fluorophore to fluoresce on a TLC plate, for example). There are several ways to increase the light throughput; both upgrades mentioned above (the UV-LED and laser light source) would have the added side effect of increasing the light to the sample. A third option available to increase light throughput is to replace the white LED in the DMD setup with a brighter broadband source, such as a supercontinuum light source, or fiber coupled plasma source. Both types of light sources are commercially available but expensive.

5.2.4 Push-Broom Camera Design for Optimized Spectral and Spatial Resolution

The current HT-EEM imaging system was designed to be a compromise between spatial, spectral, and temporal resolution. To increase the resolution of one domain often results in a decrease in the resolution of another. The imaging system can be reoptimized to favour a specific domain, to better fit the system to a particular application. As discussed in section 2.6, snapshot hyperspectral imaging was chosen because of the best compromise it offered between spatial, spectral, and temporal resolution. It is said that there are no winners in a compromise and, as is evident from the spectra and images acquired, the spatial resolution (256×256 pixels) and spectral resolution of the emission (8 channels) suffer as a result. The snapshot hyperspectral camera could be swapped out for a spatially scanning (push-broom) camera, to optimize the camera design for spectral and spatial resolution in exchange for temporal resolution. One such design has been made available by Sigerne et. al.[52] in which they provide the instructions and parts to build a "Do-it-Yourself" hyperspectral camera. A rendering of the design can be seen in Figure 5-2 below.

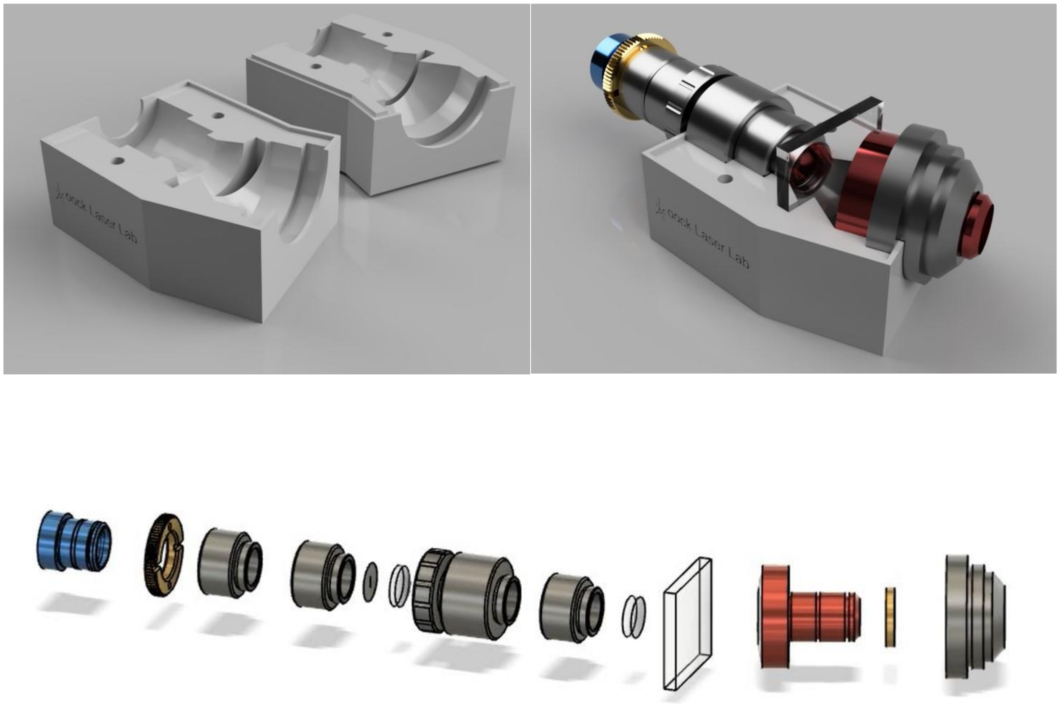

Figure 5-1 Design and Rendering for a Push-Broom Hyperspectral Camera Front Lens Assembly. Design adapted from Sigernes et al.[52]

In the push-broom design, light from the subject passes through a slit aperture, and is dispersed by a transmission grating onto a 2D CCD array to measure the emission wavelength spectrum and *x* spatial dimension simultaneously. The camera is then translated along the *y* dimension to capture the full data-cube in a sequence of acquisitions. The design allows for a significant improvement in spectral resolution, with a FWHM of 1.4 nm and a spectral range of 400-700 nm (depending on the camera sensor used).[52] The spatial resolution is no longer limited by the pixelation of the camera. The push-broom camera allows the *x* dimension to be captured with the full vertical resolution of the camera's sensor (unlike the current snapshot camera, which only uses every 8th pixel due to the filter array), and the *y* dimension's resolution is limited by the size of the steps when the camera is translated (this also allows for a very wide field of view, because there is no limit on how far the camera is translated either).

5.2.5 Instrument Design for High Throughput Assays

One eventual goal is to apply HT-EEM imaging to high throughput assays. Since every pixel provides a complete EEM, spatially separated samples (as in a well-plate) can be measured simultaneously under the field of view of the camera, if the wells are sufficiently illuminated by the light source. However, most well-plates are considerably larger than the area we can illuminate with the light source in its current form. As mentioned previously, light throughput is critical to ensuring good quality spectra. A possible design for a well-plate assay is shown below in Figure 5-2. As before, the modulated light from the DMD is collected into a fiber bundle, however instead each fiber in the bundle is coupled to the bottom of a well in a well-plate. The excitation light is more efficiently delivered to the fluorophore in the well as compared to simply illuminating the general area from above the well-plate. A camera is placed in a diascopic orientation with respect to the light source.

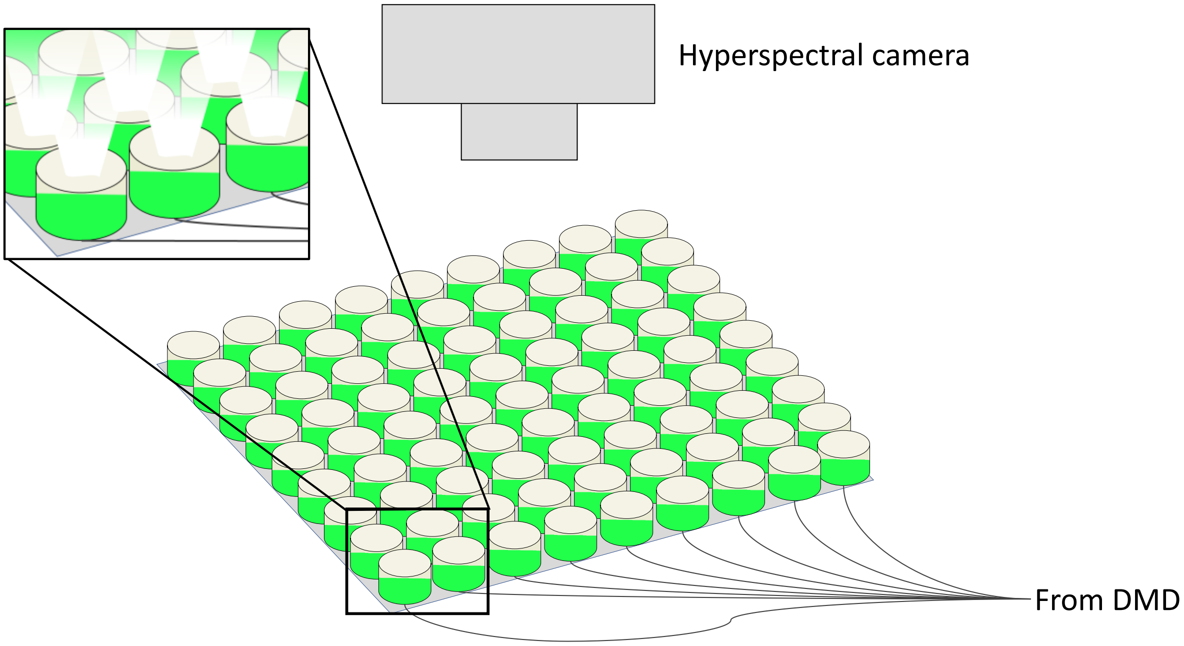

Figure 5-2 Illustration of a fiber-coupled well-plate for HT-EEM assay imaging.

An alternative design could involve bifurcated fibers for each of the wells and a camera that images just 96 “pixels” with high temporal and spectral resolution.

5.2.6 Summary of Potential Applications

The above list of potential application illustrates that our method has considerable potential in a variety of fields in quality control, imaging, chemical kinetics, and process monitoring. Far more applications can be envisioned.

Fluorescence spectroscopy is a mature field, and it appears impossible to make genuinely new contributions to the design of fluorescence spectrometers. Nevertheless, we hope that the present work could illustrate an unrealized potential of fluorescence spectroscopy when taken to a “higher dimension”. The unique combination of hyperspectral imaging and Hadamard-transform multiplexing allows for an information acquisition rate that is, to the best of our knowledge, unprecedented.

References

(1) Lin, Y.-W.; Chiu, T.-C.; Chang, H.-T. Laser-induced fluorescence technique for DNA and proteins separated by capillary electrophoresis. *Journal of Chromatography B* **2003**, *793* (1), 37-48. DOI: https://doi.org/10.1016/S1570-0232(03)00363-5.

(2) Fraga, M. F.; Ballestar, E.; Esteller, M. Capillary electrophoresis-based method to quantitate DNA–protein interactions. *Journal of Chromatography B* **2003**, *789* (2), 431-435. DOI: https://doi.org/10.1016/S1570-0232(03)00103-X.

(3) Airado-Rodríguez, D.; Durán-Merás, I.; Galeano-Díaz, T.; Wold, J. P. Front-face fluorescence spectroscopy: A new tool for control in the wine industry. *Journal of Food Composition and Analysis* **2011**, *24* (2), 257-264. DOI: https://doi.org/10.1016/j.jfca.2010.10.005.

(4) Itakura, K.; Saito, Y.; Suzuki, T.; Kondo, N.; Hosoi, F. Estimation of Citrus Maturity with Fluorescence Spectroscopy Using Deep Learning. *HORTICULTURAE* **2019**, *5* (1). DOI: 10.3390/horticulturae5010002.

(5) Yu, J.; Xiao, K.; Xue, W.; Shen, Y.-x.; Tan, J.; Liang, S.; Wang, Y.; Huang, X. Excitation-emission matrix (EEM) fluorescence spectroscopy for characterization of organic matter in membrane bioreactors: Principles, methods and applications. *Frontiers of Environmental Science & Engineering* **2020**, *14* (2), 31. DOI: 10.1007/s11783-019-1210-8.

(6) Omrani, H.; Dudelzak, A. E.; Hollebone, B. P.; Loock, H.-P. Assessment of the oxidative stability of lubricant oil using fiber-coupled fluorescence excitation–emission matrix spectroscopy. *Analytica Chimica Acta* **2014**, *811*, 1-12. DOI: https://doi.org/10.1016/j.aca.2013.10.019.

(7) Andrews, N. L. P.; Fan, J. Z.; Omrani, H.; Dudelzak, A.; Loock, H. P. Comparison of lubricant oil antioxidant analysis by fluorescence spectroscopy and linear sweep voltammetry. *Tribology International* **2016**, *94*, 279-287. DOI: https://doi.org/10.1016/j.triboint.2015.08.023.

(8) Peng, L.; Gardecki, J.; Bouma, B.; Tearney, G. Fourier fluorescence spectrometer for excitation emission matrix measurement. *Optics express* **2008**, *16*, 10493-10500. DOI: 10.1364/OE.16.010493.

(9) Loock, H.-P.; Reich, O.; Andrews Nicholas, L. P. Multiplexed Excitation Emission Matrix Spectroscopy. US US 2017/0052118 A1, 2017.

(10) Andrews, N. L. P.; Ferguson, T.; Rangaswamy, A. M. M.; Bernicky, A. R.; Henning, N.; Dudelzak, A.; Reich, O.; Barnes, J. A.; Loock, H. P. Hadamard-Transform Fluorescence Excitation-Emission-Matrix Spectroscopy. *Anal Chem* **2017**, *89* (16), 8554-8564. DOI: 10.1021/acs.analchem.7b02400 From NLM PubMed-not-MEDLINE.

(11) Bernicky, A.; Ferguson, T.; Denotter, S.; Rigg, A.; Loock, H. P. Simultaneous Double-Pass Absorption and Fluorescence Excitation-Emission Matrix Spectroscopy for Measurements of Reaction Kinetics. *Anal Chem* **2020**, *92* (18), 12489-12497. DOI: 10.1021/acs.analchem.0c02320 From NLM Medline.

(12) Ferguson, T.; Bernicky, A.; Kozin, I.; Loock, H. P. HPLC-Detector Based on Hadamard-Transform Fluorescence Excitation-Emission-Matrix Spectroscopy. *Anal Chem* **2021**, *93* (23), 8116-8121. DOI: 10.1021/acs.analchem.1c01037 From NLM Medline.

(13) Zavala, A. G.; Kulkarni, A. S.; Fortunato, E. A. A dual color Southern blot to visualize two genomes or genic regions simultaneously. *J Virol Methods* **2014**, *198*, 64-68. DOI: 10.1016/j.jviromet.2013.12.019 From NLM.

(14) Eykholt, R. L.; Mitchell, M. D.; Marvin, K. W. Direct imaging of Northern blots on an optical scanner using ethidium bromide. *BioTechniques* **2000**, *28* (5), 864-870.

(15) Luthman, A. S.; Dumitru, S.; Quiros-Gonzalez, I.; Joseph, J.; Bohndiek, S. E. Fluorescence hyperspectral imaging (fHSI) using a spectrally resolved detector array. *Journal of Biophotonics* **2017**, *10* (6-7), 840-853. DOI: 10.1002/jbio.201600304.

(16) McNamara, L. E.; Dalby, M. J.; Riehle, M. O.; Burchmore, R. Fluorescence two-dimensional difference gel electrophoresis for biomaterial applications. *Journal of The Royal Society Interface* **2010**, *7* (suppl_1), S107-S118. DOI: 10.1098/rsif.2009.0177.focus (acccessed 2022/08/17).

(17) Hell, S. W.; Wichmann, J. Breaking the diffraction resolution limit by stimulated emission: stimulated-emission-depletion fluorescence microscopy. *Opt. Lett.* **1994**, *19* (11), 780-782. DOI: 10.1364/OL.19.000780.

(18) Moerner, W. E.; Kador, L. Optical detection and spectroscopy of single molecules in a solid. *Physical Review Letters* **1989**, *62* (21), 2535-2538. DOI: 10.1103/PhysRevLett.62.2535.

(19) Betzig, E.; Patterson, G. H.; Sougrat, R.; Lindwasser, O. W.; Olenych, S.; Bonifacino, J. S.; Davidson, M. W.; Lippincott-Schwartz, J.; Hess, H. F. Imaging Intracellular Fluorescent Proteins at Nanometer Resolution. *Science* **2006**, *313* (5793), 1642-1645. DOI: doi:10.1126/science.1127344.

(20) Sinclair, M. B.; Timlin, J. A.; Haaland, D. M.; Werner-Washburne, M. Design, construction, characterization, and application of a hyperspectral microarray scanner. *Appl. Opt.* **2004**, *43* (10), 2079-2088. DOI: 10.1364/AO.43.002079.

(21) Mattheyses, A. L.; Simon, S. M.; Rappoport, J. Z. Imaging with total internal reflection fluorescence microscopy for the cell biologist. *J Cell Sci* **2010**, *123* (Pt 21), 3621-3628. DOI: 10.1242/jcs.056218 From NLM.

(22) Rahman, M. M.; Bui, M. V.; Shibata, M.; Nakazawa, N.; Rithu, M. N. A.; Yamashita, H.; Sadayasu, K.; Tsuchiyama, K.; Nakauchi, S.; Hagiwara, T.; et al. Rapid noninvasive monitoring of freshness variation in frozen shrimp using multidimensional fluorescence imaging coupled with chemometrics. *Talanta* **2021**, *224*, 121871. DOI: https://doi.org/10.1016/j.talanta.2020.121871.

(23) Abamba Omwange, K.; Al Riza, D. F.; Saito, Y.; Suzuki, T.; Ogawa, Y.; Shiraga, K.; Giametta, F.; Kondo, N. Potential of front face fluorescence spectroscopy and fluorescence imaging in discriminating adulterated extra-virgin olive oil with virgin olive oil. *Food Control* **2021**, *124*, 107906. DOI: https://doi.org/10.1016/j.foodcont.2021.107906.

(24) Herzka, D. A.; Kotys, M. S.; Krueger, S.; Traughber, B. J.; Heroux, J.; Gharib, A. M.; Ohayon, J.; Weiss, S.; Pettigrew, R. I.; Wood, B. J. MR-guided catheter-based excitation emission optical spectroscopy for in vivo tissue characterization. In *Proc.SPIE*, 2008; Vol. 6918, p 69181U. DOI: 10.1117/12.770758.

(25) Lakowicz, J. R. *Principles of Fluorescence Spectroscopy*; Springer, 2006. DOI: 10.1007/978-0-387-46312-4.

(26) Yamaguchi, Y.; Matsubara, Y.; Ochi, T.; Wakamiya, T.; Yoshida, Z.-I. How the π Conjugation Length Affects the Fluorescence Emission Efficiency. *Journal of the American Chemical Society* **2008**, *130*. DOI: 10.1021/ja808258q.

(27) Czerny, M.; Turner, A. F. Über den Astigmatismus bei Spiegelspektrometern. *Zeitschrift fur Physik* **1930**, *61*, 792-797. DOI: 10.1007/bf01340206.

(28) O'Connor, D. *Time-correlated single photon counting*; Elsevier Science, 2012.

(29) Sun, Y.; Hatami, N.; Yee, M.; Phipps, J.; Elson, D. S.; Gorin, F.; Schrot, R. J.; Marcu, L. Fluorescence lifetime imaging microscopy for brain tumor image-guided surgery. *Journal of Biomedical Optics* **2010**, *15*, 056022-056022-056025. DOI: 10.1117/1.3486612.

(30) Franco, W.; Gutierrez-Herrera, E.; Kollias, N.; Doukas, A. Review of applications of fluorescence excitation spectroscopy to dermatology. *British Journal of Dermatology* **2016**, *174* (3), 499-504. DOI: https://doi.org/10.1111/bjd.14221.

(31) Kricka, L. J.; Fortina, P. Analytical Ancestry: "Firsts" in Fluorescent Labeling of Nucleosides, Nucleotides, and Nucleic Acids. *Clinical Chemistry* **2009**, *55* (4), 670-683. DOI: 10.1373/clinchem.2008.116152 (acccessed 7/21/2022).

(32) Moerner, W. E.; Fromm, D. P. Methods of single-molecule fluorescence spectroscopy and microscopy. *Review of Scientific Instruments* **2003**, *74* (8), 3597-3619. DOI: 10.1063/1.1589587.

(33) Dubnick, A.; Barker, J.; Sharp, M.; Wadham, J.; Lis, G.; Telling, J.; Fitzsimons, S.; Jackson, M. Characterization of dissolved organic matter (DOM) from glacial environments using total fluorescence spectroscopy and parallel factor analysis. *Annals of Glaciology* **2010**, *51* (56), 111-122. DOI: 10.3189/172756411795931912 From Cambridge University Press Cambridge Core.

(34) Li, L.; Wang, Y.; Zhang, W.; Yu, S.; Wang, X.; Gao, N. New advances in fluorescence excitation-emission matrix spectroscopy for the characterization of dissolved organic matter in drinking water treatment: A review. *Chemical Engineering Journal* **2020**, *381*, 122676. DOI: https://doi.org/10.1016/j.cej.2019.122676.

(35) Andrews, N. L.; Fan, J. Z.; Forward, R. L.; Chen, M. C.; Loock, H. P. Determination of the thermal, oxidative and photochemical degradation rates of scintillator liquid by fluorescence EEM spectroscopy. *Phys Chem Chem Phys* **2016**, *19* (1), 73-81. DOI: 10.1039/c6cp06015c From NLM PubMed-not-MEDLINE.

(36) Fellgett, P. B. Theory of infrared sensitivities and its application to investigations of stellar radiation in the near infrared. 1951. https://ui.adsabs.harvard.edu/abs/1951PhDT........24F.

(37) Agaian, S. S.; Sarukhanyan, H.; Egiazarian, K.; Astola, J. Hadamard transforms. 2011; SPIE.

(38) Draper, T. G. Addition on a quantum computer. *arXiv preprint quant-ph/0008033* **2000**.

(39) Nelson, E. D.; Fredman, M. L. Hadamard Spectroscopy. *J. Opt. Soc. Am.* **1970**, *60* (12), 1664-1669. DOI: 10.1364/JOSA.60.001664.

(40) Graff, D. K. Fourier and Hadamard - Transforms in Spectroscopy. *Journal of Chemical Education* **1995**, *72* (4), 304-309. DOI: DOI 10.1021/ed072p304.

(41) Marshall, A. G.; Comisarow, M. B. Fourier and Hadamard Transform Methods in Spectroscopy. *Analytical Chemistry* **1975**, *47* (4), A491-&. DOI: DOI 10.1021/ac60354a028.

(42) MacLean, A. G.; Schneider, L. T.; Freytag, A. I.; Gribble, A.; Barnes, J. A.; Loock, H.-P. Cavity-enhanced photoacoustic detection using acoustic and fiber-optic resonators. *Applied Physics B* **2014**, *119* (1), 11-19. DOI: 10.1007/s00340-014-5969-9.

(43) Hedayat, A.; Wallis, W. D. Hadamard Matrices and Their Applications. *The Annals of Statistics* **1978**, *6* (6), 1184-1238, 1155.

(44) Tan, Y.; Jiang, J.-H.; Wu, H.-L.; Cui, H.; Yu, R.-Q. Resolution of kinetic system of simultaneous degradations of chlorophyll a and b by PARAFAC. *Analytica chimica acta* **2000**, *412* (1), 195-202. DOI: 10.1016/S0003-2670(99)00813-2.

(45) Hagen, N.; Kudenov, M. W. Review of snapshot spectral imaging technologies. *Optical Engineering* **2013**, *52* (9). DOI: 10.1117/1.Oe.52.9.090901.

(46) Arablouei, R.; Goan, E.; Gensemer, S.; Kusy, B. Fast and robust pushbroom hyperspectral imaging via DMD-based scanning. *Proc Spie* **2016**, *9948*. DOI: Artn99480a10.1117/12.2239107.

(47) Wang, Y.; Reder, N.; Kang, S.; Glaser, A.; Liu, J. Multiplexed Optical Imaging of Tumor-Directed Nanoparticles: A Review of Imaging Systems and Approaches. *Nanotheranostics* **2017**, *1*, 369-388. DOI: 10.7150/ntno.21136.

(48) HERRALA, E.; OKKONEN, J. IMAGING SPECTROGRAPH AND CAMERA SOLUTIONS FOR INDUSTRIAL APPLICATIONS. *International Journal of Pattern Recognition and Artificial Intelligence* **1996**, *10* (01), 43-54. DOI: 10.1142/s0218001496000050.

(49) Heia, K.; Sivertsen, A. H.; Stormo, S. K.; Elvevoll, E.; Wold, J. P.; Nilsen, H. Detection of Nematodes in Cod (Gadus morhua) Fillets by Imaging Spectroscopy. *Journal of Food Science* **2007**, *72* (1), E011-E015. DOI: https://doi.org/10.1111/j.1750-3841.2006.00212.x.

(50) Sigernes, F.; Lorentzen, D. A.; Heia, K.; Svenøe, T. Multipurpose spectral imager. *Appl. Opt.* **2000**, *39* (18), 3143-3153. DOI: 10.1364/AO.39.003143.

(51) Karaca, A. C.; Erturk, A.; Güllü, M.; Elmas, m.; Erturk, S. *Automatic waste sorting using shortwave infrared hyperspectral imaging system*; 2013. DOI: 10.1109/WHISPERS.2013.8080744.

(52) Sigernes, F.; Syrjasuo, M.; Storvold, R.; Fortuna, J.; Grotte, M. E.; Johansen, T. A. Do it yourself hyperspectral imager for handheld to airborne operations. *Opt Express* **2018**, *26* (5), 6021-6035. DOI: 10.1364/OE.26.006021 From NLM PubMed-not-MEDLINE.

(53) Bell III, J. F.; Squyres, S. W.; Herkenhoff, K. E.; Maki, J. N.; Arneson, H. M.; Brown, D.; Collins, S. A.; Dingizian, A.; Elliot, S. T.; Hagerott, E. C.; et al. Mars Exploration Rover Athena Panoramic Camera (Pancam) investigation. *Journal of Geophysical Research: Planets* **2003**, *108* (E12). DOI: https://doi.org/10.1029/2003JE002070.

(54) Bell, J. F.; Maki, J. N.; Mehall, G. L.; Ravine, M. A.; Caplinger, M. A.; Bailey, Z. J.; Brylow, S.; Schaffner, J. A.; Kinch, K. M.; Madsen, M. B.; et al. The Mars 2020 Perseverance Rover Mast Camera Zoom (Mastcam-Z) Multispectral, Stereoscopic Imaging Investigation. *Space Science Reviews* **2021**, *217* (1), 24. DOI: 10.1007/s11214-020-00755-x.

(55) Bell, J. F.; Godber, A.; McNair, S.; Caplinger, M. A.; Maki, J. N.; Lemmon, M. T.; Van Beek, J. K.; Malin, M. C.; Wellington, D. F.; Kinch, K. M.; et al. The Mars Science Laboratory Curiosity rover Mastcam instruments: Preflight and in-flight calibration, validation, and data archiving. *Earth and Space Science* **2017**, *4*, 396 - 452.

(56) Bowen, I. S. The Image-Slicer a Device for Reducing Loss of Light at Slit of Stellar Spectrograph. *The Astrophysical Journal* **1938**, *88*, 113. DOI: 10.1086/143964.

(57) Vanderriest, C. A fiber-optics dissector for spectroscopy of nebulosities around quasars and similar objects. *Publications of the Astronomical Society of the Pacific* **1980**, *92*, 858. DOI: 10.1086/130764.

(58) Courtes, G.; Georgelin, Y.; Bacon, R.; Monnet, G.; Boulesteix, J. A New Device for Faint Objects High Resolution Imagery and Bidimensional Spectrography. New York, NY, 1988; Springer New York: pp 266-274.

(59) Bleukens, d.; Adrianus, A. J.; De Haan, a.; by Friedrich, J.; Stoffels; Jacobus; Peters; Petrus, J. M. Color splitting prism assembly. US US RE030513 E, 1981.

(60) Xiong, Y.; Fu, Y. Multi-spectral imaging system. CN CN 106840400 A, 2017.

(61) Bayer Bryce, E. Color imaging array. US US 3971065 A, 1976.

(62) Lidan, M.; Hairong, Q.; Snyder, W. E. A generic method for generating multispectral filter arrays. Piscataway NJ, 2004, IEEE: Vol. 5, pp 3343-3346 Vol. 3345. DOI: 10.1109/ICIP.2004.1421830.

(63) Bro, R. PARAFAC. Tutorial and applications. *Chemometrics and Intelligent Laboratory Systems* **1997**, *38* (2), 149-171. DOI: https://doi.org/10.1016/S0169-7439(97)00032-4.

(64) Bernicky, A. The Advancement Of Hadamard-Transform Excitation Emission-Matrix Spectroscopy. Queen's University, 2020.

(65) Hornbeck Larry, J. Spatial light modulator and method. US US 5061049 A, 1991.

(66) Horenstein, M. N.; Pappas, S.; Fishov, A.; Bifano, T. G. Electrostatic micromirrors for subaperturing in an adaptive optics system. *Journal of Electrostatics* **2002**, *54* (3), 321-332. DOI: https://doi.org/10.1016/S0304-3886(01)00159-0.

(67) *lorentzfit*; MATLAB Central File Exchange: 2011. (accessed July 20 2022).

(68) Bahram, M.; Bro, R.; Stedmon, C.; Afkhami, A. Handling of Rayleigh and Raman scatter for PARAFAC modeling of fluorescence data using interpolation. *Journal of Chemometrics* **2006**, *20* (3-4), 99-105. DOI: 10.1002/cem.978.

(69) Dietrich, O.; Raya, J.; Reeder, S.; Reiser, M.; Schoenberg, S. Measurement of signal-to-noise ratios in MR images: Influence of multichannel coils, parallel imaging, and reconstruction filters. *Journal of Magnetic Resonance Imaging* **2007**, *26*, 375-385. DOI: 10.1002/jmri.20969.

(70) Stathaki, T. *Image Fusion: Algorithms and Applications*; Elsevier Science, 2011.

(71) Guenter, N.; Rainer, R. Noise, fluctuation, and HADAMARD-transform spectrometry. In *Proc.SPIE*, 2003; Vol. 5111, pp 273-282. DOI: 10.1117/12.510052.

(72) Hinckley, D. A.; Seybold, P. G. Thermodynamics of the rhodamine B lactone zwitterion equilibrium: An undergraduate laboratory experiment. *Journal of Chemical Education* **1987**, *64* (4). DOI: 10.1021/ed064p362.

Appendix

A. MATLAB Code

A.i. GaussFitv6

The following code is used to fit spectra of individual mirror columns to a gaussian peak. Then, the parameters of this gaussian are obtained to describe the centre wavelength, full-width at half-maximum, mirror spacing, and relative intensity of each mirror column.

```
%Adam Bernicky 2020
Had=[7 11 19 23 31 43 47 59 67 71 83 127];
% Had=[67];
Bloc=[1];
for i=2:size(Had,2)+1
    Bloc(i)=Bloc(i-1)+Had(i-1)+1;
    datbound(1,i-1)=Bloc(i-1)+1;%sets the lower bounds for data
    datbound(2,i-1)=Bloc(i-1)+Had(i-1);%sets the higher bounds for data
end
b=0;
L=1;
CN={'Background Spectra'...
    'Background Sub Spectra'...
    'Wavelength (nm)'...
    'Gaussian Coefficients'...
    'Average FWHM'...
    'Standard Deviation'...
    'Mirror Spacing (nm)'}';
Coeffs(2:8,1)=CN;
dat=Spec;
% for q=1:size(sname,2)
% file=['cALID aLL.csv'];
% dat=dlmread(file);
Wavel = dat(:,1);
dat=dat(:,2:end);
dir='C:\Users\Laser Lab\Documents\MATLAB\Blanks\211209';
%Inputs
for k=1:size(Had,2)

        savloc=[num2str(Had(k))];
        mkdir(dir,[num2str(Had(k))])
        label= ['Blank ' num2str(Had(k))];
        Coeffs{1,k+1}=label;
        CalibB = dat(:,Bloc(k));
        Coeffs{2,k+1}=CalibB;
        CalibB=repmat(CalibB,1,(Had(k)));
        Calib = dat(:,datbound(1,k):datbound(2,k));
        Calibsub= Calib-CalibB;
        Coeffs{3,k+1}=Calibsub;
        Coeffs{4,k+1}=Wavel;
        %%
        Coeff=zeros(Had(k),3);
        for i=1:(Had(k)-b);
```

```
[Pks,Loc]=findpeaks(Calibsub(10:2038,i),'MinPeakHeight',40,'MinPeakProminence',20,'So
rtStr','Descend'); %Finds the max peak for the gaussian fitting
            Rng=(Loc(1)-200:Loc(1)+200);
            Fit=fit(Wavel(Rng),Calibsub(Rng,i),'gauss1');%,'Exclude', X<init,
'Exclude', X>fin,'Lower', 0, 'Upper', 2);
            Coeff(i,1:3)=coeffvalues(Fit);
m=find(Wavel<=(Coeff(i,2))); %finding the closest spectrometer wavelength to the
gaussian center peak
                        m2=find(Wavel>=(Coeff(i,2)));
                        if Coeff(i,2)-Wavel(m(end))> Wavel(m2(1))-Coeff(i,2)
                            Coeff(i,2)=Wavel(m2(1));
                        else
                            Coeff(i,2)=Wavel(m(end));
                        end
        end
        Coeffs{5,k+1}=Coeff;
        FWHM=2*sqrt(2*log(2));
        for i=1:(Had(k)-b);   %Calculating the FWHM and HWHM of each gaussian using
'c' term
            Coeffs{6,k+1}=mean(Coeffs{5,k+1}(:,3).*FWHM);
            Coeffs{7,k+1}=std(Coeffs{5,k+1}(:,3).*FWHM);
            Coeffs{8,k+1}=mean(diff(Coeffs{5,k+1}(:,2)));
        end

        filename1 = [num2str(Had(k)) 'Coeffs.csv'];
         dlmwrite([dir '\' savloc '\' filename1],Coeffs{5,k+1},',');

        Max=max(Coeffs{5,k+1}(:,1));
        Cor=Coeffs{5,k+1}(:,1)./Max;
        filename2=[num2str(Had(k)) 'Cor.csv'];
        dlmwrite([dir '\' savloc '\' filename2],Cor,',');

        filename3=[num2str(Had(k)) 'Exwave.csv'];
        dlmwrite([dir '\' savloc '\' filename3],Coeffs{5,k+1}(:,2),',');
```

A.ii. demosaicv6

The following function is used to demosaic a 2048×2048-pixel raw image obtained from the msCam into 2D image with 8 256×256-pixel panels, each displaying a single colour channel of the camera. The size of the full image is therefore 512×1024 pixels.

```
function [W]=demosaicv6(K)
sizes=size(K);
if length(sizes)==2
    slices=1;
else
    slices=sizes(3);
end
for j=1:slices
        I=squeeze(K(:,:,j));
    I=I';
    for i=1:3
        if i==1
            Q1(1:256,1:256)=I(3:8:2048,1:8:2048); %474
            Q1(1:256,257:512)=I(1:8:2048,1:8:2048); %495
```

```
            Q1(1:256,513:768)=I(3:8:2048,5:8:2048); % 526
            Q1(1:256,769:1024)=I(1:8:2048,5:8:2048); % 546
            Q1(257:512,1:256)=I(5:8:2048,1:8:2048); %578
            Q1(257:512,257:512)=I(7:8:2048,1:8:2048);%597
            Q1(257:512,513:768)=I(5:8:2048,5:8:2048); %621
            Q1(257:512,769:1024)=I(7:8:2048,5:8:2048); %640
        elseif i==2
            Q2(1:256,1:256)=I(3:8:2048,1+(i-1):8:2048); %474
            Q2(1:256,257:512)=I(1:8:2048,1+(i-1):8:2048); %495
            Q2(1:256,513:768)=I(3:8:2048,5+(i-1):8:2048); % 526
            Q2(1:256,769:1024)=I(1:8:2048,5+(i-1):8:2048); % 546
            Q2(257:512,1:256)=I(5:8:2048,1+(i-1):8:2048); %578
            Q2(257:512,257:512)=I(7:8:2048,1+(i-1):8:2048);%597
            Q2(257:512,513:768)=I(5:8:2048,5+(i-1):8:2048); %621
            Q2(257:512,769:1024)=I(7:8:2048,5+(i-1):8:2048); %640
        else
            Q3(1:256,1:256)=I(3:8:2048,1+(i-1):8:2048); %474
            Q3(1:256,257:512)=I(1:8:2048,1+(i-1):8:2048); %495
            Q3(1:256,513:768)=I(3:8:2048,5+(i-1):8:2048); % 526
            Q3(1:256,769:1024)=I(1:8:2048,5+(i-1):8:2048); % 546
            Q3(257:512,1:256)=I(5:8:2048,1+(i-1):8:2048); %578
            Q3(257:512,257:512)=I(7:8:2048,1+(i-1):8:2048);%597
            Q3(257:512,513:768)=I(5:8:2048,5+(i-1):8:2048); %621
            Q3(257:512,769:1024)=I(7:8:2048,5+(i-1):8:2048); %640
        end
    end
        for r=1:512
            for c=1:1024
                W(r,c,j)=uint8(uint8(Q1(r,c))+uint8(Q2(r,c))+uint8(Q3(r,c))/3);
            end
        end
end
end
```

A.iii. demosaicubev3

The following function is used to demosaic a *n* number of 2048×2048-pixel raw images from the msCam that are acquired with Hadamard multiplexed light, and then subsequently demodulate each pixel to yield the resulting EEM (where *n* corresponds to the number of excitation masks). The resulting data is of the size 256×256×8×*n*.

```
function [D]=demosaicubev3(K)

K=im2double(K); %important to convert the data from uint8 type to double type
sizes=size(K);
if length(sizes)==2
    slices=1;
else
    slices=sizes(3);
    Ksig=K(:,:,2:end);
    Kback=K(:,:,1);
    K=Ksig-Kback; %Background subtraction
    slices=slices-1;
end
for j=1:slices
        I=squeeze(K(:,:,j));
```

```
    I=I';
    for i=1:3
        if i==1
            Q1(1:256,1:256,1)=I(3:8:2048,1:8:2048); %474
            Q1(1:256,1:256,2)=I(1:8:2048,1:8:2048); %495
            Q1(1:256,1:256,3)=I(3:8:2048,5:8:2048); % 526
            Q1(1:256,1:256,4)=I(1:8:2048,5:8:2048); % 546
            Q1(1:256,1:256,5)=I(5:8:2048,1:8:2048); %578
            Q1(1:256,1:256,6)=I(7:8:2048,1:8:2048);%597
            Q1(1:256,1:256,7)=I(5:8:2048,5:8:2048); %621
            Q1(1:256,1:256,8)=I(7:8:2048,5:8:2048); %640
        elseif i==2
            Q2(1:256,1:256,1)=I(3:8:2048,1+(i-1):8:2048); %474
            Q2(1:256,1:256,2)=I(1:8:2048,1+(i-1):8:2048); %495
            Q2(1:256,1:256,3)=I(3:8:2048,5+(i-1):8:2048); % 526
            Q2(1:256,1:256,4)=I(1:8:2048,5+(i-1):8:2048); % 546
            Q2(1:256,1:256,5)=I(5:8:2048,1+(i-1):8:2048); %578
            Q2(1:256,1:256,6)=I(7:8:2048,1+(i-1):8:2048);%597
            Q2(1:256,1:256,7)=I(5:8:2048,5+(i-1):8:2048); %621
            Q2(1:256,1:256,8)=I(7:8:2048,5+(i-1):8:2048); %640
        else
            Q3(1:256,1:256,1)=I(3:8:2048,1+(i-1):8:2048); %474
            Q3(1:256,1:256,2)=I(1:8:2048,1+(i-1):8:2048); %495
            Q3(1:256,1:256,3)=I(3:8:2048,5+(i-1):8:2048); % 526
            Q3(1:256,1:256,4)=I(1:8:2048,5+(i-1):8:2048); % 546
            Q3(1:256,1:256,5)=I(5:8:2048,1+(i-1):8:2048); %578
            Q3(1:256,1:256,6)=I(7:8:2048,1+(i-1):8:2048);%597
            Q3(1:256,1:256,7)=I(5:8:2048,5+(i-1):8:2048); %621
            Q3(1:256,1:256,8)=I(7:8:2048,5+(i-1):8:2048); %640
        end
    end
    for f=1:8
        for r=1:256
            for c=1:256
                W(r,c,f,j)=((Q1(r,c,f))+(Q2(r,c,f))+(Q3(r,c,f))/3);
            end
        end
    end

end
d=sizes(3); %build hadamard S-matrix
H=paleyI(d);
H=H(2:end,2:end);
H(H==1)=0;
H(H==-1)=1;
for r=1:256 %demosaic pixel by pixel
    for c=1:256
        D(r,c,:,:)=squeeze(W(r,c,:,:))*(H^-1)';
    end
end
D(D<0)=0; % all values less than 0 are set to zero
end
```